DIPLOMARBEIT

Ordered Equilibrium Structures in Confined Dipolar Systems

Ausgeführt am Institut für
Theoretische Physik
der Technischen Universität Wien
unter der Anleitung von

Ao. Univ. Prof. Dipl.-Ing. Dr. Gerhard Kahl

in Zusammenarbeit mit

Priv.-Doz. Prof. Agrégé Dr. Martial Mazars

durch

Moritz Antlanger
Tigergasse 8/16, 1080 Wien

21. Mai 2012

Abstract

We have studied systems of dipolar soft spheres in a confined slab geometry: the system is confined between two parallel walls (separated by a finite width) and is periodic in the other two directions. We were interested in the energetically most favorable configurations at zero temperature at constant number density. In order to find the particle configurations corresponding to the global minimum in the relevant thermodynamical potential, we have used an optimization tool based on ideas of genetic algorithms. For a correct treatment of the long-ranged dipolar interactions, energy calculations were carried out employing the method of Ewald sums. We have investigated confined systems of soft spheres both with and without dipole moment. In addition, we have also studied the effects of an external field perpendicular to the walls. We have identified the complex intermediate phases as the system creates, with increasing slab width, several interesting buckling structures.

Contents

1. Introduction

Dipolar fluids represent an interesting (model) system as they offer a complex interplay of a short-ranged soft sphere potential and long-ranged dipolar interactions. Such systems are of high importance in technology and biomedicine [1, 2] and much work has been dedicated to understanding their phase behavior (for an overview see [3, 4, 5, 6, 7, 8]). A few examples of realistic systems are discussed in section 1.1. While the bulk behavior of dipolar fluids has been studied rather extensively, less is known about their properties "between two and three dimensions", i.e. as multilayer systems. Such geometrical restrictions are of high relevance in technological applications, for instance as thin films. It is well known that the phase behavior of simple systems differs drastically when the system is of limited extent in one direction: the ordered phases of so-called quasi-2D systems have been studied in both theory [9, 10] and experiment [11, 12], showing interesting behavior such as buckling and twisting mesostructures. In order to foster a better understanding of the thermodynamically stable phases at finite temperatures, studying the system at zero temperature is a good starting point.

The aim of this Master's thesis is to find the energetically most favorable structures formed by a system of dipolar soft spheres in a confined geometry at zero temperature. The influence of an external field perpendicular to the walls will also be studied.

This thesis is organized in the following way:

- **Chapter 1** explains the model for our computations.
- **Chapter 2** deals with long-ranged interactions and how we treat them in our program.
- **Chapter 3** presents the ideas behind and our implementation of genetic

algorithms.

- **Chapter 4** elaborates on details of the optimization and how results were analyzed.
- **Chapter 5** presents the results we obtained for quasi-2D systems.
- **Chapter 6** summarizes our results and gives an outlook on possible future investigations.

1.1. Manufacturing Particles in Experiments

Many experimental systems in soft matter physics consist of paramagnetic particles that can be magnetized in an external field [13, 14]. Alternatively, it is also possible to manufacture colloids with almost dipole-like characteristics by printing a positive charge onto one hemisphere and a negative one onto the other [15], or to produce ferromagnetic colloids [16, 17]. In these experimental systems, the dipole moment of each particle is in most cases oriented parallel to the direction of the field.

1.2. Theoretical Model

The system we will investigate in this thesis consists of dipolar soft spheres, i.e. of spheres carrying a point dipole moment at their center. Such spheres interact with an isotropic (soft-sphere) potential and an anisotropic (dipolar) potential:

$$V_{\mathrm{ij}}\left(\mathbf{r}, \boldsymbol{\mu}_{\mathrm{i}}, \boldsymbol{\mu}_{\mathrm{j}}\right) = V_{\mathrm{ij}}^{\mathrm{iso}}\left(r\right) + V_{\mathrm{ij}}^{\mathrm{dip}}\left(\mathbf{r}; \boldsymbol{\mu}_{\mathrm{i}}, \boldsymbol{\mu}_{\mathrm{j}}\right) \tag{1.1}$$

For the isotropic potential, we have used

$$\begin{aligned} V_{\mathrm{ij}}^{\mathrm{iso}} &= V_{\mathrm{IPL}}\left(\alpha, r\right) \\ &= 4\epsilon\left(\frac{r}{\sigma}\right)^{-\alpha} \end{aligned} \tag{1.2}$$

where r is the distance between particles i and j, σ is the particle diameter, ϵ is the energy scaling, and α is a parameter of the potential. The superposition of

two such inverse power law potentials

$$V_{\mathrm{ij}}^{\mathrm{LJ}}(r) \;=\; V_{\mathrm{IPL}}(2\alpha, r) - V_{\mathrm{IPL}}(\alpha, r)\,, \tag{1.3}$$

more specifically with $\alpha = 6$, is called the Lennard-Jones potential (see Fig. 1.1). Although the Lennard-Jones potential is in general considered as a short-ranged interaction, the long-range contributions are definitely required when evaluating with sufficient accuracy the energy via Ewald sums for the Lennard-Jones system (see section 2.1).

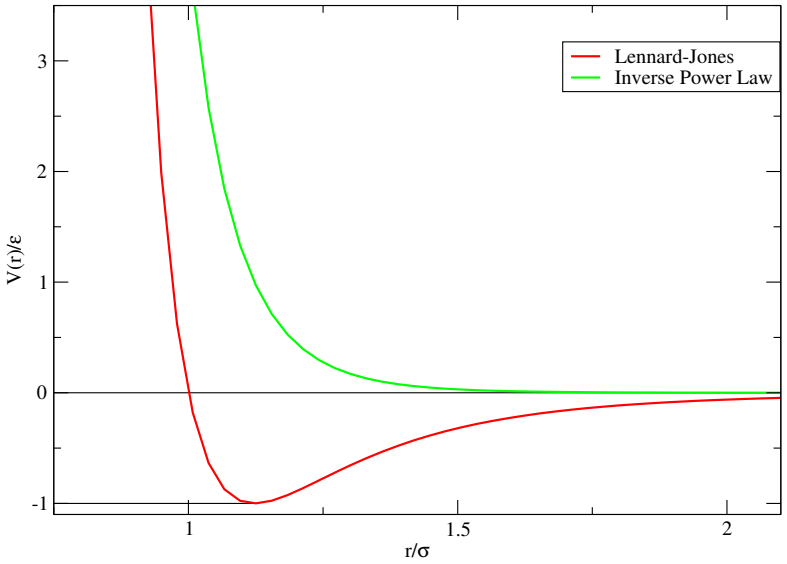

Figure 1.1.: Comparison between a Lennard-Jones and an inverse power law potential for $\alpha = 6$ and $\alpha = 12$, respectively. While the Lennard-Jones potential has an attractive minimum located at $r_{\mathrm{LJ}} = 2^{\frac{1}{6}}\sigma$ with a binding energy $-\epsilon$, the inverse power law potential is purely repulsive.

The anisotropic (dipolar) part of the potential can be written as

$$\begin{aligned} V_{\mathrm{ij}}^{\mathrm{aniso}} &= V_{\mathrm{dip}}(\mathbf{r}_{\mathrm{ij}}; \boldsymbol{\mu}_{\mathrm{i}}, \boldsymbol{\mu}_{\mathrm{j}}) \\ &= \frac{1}{r^3}\left[\boldsymbol{\mu}_{\mathrm{i}} \cdot \boldsymbol{\mu}_{\mathrm{j}} - 3\frac{(\boldsymbol{\mu}_{\mathrm{i}} \cdot \mathbf{r})\,(\boldsymbol{\mu}_{\mathrm{j}} \cdot \mathbf{r})}{r^2}\right] \end{aligned} \tag{1.4}$$

where $\boldsymbol{\mu}_{\mathrm{i}}$ and $\boldsymbol{\mu}_{\mathrm{j}}$ are the dipole moments of particles i and j, respectively.

For zero dipole moment, the total potential is purely repulsive. However, a finite dipole moment may, for certain α-values, lead to a net attraction [8, 18], i.e. even

at zero pressure the system does not disperse. We used $\alpha = 12$ for the inverse power law interaction in this work. An alternative would be a superposition of the Lennard-Jones potential and a dipolar potential; this is called the Stockmayer potential.

Apart from the interaction potentials of the particles, another determining characteristic of the system is the geometry. In this work, we are interested in the periodic structures formed by particles confined in a slab, i.e. where two of the three dimensions are infinite (and periodic), but the third is finite. This differs strongly from the monolayer case as we deal in the present case with an inherent 3D structure. Figure 1.2 shows a two-dimensional schematic representation of a confined system. In this work, we will define the slab width, i.e. the distance between the two hard walls that confine the system, as $H = h + \sigma$. Thus, the particle centers are confined to a slab of thickness h. Other important parameters of the system are the particle density ρ, the pressure P and the temperature T.

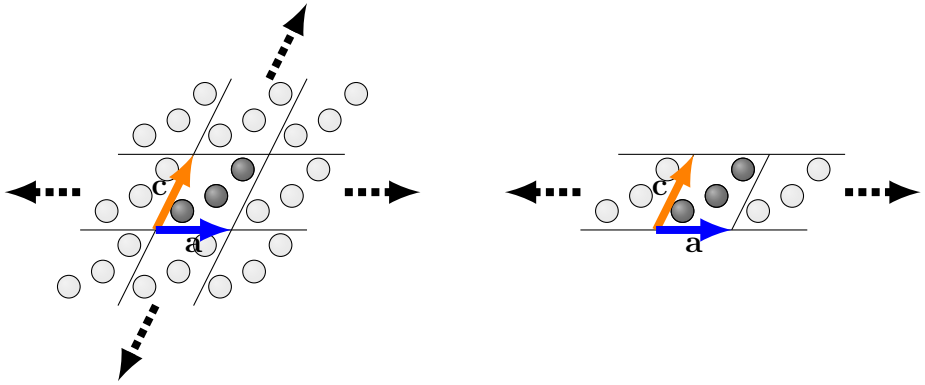

Figure 1.2.: Left: Two-dimensional schematic representation of 3D periodic boundary conditions. Right: Two-dimensional schematic representation of quasi-2D periodic boundary conditions, note the missing periodicity in **c**-direction. Actual calculations are carried out in 3D.

Dipoles tend to align head-to-tail in a periodic lattice direction whenever possible (see section 5). For slab geometries, this tendency can be reduced by applying an external electric field E_{ext} in the non-periodic direction z perpendicular to the walls of the slab. We can include the contribution of an external electric field to

the potential by adding the term

$$\begin{aligned} V_{\text{ext}}(\boldsymbol{\mu}) &= \boldsymbol{\mu} \cdot \mathbf{E}_{\text{ext}} \\ &= \mu_z E_{\text{ext,z}}. \end{aligned} \tag{1.5}$$

Apart from the orientation of the embedded dipole moment, the particles have no inner structure. We can, thus, treat them as point particles carrying point dipoles (see Fig. 1.3), i.e. only the centers of mass of the particles and their orientations are of relevance.

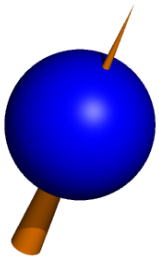

Figure 1.3.: Schematic representation of a dipolar soft sphere as used in this work. The particle (blue sphere) has a diameter σ, which is not drawn to scale, and a dipole moment $\boldsymbol{\mu}$ (orange cone). The actual particle diameter is given by the length of the orange cone; thus this visualization allows good visibility even for strong particle overlap.

In this work, we are searching for the energetically most favorable ordered equilibrium structures that our model system forms at zero temperature in the NVT ensemble. The thermodynamic quantity we thus need to minimize is the Helmholtz free energy $F = E - TS$. For $T = 0$, this expression simplifies to $F = E$. Alternatively, it is also possible to perform calculations in the NPT ensemble, where the relevant thermodynamic quantity is the Gibbs free energy $G = E + PV - TS$. For $T = 0$, G simplifies to $G = E + PV$.

Throughout, we will use reduced (dimensionless) units for the Gibbs free energy G, the energy E, the unit cell volume V, the dipole strength μ, and the external field strength E_{ext} in this work, i.e.

$$G^* = E^* + PV^* \tag{1.6}$$

with

$$E^* = \frac{E}{\epsilon} \tag{1.7}$$

$$V^* = \frac{V}{N\sigma^3} \tag{1.8}$$

$$\mu^* = \mu\sqrt{\frac{1}{\epsilon\sigma^3}} \tag{1.9}$$

$$E^*_{\text{ext}} = E_{\text{ext}}\sqrt{\frac{\sigma^3}{\epsilon}} \tag{1.10}$$

introducing the number of particles per unit cell N. Consequently, the density is defined by

$$\rho = \rho_{\text{H}} = \frac{N}{V} \tag{1.11}$$

The model we use for our computations is a unit cell containing N particles. The form and size of the unit cell is given by three lattice vectors **a**, **b**, and **c**. The position of a particle within the unit cell is given in fractional coordinates, i.e. in fractions of **a**, **b**, and **c**. Figure 1.4 shows a two-dimensional schematic representation of a unit cell, the lattice periodicity and fractional coordinates (actual calculations are carried out in three dimensions). The orientation of each particle is given by two orientational angles ψ and θ, measured with respect to the z-axis.

1.3. Lattice Parametrization

A given configuration can be described by the three lattice vectors **a**, **b**, and **c**, the $3N$ fractional particle coordinates x_{f}, y_{f}, and z_{f}, and the N particle (dipole) orientations $\boldsymbol{\mu}$. While it is possible to take into account all nine lattice vector components (which we will refer to as the "full form" in this work) only six components are necessary to describe any given lattice (we will refer to this as the "reduced form" of the lattice). Without loss of generality, we can assume that **a**

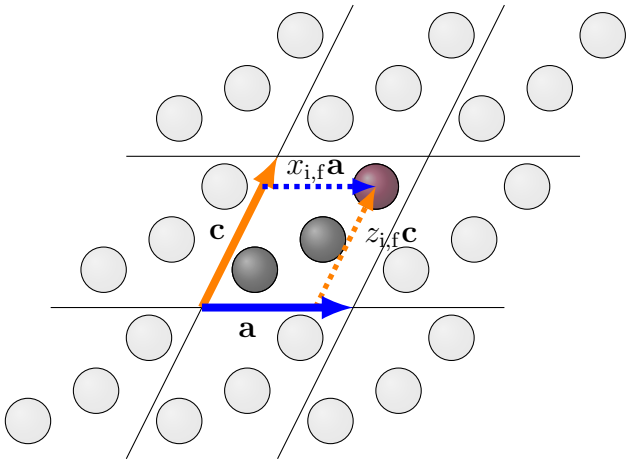

Figure 1.4.: Schematic representation of unit cell in a two-dimensional lattice, showing lattice vectors $\mathbf{a}$ and $\mathbf{c}$, fractional coordinates $x_{\mathrm{i,f}}$ and $z_{\mathrm{i,f}}$ (for the purple particle) and the lattice periodicity. The dark particles lie within the unit cell, the light particles are their periodic images.

points in x-direction and $\mathbf{b}$ lies in the x-y-plane [19]

$$\left.\begin{aligned} \tilde{\mathbf{a}} &= \begin{pmatrix} \tilde{a}_\mathrm{x} \\ \tilde{a}_\mathrm{y} \\ \tilde{a}_\mathrm{z} \end{pmatrix} \\ \tilde{\mathbf{b}} &= \begin{pmatrix} \tilde{b}_\mathrm{x} \\ \tilde{b}_\mathrm{y} \\ \tilde{b}_\mathrm{z} \end{pmatrix} \\ \tilde{\mathbf{c}} &= \begin{pmatrix} \tilde{c}_\mathrm{x} \\ \tilde{c}_\mathrm{y} \\ \tilde{c}_\mathrm{z} \end{pmatrix} \end{aligned}\right\} \rightarrow \left\{\begin{aligned} \mathbf{a} &= \begin{pmatrix} a_\mathrm{x} \\ 0 \\ 0 \end{pmatrix} \\ \mathbf{b} &= \begin{pmatrix} b_\mathrm{x} \\ b_\mathrm{y} \\ 0 \end{pmatrix} \\ \mathbf{c} &= \begin{pmatrix} c_\mathrm{x} \\ c_\mathrm{y} \\ c_\mathrm{z} \end{pmatrix} \end{aligned}\right. . \tag{1.12}$$

Moreover, we choose that $a_\mathrm{x} > 0$, $b_\mathrm{y} > 0$, and $c_\mathrm{z} > 0$, which reduces the volume calculation of the unit cell (UC) to $V_\mathrm{UC} = a_\mathrm{x} b_\mathrm{y} c_\mathrm{z} > 0$. In case that any of these three components becomes negative during the optimization process, we perform an inversion of the corresponding lattice vector, e.g. $\mathbf{a} \rightarrow -\mathbf{a}$, which leaves the lattice periodicity unchanged. In this case, particle coordinates need to be updated as well (otherwise we would mirror the lattice). The transformation from the full form to the reduced form can be described as a simple rotation (see appendix A.1).

In total, there are $5N+6$ independent parameters to optimize in constant pressure mode (three fractional coordinates plus two orientation angles per particle and six independent lattice vector components).

The reduced form of the lattice also enables us to easily implement a constant volume mode, i.e. to perform isochoric optimizations (in the NVT ensemble). This can be achieved by replacing the independent variable a_x with $a_\mathrm{x} \to V_\mathrm{UC}/(b_\mathrm{y}c_\mathrm{z})$, bringing along some changes in the expressions of the derivatives required in the optimization tool (see section 4.1). Thus in total, there are $5N + 5$ independent parameters to optimize in the constant volume mode.

2. Ewald Summations

2.1. Long-Ranged Interactions

In simulations, it is a common practice to truncate interactions for distances larger than a chosen cutoff radius. Beyond this distance, all contributions to the potential energy are neglected. For this work, we desire to obtain a relative accuracy in the energy calculations of $\delta = 10^{-6}$. For a simple $r^{-\alpha}$-potential, it is thus possible to estimate the required cutoff radius R_c: introducing E_c as the energy contributions from distances smaller than R_c, we use

$$\begin{aligned} E &\approx \int_0^\infty r^{-\alpha} r^2 \frac{4\pi}{3} \rho(r) dr \qquad (2.1)\\ &= \frac{4\pi}{3} \int_0^\infty r^{2-\alpha} \rho(r) dr \\ &= \frac{4\pi}{3} \frac{1}{3-\alpha} r^{3-\alpha}|_{R_0}^{\infty} \\ &= -\frac{4\pi}{3} \frac{1}{3-\alpha} R_0^{3-\alpha} \\ E_\mathrm{c} &\approx \frac{4\pi}{3} \frac{1}{3-\alpha} r^{3-\alpha}|_{R_0}^{R_\mathrm{c}} \qquad (2.2)\\ &= \frac{4\pi}{3} \frac{1}{3-\alpha} \left(R_\mathrm{c}^{3-\alpha} - R_0^{3-\alpha} \right) \\ \frac{\triangle E}{E} = \frac{E - E_\mathrm{c}}{E} &\approx \left(\frac{R_\mathrm{c}}{R_0} \right)^{3-\alpha} \approx \left(\frac{R_\mathrm{c}}{\sigma} \right)^{3-\alpha} \qquad (2.3) \end{aligned}$$

assuming that the radial distribution of the particles is approximately constant as long as they do not overlap

$$\begin{aligned} \rho(r) &= \begin{cases} 0 & r < R_0 \\ \text{const.} & r > R_0 \end{cases} \qquad (2.4)\\ R_0 &\approx \sigma. \qquad (2.5) \end{aligned}$$

R_c can therefore be estimated to

$$\frac{\triangle E}{E} \leq \delta = 10^{-6} \approx \left(\frac{R_c}{\sigma}\right)^{3-\alpha} \tag{2.6}$$

$$R_c \geq 10^{\frac{6}{\alpha-3}}\sigma. \tag{2.7}$$

The assumption that the radial distribution of the particles is (approximately) constant is not necessarily a good one, especially for a perfectly ordered crystal. The expression derived above is also only valid for $\alpha > 3$. The interaction of dipoles decays as r^{-3}, i.e. the estimated required cutoff radius diverges for the dipolar interaction (and even more so for the Coulomb interaction). Such interactions are therefore considered long-ranged and treating them with simple truncation can introduce serious numerical error. Errors can even occur for the Lennard-Jones interaction (with an exponent $\alpha = 6$). Using the above expression for an accuracy of $\delta = 10^{-6}$, we obtain $R_c \geq 100\sigma$, a prohibitively large value. It is therefore necessary to use more adequate methods to deal with such interactions. In contrast, the inverse power law interaction (with $\alpha > 10$) does not have to be treated as long-ranged, as it only requires $R_c \geq 7.197\sigma$, so using a cutoff radius of $R_c = 10\sigma$ is perfectly fine.

One way of treating properly long-ranged interactions are so-called Ewald summations. We will use this method in this work; it will be explained in section 2.2. Alternative approaches to this method include reaction field methods [20], the Nijboer-de Wette method [21, 22], the Lekner sums [23, 24], calculations on hyperspheres [25], and the fast multipole method [26, 27, 28].

2.2. Ewald Summations

The method of Ewald summation can be applied to any periodic system [29, 30, 31, 32]. Its basic idea is to modify the function $f(\boldsymbol{r})$ which is the target function of the summation in real space. $f(\boldsymbol{r})$ is modified by another function $g(\boldsymbol{r})$ such that either function decays rapidly in real and reciprocal space:

$$\begin{aligned} f(\mathbf{r}) &= [f(\mathbf{r}) - g(\mathbf{r})] + g(\mathbf{r}) \\ &= h(\mathbf{r}) + g(\mathbf{r}). \end{aligned} \tag{2.8}$$

Typically, $g(\mathbf{r})$ is chosen such that the function $h(\mathbf{r})$ decays rapidly in real space. For a crystal of point charges, an example for $g(\mathbf{r})$ would be Gaussian charge distributions of the opposite sign (see Fig. 2.1). While summation over $h(\boldsymbol{r})$ is performed in real space, the summation over $g(\boldsymbol{r})$ is realized in reciprocal space:

$$\begin{aligned} \sum_{\mathbf{r}} f(\mathbf{r}) &= \sum_{\mathbf{r}} \left[f(\mathbf{r}) - g(\mathbf{r}) \right] + \sum_{\mathbf{r}} g(\mathbf{r}) \\ &= \sum_{\mathbf{r}} h(\mathbf{r}) + \sum_{\mathbf{k}} \tilde{g}(\mathbf{k}) . \end{aligned} \tag{2.9}$$

This concept can be applied to any kind of interaction, the difficulty lies in finding an appropriate $g(\mathbf{r})$ that ensures rapid decay and for which the Fourier transform is known.

2.3. Interaction Energies Expressed as Ewald Sums

Using the Ewald summation scheme, the total interaction energy for potentials of type $r^{-\alpha}$ can be written as [33, 34]

$$\begin{aligned} E_{\mathrm{SS}}^{\alpha} &= \frac{1}{2} \sum_{\mathrm{i}}^{\mathrm{N}} \sum_{\mathrm{j}}^{\mathrm{N}} {\sum_{\mathbf{R}}}' V_{\mathrm{SS}}^{\alpha}(r) \\ &= \frac{2\epsilon\sigma^{\alpha}}{\Gamma(\frac{\alpha}{2})} \left\{ \frac{2\pi^{\frac{3}{2}}\nu^{\alpha-3}}{(\alpha-3)V} N^2 - \frac{2\nu^{\alpha}}{\alpha} N + {\sum_{\mathrm{i}}^{\mathrm{N}}}' {\sum_{\mathbf{R}}}' \sum_{\mathrm{j}}^{\mathrm{N}} \frac{\Gamma\left(\frac{\alpha}{2}, \nu^2 r^2\right)}{r^{\alpha}} + \right. \\ &\quad \left. + \frac{\pi^{\frac{3}{2}}}{V} \sum_{\mathrm{i}}^{\mathrm{N}} \sum_{\mathbf{k}\neq 0} \sum_{\mathrm{j}}^{\mathrm{N}} \cos(\mathbf{k}\cdot\mathbf{r}_{\mathrm{ij}}) \left(\frac{k}{2}\right)^{\alpha-3} \Gamma\left(\frac{3-\alpha}{2}, \frac{k^2}{4\nu^2}\right) \right\} \end{aligned} \tag{2.10}$$

where $r = |\mathbf{r}_{\mathrm{ij}} + \mathbf{R}|$ is the distance between two particles, $\mathbf{R} = n_{\mathrm{a}}\mathbf{a} + n_{\mathrm{b}}\mathbf{b} + n_{\mathrm{c}}\mathbf{c}$ represents the lattice periodicity, and $\mathbf{k} = \tilde{n}_{\mathrm{a}}\tilde{\mathbf{a}} + \tilde{n}_{\mathrm{b}}\tilde{\mathbf{b}} + \tilde{n}_{\mathrm{c}}\tilde{\mathbf{c}}$ is a reciprocal lattice vector. The above expression consists of a summation in real space, a summation in reciprocal space and constant terms. The primed sum excludes the term for $i = j$ when $\mathbf{R} = 0$. The incomplete Gamma functions, $\Gamma\left(\frac{\alpha}{2}, \nu^2 r^2\right)$ and $\Gamma\left(\frac{3-\alpha}{2}, \frac{k^2}{4\nu^2}\right)$, are computationally very expensive and are therefore prime candidates for tabulation (see section 4.3). The parameter ν determines the behavior of the "screening function", its effects will be described in section 2.5. Since the Lennard-Jones

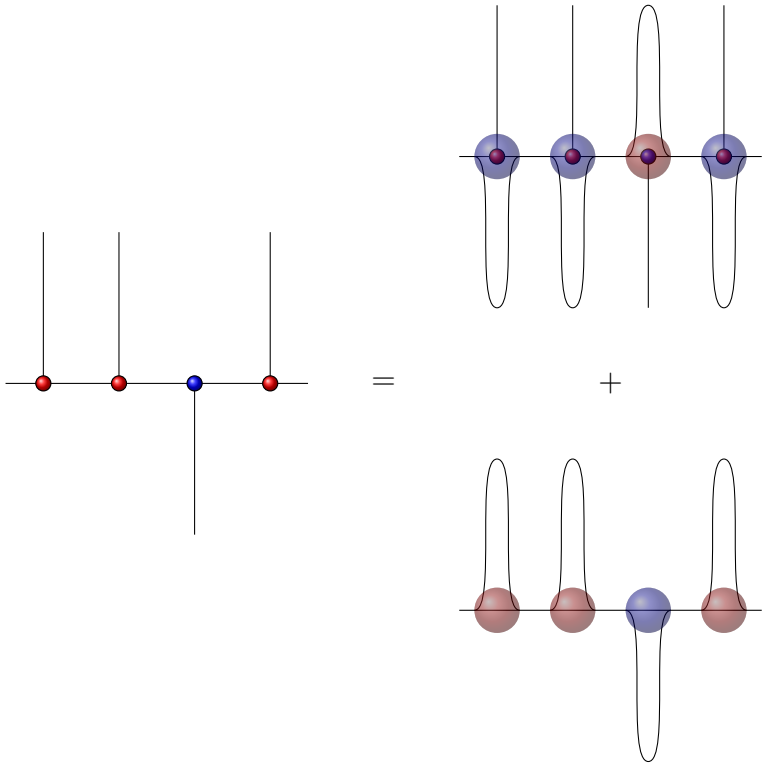

Figure 2.1.: Schematic representation of the basic idea of Ewald summations. The energy of a periodic configuration of particles with a long-ranged interaction is represented as a rapidly decaying term and a term that can be calculated in reciprocal space. For a Coulombic system, the energy of a periodic configuration of point charges (left) is difficult to calculate as the interaction is long-ranged. The interaction can be reformulated as the sum over screened charges (right top) and over screening charge distributions (right bottom).

potential is simply a superposition of two inverse power law potentials (of different sign and exponents), it can be treated with the Ewald summation scheme.

The dipolar interaction energy (see equ. 1.4) can be written as [34, 35, 36]

$$\begin{aligned} E_{\mathrm{dip}} &= \frac{1}{2}\sum_{\mathrm{i}}^{\mathrm{N}}\sum_{\mathrm{j}}^{\mathrm{N}}{\sum_{\mathbf{R}}}' \left[(\boldsymbol{\mu}_{\mathrm{i}}\cdot\boldsymbol{\mu}_{\mathbf{j}})\,B(r,\nu) - (\boldsymbol{\mu}_{\mathrm{i}}\cdot\mathbf{r})\,(\boldsymbol{\mu}_{\mathrm{j}}\cdot\mathbf{r})\,C(r,\nu)\right] - \\ &\quad -\frac{2\nu^3}{3\sqrt{\pi}}\sum_{\mathrm{i}}^{\mathrm{N}}\mu_{\mathrm{i}}^2 + \frac{2\pi}{V}\sum_{\mathbf{k}\neq 0}\frac{1}{k^2}\exp\left(-\frac{k^2}{4\nu^2}\right)\tilde{M}(\mathbf{k})\tilde{M}^*(\mathbf{k}) \end{aligned} \tag{2.11}$$

where $\boldsymbol{\mu}_{\mathrm{i}}$ is the dipole moment of particle i and

$$B(r,\nu) = \frac{1}{r^3}\left[\frac{2\nu r}{\sqrt{\pi}}\exp(-\nu^2 r^2) + \mathrm{erfc}(\nu \mathrm{r})\right] \tag{2.12}$$

$$\begin{aligned} C(r,\nu) &= -\frac{1}{r}\frac{d}{dr}B(r,\nu) \\ &= \frac{1}{r^5}\left[\frac{2\nu r}{\sqrt{\pi}}(3+2\nu^2 r^2)\exp(-\nu^2 r^2) + 3\mathrm{erfc}(\nu \mathrm{r})\right] \end{aligned} \tag{2.13}$$

$$\tilde{M}(\mathbf{k}) = \sum_{\mathrm{i}}^{\mathrm{N}}(\boldsymbol{\mu}_{\mathrm{i}}\cdot\mathbf{k})\exp(-\imath\mathbf{k}\cdot\mathbf{r}_{\mathrm{i}}). \tag{2.14}$$

The factor ν is a parameter of the Ewald sum. When performing the sum over all $\mathbf{R}$ and $\mathbf{k} \neq 0$, the energy is independent of the choice of ν. The forces acting on the particles can be obtained by calculating the derivatives of above expressions with respect to $\mathbf{r}$.

2.4. Effects of Macroscopic Boundary Conditions

The Ewald summation is only of conditional convergence for the dipolar interaction [34, 36], i.e. depending on in what order the sum is carried out, the results may vary. This is related to the choice of macroscopic boundary conditions (i.e. how the system behaves at $r \to \infty$). The macroscopic boundary conditions are considered at the surface of a (large) experimental system. Depending on the dielectric permittivity ϵ_{r} of the medium surrounding the system at $r \to \infty$, the

energy of the system is corrected by a term

$$E_{\epsilon_\mathrm{r}} = \frac{2\pi}{V}\frac{1}{2\epsilon_\mathrm{r}-1}\sum_{\mathrm{i}}^{\mathrm{N}}\sum_{\mathrm{j}}^{\mathrm{N}}\boldsymbol{\mu}_\mathrm{i}\boldsymbol{\mu}_\mathrm{j} \tag{2.15}$$

$$= \frac{2\pi}{V}\frac{1}{2\epsilon_\mathrm{r}-1}\left|\mathbf{P}\right|^2$$

$$\mathbf{P} = \sum_{\mathrm{i}}^{\mathrm{N}}\boldsymbol{\mu}_\mathrm{i}, \tag{2.16}$$

i.e. an energy contribution that slightly disfavors parallel orientation of all dipoles. In this work, we will use metallic boundary conditions ($\epsilon_\mathrm{r} = \infty$), which means that this contribution vanishes.

2.5. Ewald Summation Parameters

The calculation of the interaction energy via Ewald summation is exact if infinite sums are taken into account. In this case, the energy calculation does not depend on the parameter ν introduced in equ. 2.10. However, this is not necessarily true for finite cutoff radii in real and reciprocal space. Still, for appropriate values for the cutoff radii R_cut in real space and K_cut in reciprocal space, the energy calculation can, at least in an interval, be independent of ν. If this is indeed true can be verified for several random, ordered reference configurations. An example of the ν-dependence of the energy for a selection of different configurations is shown in Fig. 2.2. From this figure it becomes obvious that we have to choose a ν-value that lies inside the plateau region. These plateaus become larger with increasing cutoff radii, requiring, however, more computational resources. While for very slowly decaying potentials, such as the dipolar interaction, very large or infinite cutoff distances are necessary to obtain good accuracy when performing calculations in real space only, the cutoff radii for Ewald summation in real and reciprocal space are significantly smaller. An estimate for the order of magnitude of the optimum values for ν, the real space cutoff radius R_cut and the reciprocal space cutoff K_cut is given by [34]

$$\nu_\mathrm{opt} \approx \frac{N^{\frac{1}{6}}}{V^{\frac{1}{3}}}\left(\frac{t_\mathrm{R}}{t_\mathrm{F}}\right)^{\frac{1}{6}} \tag{2.17}$$

$$R_{\mathrm{cut}_{\mathrm{opt}}} \approx \sqrt{-\ln\delta}\frac{1}{\nu_{\mathrm{opt}}} = 3.717\frac{1}{\nu_{\mathrm{opt}}} \tag{2.18}$$

$$K_{\mathrm{cut}_{\mathrm{opt}}} \approx \sqrt{-\ln\delta}\nu_{\mathrm{opt}} = 3.717\nu_{\mathrm{opt}} \tag{2.19}$$

where t_{R} and t_{K} are the CPU-times necessary to compute an individual particle-particle interaction in real or reciprocal space, respectively, and δ, e.g. $\delta = 10^{-6}$, is the desired accuracy. The computational cost should be minimal for the set of parameters $(\nu_{\mathrm{opt}}, R_{\mathrm{cut}_{\mathrm{opt}}}, K_{\mathrm{cut}_{\mathrm{opt}}})$. For our computations we chose for the dipolar interaction $\nu = 1.5$, $R_{\mathrm{cut}} = 7\sigma$, $K_{\mathrm{cut}} = 12/\sigma$ for the dipolar interaction. The soft sphere interactions were calculated in real space only with a cutoff radius $R_{\mathrm{c}} = 10\sigma$. Alternatively, good parameters when using Ewald summation are $\nu = 1$, $R_{\mathrm{cut}} = 7\sigma$, $K_{\mathrm{cut}} = 12/\sigma$. These values yield an accuracy on the order of 10^{-6} for a broad variety of configurations.

2.6. Treatment of Quasi-2D Systems

While an analytical expression for the Ewald summation in slab geometries is available [34], this expression is computationally unfavorable as it contains quite a few two-particle summations instead of the one-particle summations available in 3D. One way to circumvent this problem is to use the properties of image charges of a system confined between two parallel metallic walls. The charges of particles in a slab geometry are replicated infinitely as image charges. For dipoles, not only are their positions mirrored respective to the wall, but also their orientations (see Fig. 2.3). In such a system, the combined unit cell of the slab and its first image charges on one side are replicated periodically orthogonal to the walls. For such an "expanded" unit cell, 3D periodicity is retained. While this is an exact way of treating the quasi-2D geometry, the related doubling of the number of particles per unit cell does slow down computations as more interactions need to be calculated. Another possible way to deal with the missing periodicity in the third direction is to modify the unit cell such that even when the slab is replicated in 3D, the contribution from these inexistent layers is insignificant. This presumes that the slab is surrounded by vacuum (not metal) at the walls. In this work, we will use the latter method (see section 2.7).

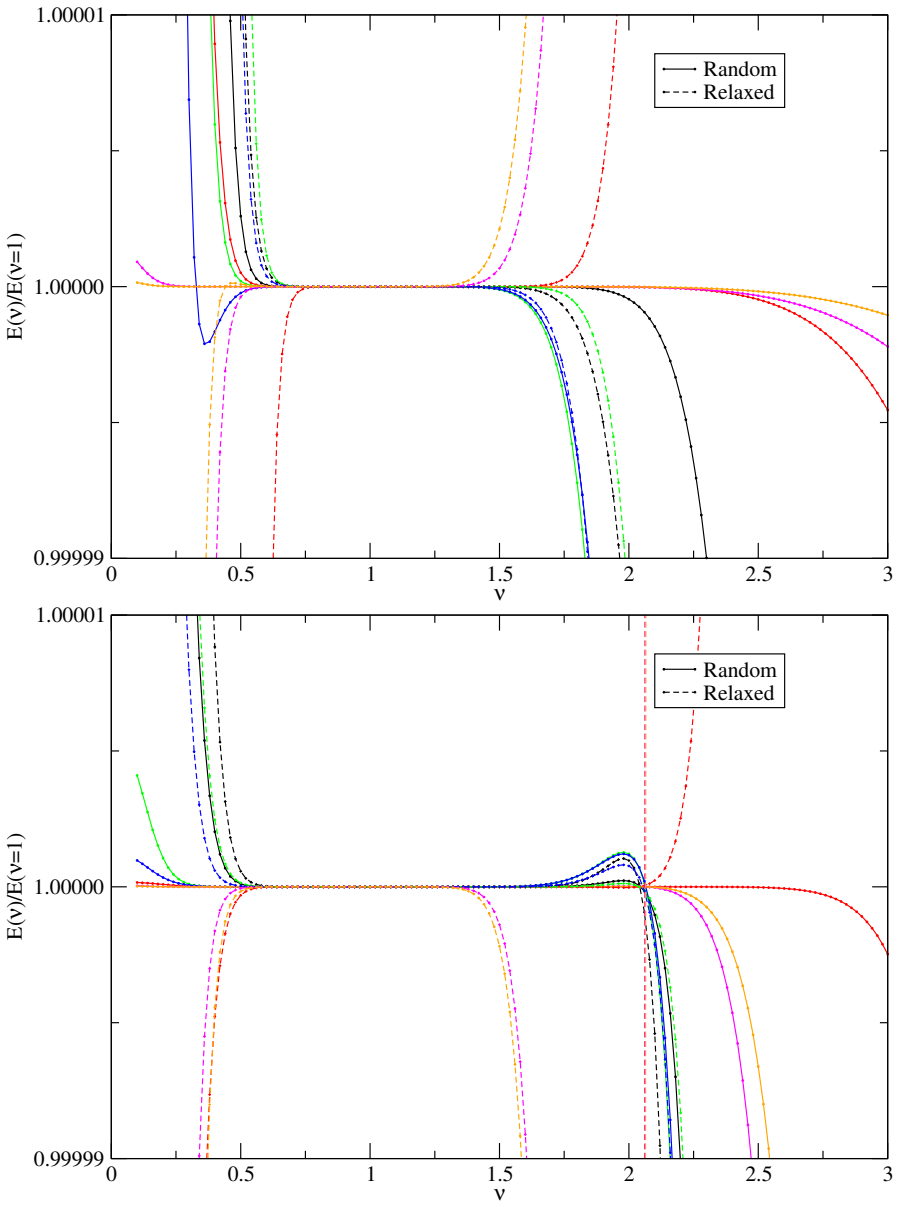

Figure 2.2.: ν-dependence of the energy calculation via Ewald sum $E = E(\nu)$ for several reference configurations and for $R_{\text{cut}} = 5\sigma$ and $K_{\text{cut}} = 10/\sigma$. On the abscissa, $E(\nu)/E(\nu = 1)$ is plotted for several different random starting configurations (solid lines) and their locally optimized (see section 4.1) final forms (dashed lines). Top: Dipolar interaction. Bottom: Inverse Power Law Interaction.

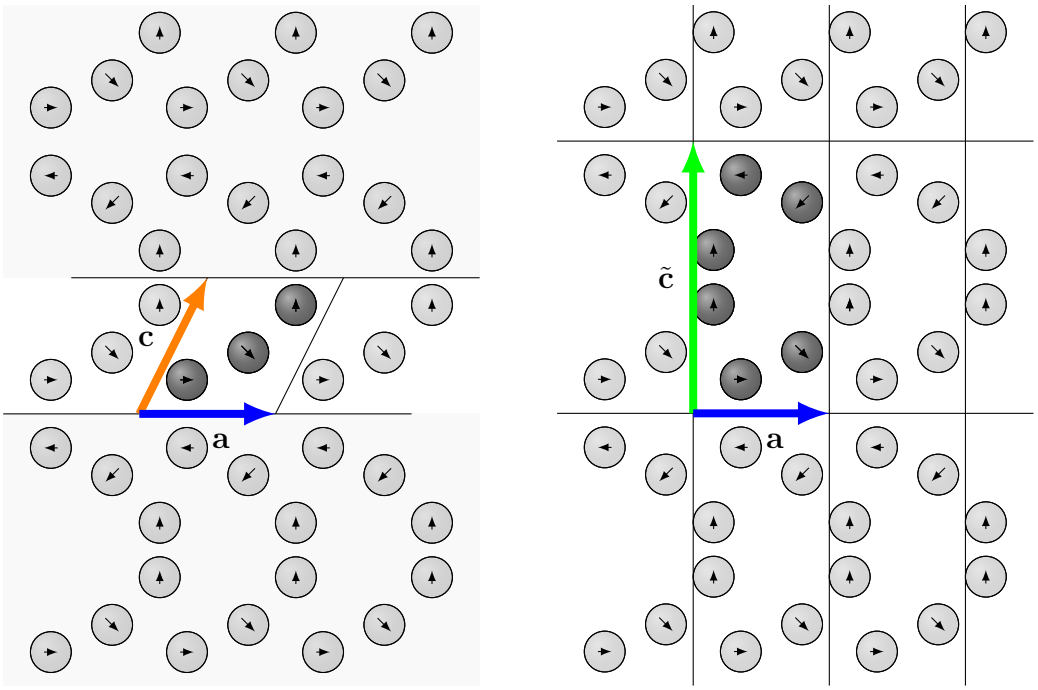

Figure 2.3.: Left: Two-dimensional schematic representation of a unit cell in quasi-2D geometry and its image charges. Areas shaded in grey signify the metallic walls. The system of charges (or dipoles) is constructed by placing the image charges of the particle in the slab and then iteratively adding the images of those images (produced by the opposite wall) *ad infinitum*. Right: Treatment of the structure shown in the left panel using an expanded unit cell (twice the size of the original unit cell) with 3D periodicity. Actual calculations are carried out in 3D.

2.7. Quasi-2D Approximation

In this thesis we chose to employ an approximation to the quasi-2D geometry via a 3D geometry [37, 38, 39, 40, 41, 42]. Within this approach, a region of empty space of width $h_{\mathrm{vac}} = (W-1)h$ is added in the non-periodic direction, i.e. the cell is stretched by the stretching factor W in the non-periodic direction and the particles are confined to a part of the unit cell. The total unit cell is then replicated in 3D (see Fig. 2.4). For the dipolar energy, the calculations are the same as those in 3D, apart from a correction term

$$E_{\mathrm{corr}} = \frac{2\pi}{V}\left(\sum_{i}^{N}\mu_{\mathrm{z,i}}\right)^2 . \tag{2.20}$$

This correction term favors, as does the chain formation caused by energetically favored head-to-tail configurations, in-plane dipole arrangements. Applying an external field therefore leads to very interesting effects (see section 1.2). For the soft sphere energy, the sum in real space is carried out only with 2D-periodicity. The particle centers are confined to fractional coordinates $0 \leq z_{\mathrm{f}} \leq 1/W$ (instead of $0 \leq z_{\mathrm{f}} \leq 1$ in the 3D system), which corresponds to $0 \leq z \leq h$ (the actual impenetrable walls are located at $-\sigma/2$ and $\sigma/2$, see Fig. 2.5 for clarification). The c_{z}-component of the lattice vectors is kept constant at $c_{\mathrm{z}} = Wh$.

2.8. Quasi-2D Parameters

For the 3D approximation to the quasi-2D geometry, we chose a variable stretching factor W such that the vacuum layer between neighboring slabs is of thickness h_{vac}. This ensures that even for small values of slab thickness h contributions from neighboring layers remain insignificant (which is not given for $W = const.$). Densities for quasi-2D systems are given in ρ_{H}, which corresponds to the total *available* volume in the slab (i.e. between the impenetrable walls). Figure 2.6 shows the h_{vac}-dependence of the energy of a quasi-2D system. For a few reference configurations, we can see that a vacuum layer thicker than $h_{\mathrm{vac}} \geq 10\sigma$ is fine in most cases. To be on the safe side (especially for small slab width), we chose $h_{\mathrm{vac}} =$

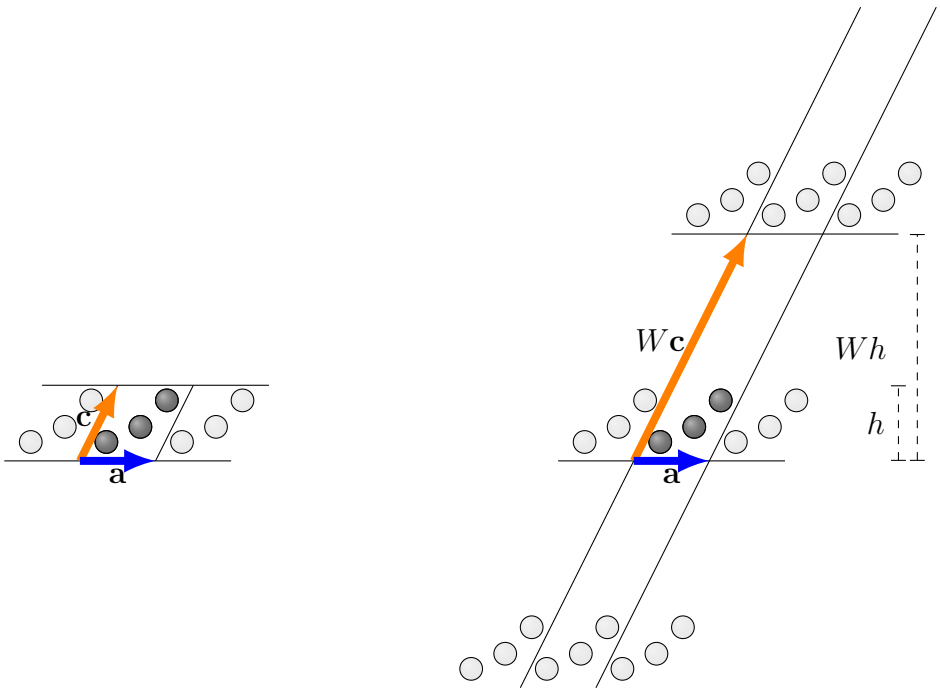

Figure 2.4.: Left: Two-dimensional schematic representation of a unit cell in quasi-2D geometry. Note the missing periodicity in **c**-direction. Right: Approximation of the structure shown in the left panel introducing empty regions via a stretching factor W. Actual calculations are carried out in 3D.

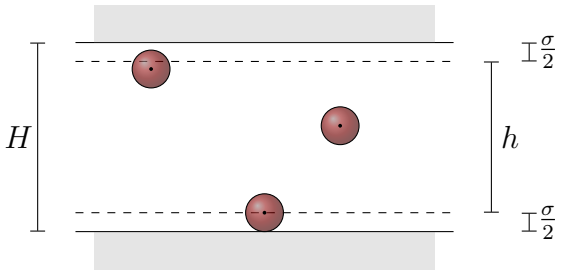

Figure 2.5.: Set-up of the impenetrable walls. Particle centers are confined to the region $0 \leq z \leq h$ (limited by dashed lines), the actual walls are separated by a distance $H = h + \sigma$ (solid lines).

15σ (interaction of a head-to-tail dipole arrangement between layers contributes at most $|\triangle E| \leq 2/(h_{\mathrm{vac}}^3)\mu^2 = 5.9 \times 10^{-4}\mu^2$).

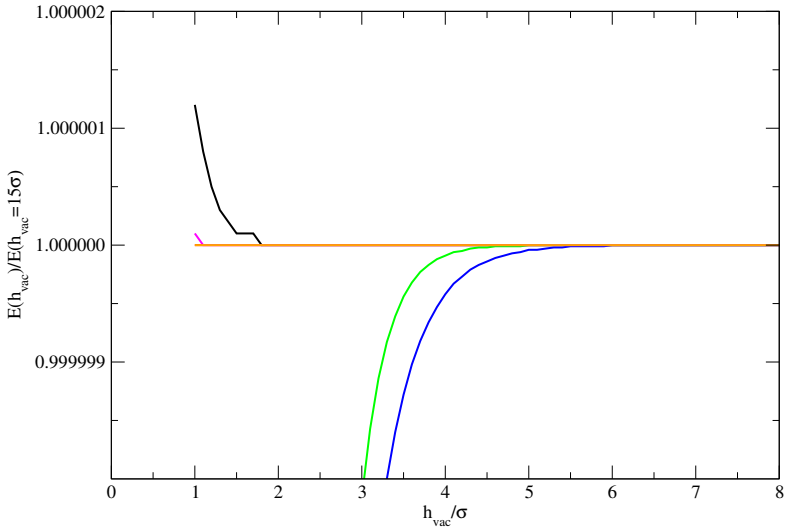

Figure 2.6.: h_{vac}-dependence of the energy calculation for slab geometry for several different configurations (different colors). For large enough separations, the slab geometry is well described by a layered system with full 3D periodicity.

3. Genetic Algorithms

3.1. Complex Energy Landscapes

The problem we face is that the optimization problem for a complicated system has, in the general case, no analytical solution. Apart from the large number of parameters that need to be optimized, the energy function itself is also highly complicated and can show many local minima in the parameter space. A simple local optimization (via gradient descent or Newton methods) is thus not possible without prior knowledge of the problem itself. In many previous works [3, 4, 5, 6, 8], starting points were simply guessed as possible candidate structures, sometimes making use of symmetry or periodicity arguments derived from the interaction potential and the boundary conditions. However, irrespective of how many different candidate structures are taken into consideration for local optimization, any other (unforeseen) structures cannot come into play. Therefore, it can be imperative to make use of more complicated optimization methods to deal with complex energy landscapes. In our case, we chose an optimization tool based on ideas of genetic algorithms.

3.2. Idea Behind Genetic Algorithms

As first described by Darwin [43], the theory of evolution states that individuals adapt to a given environment by a series of genetic optimizations. Fitter (i.e. better adapted or optimized) individuals have a higher chance of passing on their genetic material. Even though some randomness is involved, over time better adapted individuals will emerge. From time to time, individuals can also mutate (i.e. their

genetic material undergoes a sudden, random change). This can also lead to better adaptation to the environmental circumstances. In natural systems, this process of evolution generally takes place on long time-scales (thousands or millions of years), but nevertheless allowed a transition from the most basic amino acids to beings as complex as humans. The "evaluation" of an individual's adaptation is very complex, since it involves interactions between different individuals and many other factors.

This general concept can also be used as an optimization strategy [44, 45, 46, 47, 48] that can be adapted to a broad variety of systems. Genetic algorithms as computer simulations were introduced in a general form in 1975 by J. H. Holland [49]. In contrast to natural systems, the evaluation of an individual's adaptation is done with an analytical function in computer simulations. During the past decades, many different problems in different fields of science and technology (among them acoustics [50], aerospace engineering [51], chemistry [52], electric engineering [53], and materials engineering [54], to name just a few) were investigated using genetic algorithms. The advantage is that in many cases, a genetic algorithm, if correctly implemented, does not apply any constraints as to what solutions it will consider.

3.3. Genotype and Phenotype Genetic Algorithms

A given individual can be described in two ways: by its genotype and by its phenotype. The genotype corresponds to the genetic information encoded as a sequence of bits assigned values of 0 or 1. The first types of genetic algorithms were genotype algorithms. In this case, it is very easy to define the two important genetic operators, namely crossover (basically mating) and mutation (see Fig. 3.1), as they are directly equivalent to their natural counterparts. During crossover, the genetic code of the two parents is combined by taking a part from one parent and the rest from the other. Mutation simply consists of flipping bits with a certain probability. The fitness of an individual is determined by decoding its physical properties from its genetic code and then evaluating a certain fitness function. Genotype algorithms generally require many time-consuming en- and decoding operations (i.e. conversions from genotype to phenotype and back).

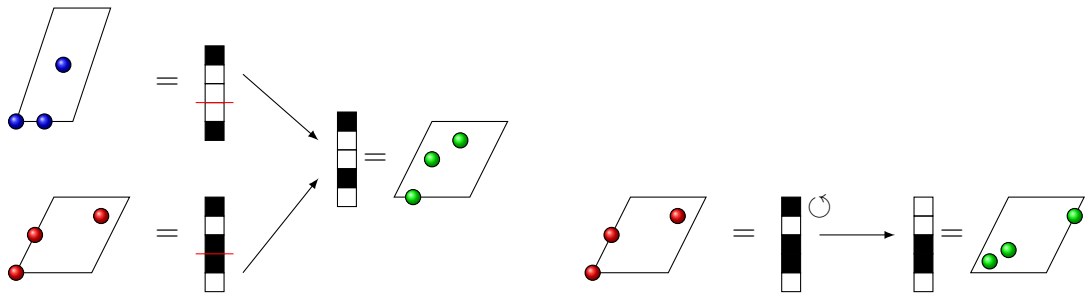

Figure 3.1.: Schematic representation of the crossover and mutation operations for a genotype genetic algorithm. Left: Crossover combines strands of both parents to form a child. Right: Mutation simply flips single bits of genetic information.

Phenotype algorithms, on the other hand, simply encode the individual via its physical properties. It is thus no longer necessary to en- or decode the individual, but all of the genetic operations (crossover and mutation) need to be redefined. While this can be tricky, it can, with some knowledge of the problem at hand, be possible to define the genetic operators in such a way that it becomes easier to escape from local minima in the energy landscape.

3.4. General Layout

In our group, genetic algorithms have been successfully applied to the identification of ordered equilibrium structures in condensed matter [55], 3D soft matter systems [56, 57], 2D soft matter systems [58, 59, 60, 61, 62] and quasi-2D soft matter systems [63, 64]. The program presented in this work is based on genetic algorithm tools originally developed by Dieter Gottwald [65] and modified by Julia Fornleitner [66] and Gernot Pauschenwein [67]. In particular, the phenotype implementation and overall structure of the program are based on the program developed by Günther Doppelbauer [68, 69] and adapted for dipolar systems by Camille Jouvie [70].

3.4.1. Generations and Pool

In a traditional genetic algorithm, the creation of new individuals is performed in generations. Individuals of a parent generation are combined and mutated to form a child generation. Except for a few individuals (see section 3.4.4) all individuals are replaced in the child generation. This process is, unfortunately, not well-suited for parallelization as the creation of new individuals requires an amount of time that strongly depends on the parents used, on mutation and on other factors. We therefore employed a restructuring of the concept of a generation developed by Günther Doppelbauer [69] where the generations are replaced by a pool of individuals (see section 4.5).

3.4.2. Initialization

In the beginning, when we know very little about suitable configurations for a given set of parameters, we start from random configurations. These are created by asigning the lattice vectors values such that the enclosed angles range between 30° and 60° and the volume they define is equal to a given input parameter V_{init}. For a constant volume optimization, we have to choose $V_{\text{init}} = V_{\text{UC}}$. The fractional coordinates of each particle are chosen as random numbers $(0, 1]$ and the dipole orientation angles are chosen such that they are random according to sphere point picking [71], i.e. $0 \leq \theta \leq 360°$ and $-1 \leq \cos\psi \leq 1$.

3.4.3. Fitness Function

The fitness of an individual is a measure of how well it is adapted to its environment. Fitter individuals are better adapted and are therefore more likely to procreate. For our purposes, a "fit" individual is characterized by a low Gibbs free energy G or Helmholtz free energy F (i.e. such an individual is well adapted to the external parameters), since we are looking for the energetically most favorable configuration. The probability for an individual to be selected as a parent (see section 3.5.1) is determined by its modified fitness. The modified fitness depends on the fitness, which in turn is calculated from the thermodynamic potential G or

F of the individual. The expression for the fitness function we use is given by (in the NPT-ensemble)

$$f_{\mathrm{i}} \;=\; \exp\left(-P_{\mathrm{fit}}\frac{G_{\mathrm{i}}-\mathrm{MIN_j(G)}}{\mathrm{MAX_j(G)}-\mathrm{MIN_j(G)}}\right) \tag{3.1}$$

where P_{fit} is a parameter that determines how much more likely a better individual is to procreate (the higher P_{fit}, the more favored better individuals are) and $\mathrm{MIN_j(G)}$ and $\mathrm{MAX_j(G)}$ are the minimum and maximum in G in the pool, respectively. The modified fitness is then calculated by rescaling the fitness values of each individual conform to the roulette wheel method (i.e. a random number between $[0,1]$ will choose an individual with a probability corresponding to its fitness value)

$$f_{\mathrm{i}}^{\mathrm{mod}} \;=\; \frac{\sum_{j,f_{\mathrm{j}}\leq f_{\mathrm{i}}} f_{\mathrm{j}}}{\sum_{j}^{N_{\mathrm{ind}}} f_{\mathrm{j}}}. \tag{3.2}$$

3.4.4. Elitism

A feature that is not present in natural systems is elitism, i.e. all individuals are replaced when they die. Elitism describes the practice of keeping the best N_{elit} individuals in the population when creating a new generation. On the one hand, this ensures that subsequent generations represent always an improvement; however, on the other, this feature can also strongly bias the system to local minima. In our case, the best N_{elit} individuals can only be replaced by better individuals, while all other individuals can (with a certain probability) always be replaced when a new individual enters the pool.

3.5. Genetic Operators

3.5.1. Crossover

The crossover operation is the most important one in a genetic algorithm. It defines how two (or more) parent individuals are to be combined to form a new

(and hopefully better) child individual [19, 69, 72, 73, 74, 75, 76]. We defined the crossover such that the lattice vectors are taken from one of the parents at random. We then sort the particles in both parent configurations in ascending order respective of their distance to a given plane (i.e. we "cut" the individuals). In a subsequent step, we pick a random number of particles from the first parent configuration and the remaining ones from the other one. Figure 3.2 illustrates the creation of a new individual from two parents. Using fractional coordinates in this context simplifies how well the parts of the two parents can be joined. The cutting direction should be random as well, but this can be taken into account by "shifting" both parents before sorting them [72].

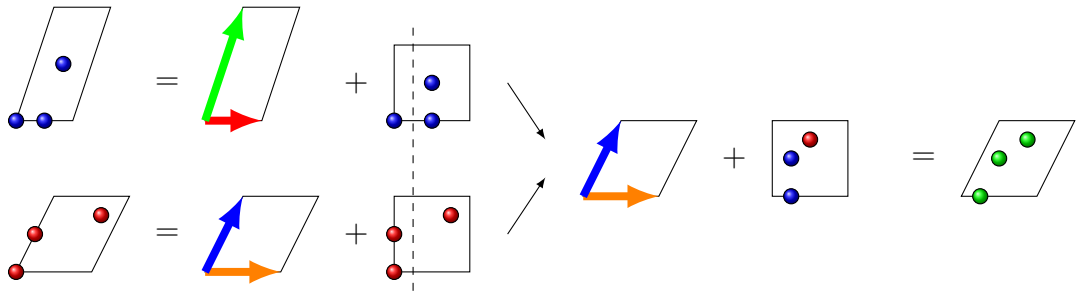

Figure 3.2.: Schematic representation of the crossover operation for a phenotype genetic algorithm. Left: first parent (top) represented as real cell, lattice vectors, and fractional coordinates. Second parent (bottom). Right: New individual, inheriting lattice from the second parent, and two and one fractional particle positions from first and second parent, respectively. The dashed line signifies the shift of fractional coordinates, corresponding to a random rotation before cutting.

3.5.2. Lattice Deformation

Especially for unit cells containing few particles, the lattice periodicity and thus the lattice vectors are of particular importance. A possible mutation operation for the crystal lattice is a random distortion. This can be expressed by multiplying

the matrix of the lattice vectors with a strain matrix [72]

$$\begin{pmatrix} a'_x & a'_y & a'_z \\ b'_x & b'_y & b'_z \\ c'_x & c'_y & c'_z \end{pmatrix} = \begin{pmatrix} 1+\epsilon_{11} & \frac{\epsilon_{12}}{2} & \frac{\epsilon_{13}}{2} \\ \frac{\epsilon_{21}}{2} & 1+\epsilon_{22} & \frac{\epsilon_{23}}{2} \\ \frac{\epsilon_{13}}{2} & \frac{\epsilon_{23}}{2} & 1+\epsilon_{33} \end{pmatrix} \cdot \begin{pmatrix} a_x & a_y & a_z \\ b_x & b_y & b_z \\ c_x & c_y & c_z \end{pmatrix} \quad (3.3)$$

where ϵ_{ij} are random Gaussian variables. Multiplication with the strain matrix disturbs the reduced expression of the lattice vectors, the resulting lattice therefore has to be reduced again (see section 1.3). A separate mutation operator to move particles around is not necessary, as the crossover itself can strongly disturb a given lattice.

3.5.3. Particle Reorientation

When using dipolar particles, the orientation of each particle is also of importance for the energy of the system. Local minima due to dipole orientation can be prevalent as chain formation is usually strong. In order to help the algorithm in "escaping" from local minima in energy, we introduced a mutation operator that randomly reorients a dipole. This is done by tilting the dipole by a Gaussian-distributed angle away from its original axis and subsequently rotating it a random angle $[0, 2\pi)$ around its original axis. This operation can be repeated for several particles.

3.5.4. Permutation

In binary mixtures, it can sometimes be advantageous to swap the particle kinds of two randomly chosen particles from time to time. We included such a procedure as our program also supports different particle kinds. For the systems presented in this work, such an operator is of no significance. A permutation mutation can also be repeated for several particles.

3.5.5. Lattice Squashing

For very low densities, some systems separate into layered crystals separated by large voids. Neighboring layers will only interact very weakly and convergence can be insufficient (if the energetically best structure is a uniform, non-layered crystal). We therefore also introduced a mutation that compresses or expands the unit cell in one direction and expands or contracts it in the other directions, leaving the volume of the unit cell constant.

3.6. Genetic Algorithm Parameters

For the genetic algorithm, we used a pool size $N_{\mathrm{ind}} = 10$ and an elitism parameter $N_{\mathrm{elit}} = 3$. In total, $N_{\mathrm{gen}} = 1,000$ individuals were created. For the fitness function, we used a parameter value $P_{\mathrm{fit}} = 3$. The probabilities for mutation were chosen as $p_{\mathrm{latt}} = 0.05$ for lattice deformation, $p_{\mathrm{rot}} = 0.02$ for dipole rotation, and $p_{\mathrm{squ}} = 0.05$ for lattice squashing. The Gaussian function uses a deviation of $\sigma_{\mathrm{str}} = V/6$ for the strain matrix and $\sigma_{\mathrm{rot}} = 0.5$ for the tilting angle during dipole rotation.

4. Optimization, Analysis and Miscellaneous

4.1. Local Optimization

While optimization tools based on genetic algorithms are suitable to cover a large variety of different candidate structures, the sheer size of the parameter search space can be troublesome. Local optimizations with very subtle energy differences can also prove difficult. In order to prevent problems in these cases, we *locally* optimize every candidate structure and then apply the genetic algorithm [77]. The algorithm we use for this is based on the L-BFGS method (see appendix A.3), a quasi-Newton method of optimization. As a consequence, the energy landscape in parameter space reduces to the local minima in energy (which represents, nevertheless, a considerably large number of possible points). Figure 4.1 shows a schematic representation of this local optimization for a single parameter and a fictitious genetic operation. Starting from individuals with low fitness values can take a long time to optimize. We therefore limited the L-BFGS algorithm to a maximum number of relaxation steps. In this work, we use the L-BFGS-B implementation by Zhu [78, 79].

4.2. Lattice Simplification

For a given ordered particle configuration, an infinite number of different representations as lattice vectors is possible. During local optimization and during the genetic algorithm run, configurations may end up strongly distorted (e.g. with

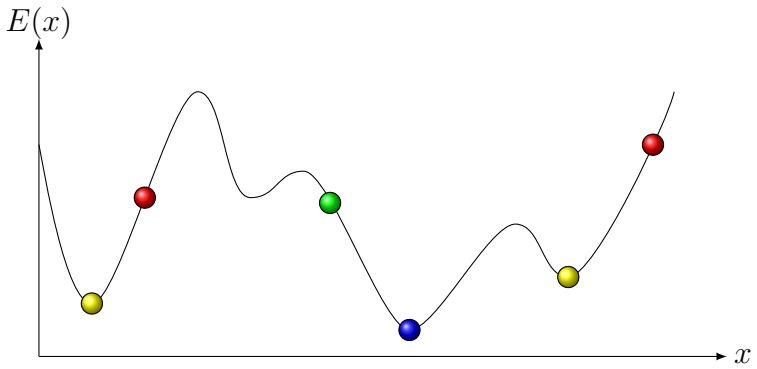

Figure 4.1.: Schematic representation of the local optimization. In a first step the red configurations are locally relaxed. The respective optimized configurations (yellow) are used to create new individuals (green configuration), which are again relaxed (blue configuration). In this schematic representation, only one parameter x needs to be optimized, whereas several dozen parameters are usually considered in our program. Effectively, the search space in this schematic representation reduces from a wide range of possible x-values to only four local minima. The operations of the genetic algorithm are used to hop between these basins and find even better configurations.

very thin and long unit cells). It is possible to transform these distorted lattices into equivalent, but more compact shapes. This makes them easier to understand and handle. In addition, it is also useful for the algorithm itself, since this step can even speed up energy calculations as fewer periodic images or **k**-vectors have to be taken into account. Figure 4.2 shows a schematic representation of lattice simplification in 2D. The quantity we try to minimize is the unit cell surface. We

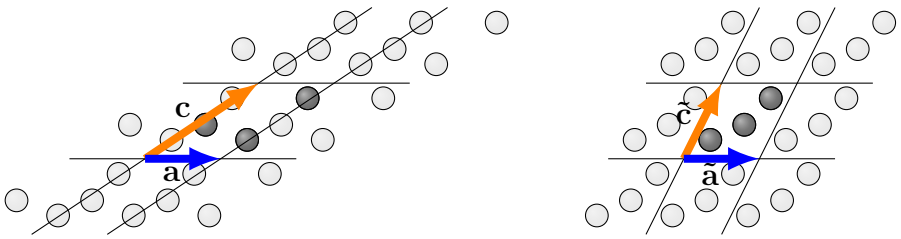

Figure 4.2.: Left: Distorted unit cell. Right: Simplified unit cell introducing $\tilde{\mathbf{c}} = \mathbf{c} - \mathbf{a}$. Note that the circumference (2D analogue to the surface) of the unit cell decreases while its area (2D analogue to the volume) remains unchanged. Actual calculations are carried out in 3D.

iteratively try to transform lattice vectors according to

$$\mathbf{a} \rightarrow \begin{cases} \mathbf{a} \pm \mathbf{b} \\ \mathbf{a} \pm \mathbf{c} \end{cases} \tag{4.1}$$

which leaves the unit cell volume unchanged, but changes the fractional coordinates of the particles (see appendix A.4).

4.3. Tabulation of Interaction Potentials

The calculation of computationally expensive functions can require a considerable fraction of the total run time of a genetic algorithm optimization. Especially incomplete Gamma functions, error functions, etc. can be problematic in this respect. In order to considerably speed up the program, we tabulated the most frequently used functions (as well as their derivatives, if required). From these tables, the respective function can be calculated much faster, using just a few

(simple) operations (see appendix A.5 for the exact expressions). We evaluated the functions

- $4\epsilon\sigma^\alpha r^{-\alpha}$
- $-4\epsilon\sigma^\alpha r^{-\alpha-1}$
- $4\epsilon\sigma^\alpha \frac{1}{\Gamma\left(\frac{\alpha}{2}\right)} r^{-\alpha}\Gamma\left(\frac{\alpha}{2}, \nu^2 r^2\right)$
- $4\epsilon\sigma^\alpha \frac{1}{\Gamma\left(\frac{\alpha}{2}\right)} \left(-\frac{\alpha}{r}\Gamma\left(\frac{\alpha}{2}, \nu^2 r^2\right) - 2\nu^\alpha \frac{\exp\left(-\nu^2 r^2\right)}{r}\right)$
- $4\epsilon\sigma^\alpha \frac{\pi^{\frac{3}{2}}}{\Gamma\left(\frac{\alpha}{2}\right)} \left(\frac{k}{2}\right)^{\alpha-3} \Gamma\left(\frac{3-\alpha}{2}, \frac{k^2}{4\nu^2}\right)$
- $4\epsilon\sigma^\alpha \frac{\pi^{\frac{3}{2}}}{\Gamma\left(\frac{\alpha}{2}\right)} \left[\frac{\alpha-3}{2}\left(\frac{k}{2}\right)^{\alpha-4} \Gamma\left(\frac{3-\alpha}{2}, \frac{k^2}{4\nu^2}\right) - \left(\frac{k}{2}\right)^{\alpha-3} \exp\left(-\frac{k^2}{4\nu^2}\right)\left(\frac{k}{2\nu}\right)^{1-\alpha}\right]$
- $B(r) = \frac{1}{r^3}\left[\frac{2\nu r}{\sqrt{\pi}} \exp(-\nu^2 r^2) + \mathrm{erfc}(\nu \mathrm{r})\right]$
- $C(r) = \frac{1}{r^5}\left[\frac{2\nu r}{\sqrt{\pi}}(3 + 2\nu^2 r^2) \exp(-\nu^2 r^2) + 3\mathrm{erfc}(\nu \mathrm{r})\right]$
- $D(r) = \frac{1}{r^7}\left[\frac{2\nu r}{\sqrt{\pi}}(15 + 10\nu^2 r^2 + 4\nu^4 r^4) \exp(-\nu^2 r^2) + 15\mathrm{erfc}(\nu \mathrm{r})\right]$
- $2\pi \exp\left(-\frac{k^2}{4\nu^2}\right) \frac{1}{k^2}$
- $-2\pi \exp\left(-\frac{k^2}{4\nu^2}\right)\left(\frac{2}{k^3} + \frac{1}{2k\nu^2}\right)$

for 40,000 values of r or k between a lower and an upper cutoff and stored the results in arrays. Using a quadratic interpolation, we can then evaluate these functions with high accuracy (the relative differences between interpolated and exact value of the different functions is then smaller than 10^{-7}) for any value of r or k. Below the lower cutoff, we used the exact function as the interpolation deviates significantly for inverse power and similar expressions. Above the upper cutoff, the function is simply set to zero (with actual function values usually below 10^{-9}). For the lower cutoff, in order to ensure appropriate accuracy, we choose $r_{\min} = 0.5\sigma$ in real space (which is only reached for very strong dipole moment and/or very high density) and $k_{\min} = 0.2/\sigma$ in reciprocal space. The choice of the reciprocal space cutoff can be trickier, especially for the quasi-2D approximation we use (where $\mathbf{c}$ is considerably longer than any other lattice vector and thus $\tilde{\mathbf{c}}$ is much shorter). For systems with many particles per unit cell (which is then also

larger for the same density), discrepancies in length between lattice vectors can be compensated by simplifying the unit cell (see section 4.2). The upper cutoff is R_{c} or R_{cut} in real space and K_{cut} in reciprocal space.

4.4. Optimizations for Speed

In order to speed up the execution of our program, we reorganized all summations so as to take advantage of negligible expressions, i.e. truncating as close to the cutoff radii as possible and using all symmetry relations. Some of the two-particle summations can be expressed as upper-triangle summations. It is also advantageous to only take into account periodic images that are not further away from the central unit cell than the cutoff radius (instead of simply repeating the unit cell a certain number of times in each direction)

$$\begin{aligned}\sum_{\boldsymbol{R}}{\sum_{\mathrm{i,j}}}' V\left(\boldsymbol{r}_{\mathrm{ij}}+\boldsymbol{R}\right) &= \sum_{\mathrm{n_a}=-\infty}^{\infty}\sum_{\mathrm{n_b}=-\infty}^{\infty}\sum_{\mathrm{n_c}=-\infty}^{\infty}{\sum_{\mathrm{i,j}}}' V\left(\boldsymbol{r}_{\mathrm{ij}}+n_{\mathrm{a}}\boldsymbol{a}+n_{\mathrm{b}}\boldsymbol{b}+n_{\mathrm{c}}\boldsymbol{c}\right) \quad (4.2)\\ &= \sum_{\mathrm{n_c}=-\mathrm{n_{c,max}}}^{\mathrm{n_{c,max}}}\sum_{\mathrm{n_b}=\mathrm{n_{b,min}}(\mathrm{n_c})}^{\mathrm{n_{b,max}}(\mathrm{n_c})}\sum_{\mathrm{n_a}=-\mathrm{n_{a,min}}(\mathrm{n_c},\mathrm{n_b})}^{\mathrm{n_{a,max}}(\mathrm{n_c},\mathrm{n_b})}{\sum_{\mathrm{i,j}}}' V\left(\boldsymbol{r}\right).\end{aligned}$$

These measures can reduce the number of necessary calculations by a factor of $\frac{4R^3\pi}{3}\frac{1}{(2R)^3}=\frac{\pi}{6}\simeq 0.524$ (see Fig. 4.3 for a schematic representation of cutoff optimization and appendix A.6 for the derivation of the analytical expressions describing this). Many functions depend only on the length of $\mathbf{r}$ or $\mathbf{k}$, so they are symmetric with respect to $\mathbf{r}\rightarrow-\mathbf{r}$ (antisymmetry is also given in many cases).

4.5. Parallelization

For the parallelization of our program, we used the MPIF90 compiler and runtime environment [80] on the cluster in our group and the Intel Fortran Compiler and runtime environment [81] on the JADE cluster (Montpellier, France). In both cases, the code is written in Fortan90. Typically 12-16 cores were used in parallel. One of these cores is devoted solely to managing the pool of individuals, while the others create and relax individuals.

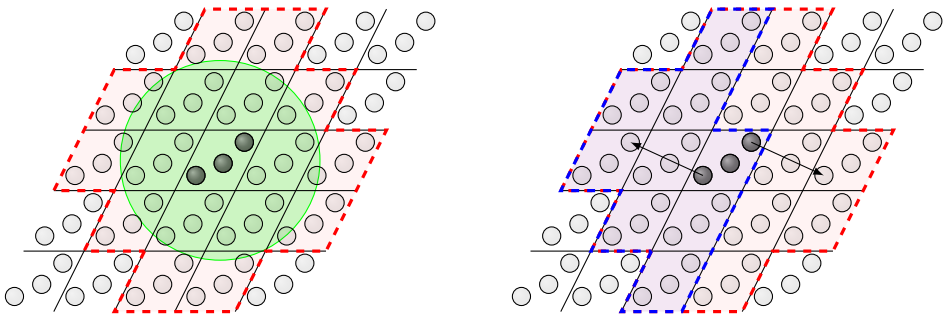

Figure 4.3.: Left: 2D schematic representation of cutoff optimization. Only the cells shaded in red (that are at least partly covered by the cutoff (green)) are included in the calculation. Right: 2D schematic representation of symmetry considerations to speed up energy calculations. Only the area shaded in blue is included in the calculations. The two interactions indicated by arrows can be included in the energy calculation by applying the interaction to both particles involved in one interaction. Actual calculations are performed in 3D.

4.6. Composite Energy Curves

In our algorithm, the number of particles per unit cell is constant during a run. As different structures may require a different number of particles per unit cell, this can be problematic, as we do not know *a priori* in all cases what structure to expect. For 3D systems, the simplest unit cell is very small [8], but quasi-2D unit cells can require considerably more particles (see section 5). A simple way to circumvent this problem is to choose a number of particles per unit cell that is divisible by many different natural numbers (e.g. 60 is divisible by 1, 2, 3, 4, 5, 6, 10, 12, 15, 20, 30, and 60 and can thus form unit cells with those numbers of particles perfectly). If the number of particles in our optimization is not the number of particles required by the energetically most favorable structure for given parameters (or a multiple thereof), the obtained result will be incorrect. Unfortunately, systems with $N \approx 60$ particles take a long time to optimize. We therefore chose to run our algorithm for different, smaller particle numbers and then determine the best configuration by comparing the obtained energies, e.g. if we do not know whether the system requires 2, 3 or 5 particles per unit cell,

running the genetic algorithm for each of these particle numbers will be a lot faster than running one for $N = 2 \times 3 \times 5 = 30$ particles. The resulting energy curve will be composed of systems of different sizes. For quasi-2D systems, we performed computations with $N = 1, 2, 3, 4, 5$ (which allows us to roughly determine the number of layers and where interesting regions are located) and, depending on the system, also with $N = 6, 8, 10, 12, 14, 18, 24$ particles. For some systems, we also performed computations with up to 28 particles, but no further improvements were found, at least for the soft-sphere system.

4.7. Order Parameters

While it is possible to classify particle configurations visually, i.e. by looking at a snapshot, this is impractical when carrying out many runs for different parameters. It is therefore useful to introduce so-called order parameters. These order parameters should correctly identify the different phases and can also be used to locate the phase transitions.

In our case, we are interested in rotational symmetries of our particle configurations. For a 2D system, one can define (as it is done in the literature [82, 83]) the order parameter for n-fold rotational symmetry Ψ_n as

$$\Psi_\mathrm{n} = \frac{1}{N} \sum_{\mathrm{i}=1}^{\mathrm{N}} |\Psi_\mathrm{n}(i)| \tag{4.3}$$

$$\Psi_\mathrm{n}(i) = \frac{1}{N_\mathrm{NN}(i)} \sum_{\mathrm{j}=1}^{\mathrm{N_{NN}(i)}} \exp(in\theta_\mathrm{ij}) \tag{4.4}$$

where θ_ij is the angle between the vector $\mathbf{r}_\mathrm{ij}$, which connects particles i and j, and a reference axis; $N_\mathrm{NN}(i)$ is the number of nearest neighbors for particle i. These order parameters are $\Psi_\mathrm{n} = 1$ for perfect n-fold rotational symmetry and small or zero when such a symmetry is not present. In 3D systems, spherical harmonics are necessary to calculate appropriate order parameters (see appendix A.7). In our case, we follow the order parameters as calculated by [84, 85]. In a slab geometry, full 3D rotational symmetry can be found inside the slab, but not close to the walls.

As will be discussed in section 5, layered configurations are very common in slab geometries, but intermediate phases may exhibit buckling and other phenomena. In order to accommodate these possibilities, we defined order parameters based on the 2D expressions but adapted for different height and different structures of the layers (see appendix A.8). Nearest neighbors can, in any dimension, be determined via a Voronoi construction (see appendix A.9). Again, this approach has to be suitably adapted for slab geometries. Possible improvements here would be to develop order parameters that are able to describe the transition from 2D order parameters (slab thickness $h = 0$) to 3D order parameters ($h = \infty$). For parts of the analysis of the 3D system we also employed the FINDSYM program package [86], which computes all rotational symmetries of a given crystal cell, as well as its space group and other information.

4.8. Visualization

In order to visualize our results, we used the program package PyMOL [87] which allows us to plot both the particles and the dipole moments associated with them, as well as the walls for slab geometries. Note that in all snapshots shown in section 5 the particles are not drawn to scale in an effort to retain good visibility even for overlapping particles; thus, the blue spheres should be regarded as representations of the centers of the particles. The dipole moments (shown as orange cones) signify only the direction of the corresponding moment, but not its strength. The length of such a cone is equal to the real particle diameter. The walls for slab geometries are shown (in part) as grey planes. They are drawn at a distance h from each other (i.e. signifying the hard boundaries for the particle *centers*, compare Fig. 2.5). These planes also allow for easy verification of the structure of the system at the wall. For plotting energy and order parameter curves we employed the program package Xmgrace [88].

5. Results

While we were able to reproduce some of the results for 3D Stockmayer systems [8, 70], we did not observe any new structures.

For the quasi-2D system, we will always use $\alpha = 12$ for the exponent in the spherically symmetric inverse power law potential (see equ. 1.2) and a fixed volume (i.e. we will perform isochoric optimizations).

5.1. Soft Sphere Interaction

In a first step, we investigated systems of soft spheres (i.e. $\mu^* = 0$) and compared the results to data available in the literature. We chose densities $0.5 \leq \rho_{\mathrm{H}} \leq 1$ and slab widths $0.01\sigma \leq h \leq 3\sigma$. Figure 5.1 shows the rescaled energy curves for different densities as functions of h. The relevant particle numbers per unit cell in this region are $N = 2, 3, 4, 6, 8, 12, 14, 18, 24$. The curves shown here are composed of the curves corresponding to the best configurations for particle numbers $N = 1, 2, 3, 4, 5, 8, 12, 10, 14$. Figures 5.2 and 5.3 show the energy curve for $\rho_{\mathrm{H}} = 1$ and for interesting regions, i.e. where intermediate phases occur, respectively.

The transitions between the different phases are much easier to identify using the order parameters described in section 4.7. Apart from the identification of the simple triangular or square phases, it is also possible to locate intermediate phases (see Fig. 5.4). Figure 5.5 shows the order parameters for all investigated densities. As mentioned in section 4.7, Ψ_4 and Ψ_6 are somewhat less adequate for identifying triangular and square phases.

In order to characterize the different phases, we have used the same nomenclature as in [89, 90], i.e. $n\triangle$ and $n\square$ denote systems of n layers with triangular or square

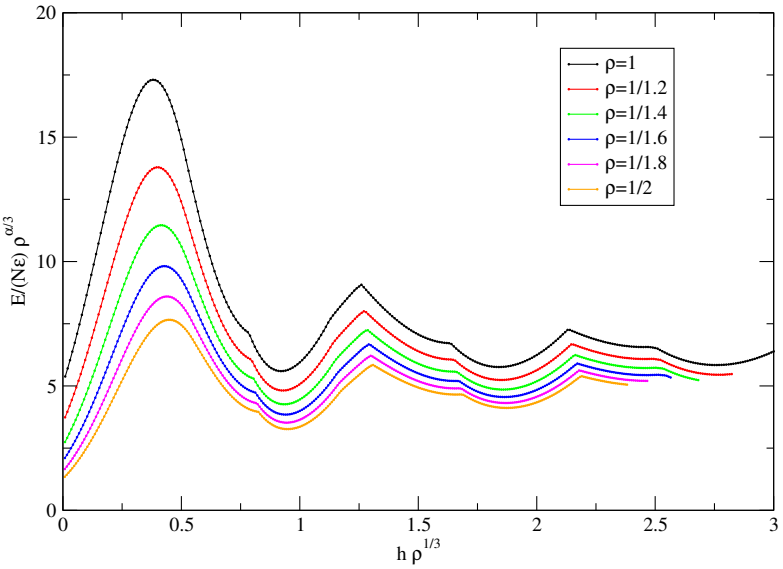

Figure 5.1.: Rescaled energy curves for different densities of soft spheres in a slab geometry. Most transitions between phases can be observed as kinks in the energy curve. The region where the energy is large corresponds to the forbidden region for hard spheres, i.e. particles overlap in this region for the given densities.

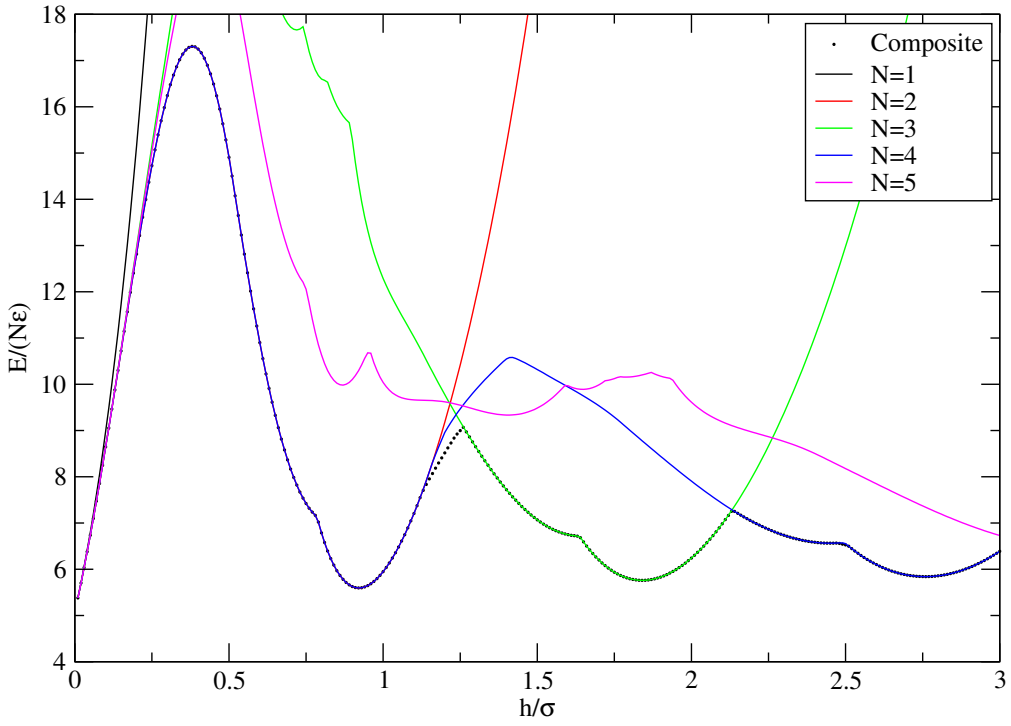

Figure 5.2.: Energy curves for different numbers of particles per unit cell in a soft sphere system with $\rho_H = 1$. As can be seen, perfectly layered systems are well described by a single particle per layer. Only for the considerably more complicated intermediate phases more particles are necessary to form the correct structure.

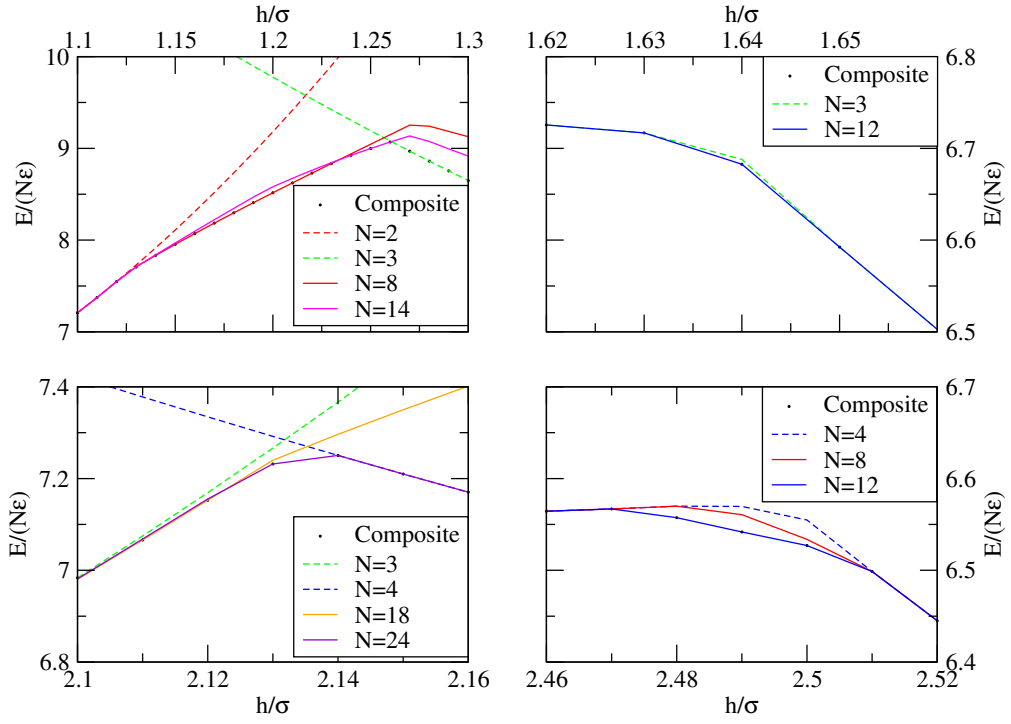

Figure 5.3.: Enlarged views for regions where intermediate phases occur (compare Fig. 5.2).

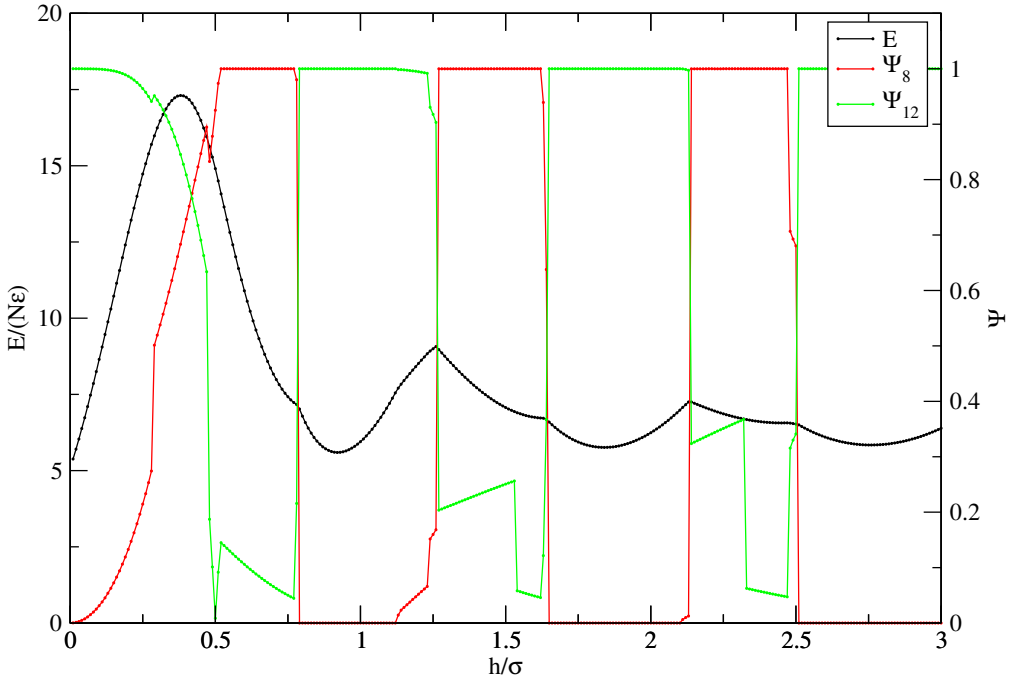

Figure 5.4.: Order parameters in a soft sphere system with $\rho_H = 1$. Phase transitions coincide with changes in order parameter and kinks in the energy. Note that intermediate phases are present at almost all transitions (i.e. order parameters do not change in a perfect step). The sudden changes in order parameter that do not coincide with kinks in the energy are due to artifacts in the order parameter calculation (see section 4.7 and appendix A.9).

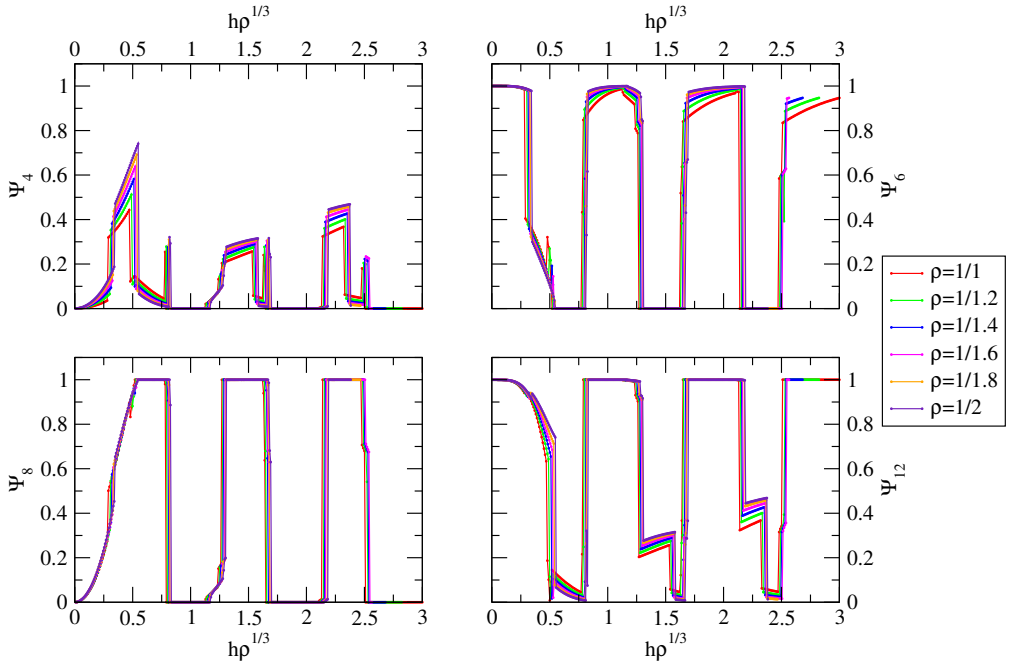

Figure 5.5.: Order parameters in a soft sphere system. When rescaling the slab thickness by $h\rho_{\mathrm{H}}^{\frac{1}{3}}$, the sequence of the phases and their range of stability are almost identical.

layout, respectively. This nomenclature is commonly used for hard sphere systems and also well applies in the soft sphere case. To better describe some of the observed buckling phases, we introduce the symbols $1\triangle(a,b)$, which denotes a zigzag buckling phase where the path following the particles in a given sublayer can be described by (a,b). In particular, a steps along the 0°-direction are followed by b steps along the 60°-direction (see Fig. 5.6). In actual systems, the basic triangular lattice will be distorted, in particular close to the transition from one to two layers.

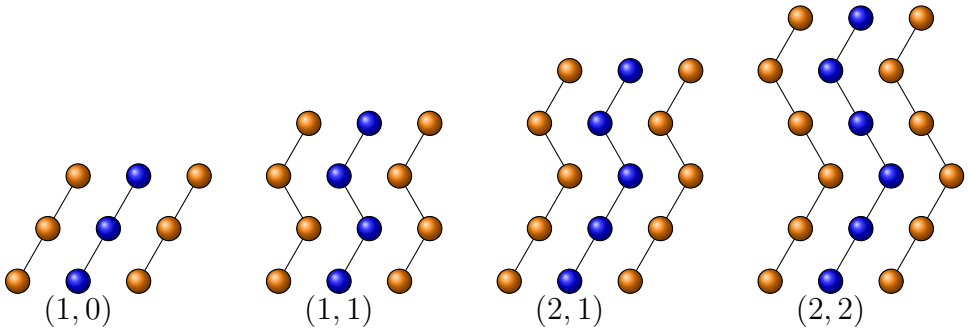

Figure 5.6.: Schematic representations of different possible $1\triangle$ buckling phases. From left to right: $1\triangle(1,0)$ (requires $N = 2$ particles), $1\triangle(1,1)$ (requires $N = 4$), $1\triangle(2,1)$ (requires $N = 6$), and $1\triangle(2,2)$ (requires $N = 8$). The blue and orange particles occupy the slightly raised and lowered sublayers, respectively. In our computations, a contraction perpendicular to the creases may also be observed.

The complete sequence of phases for increasing slab width h is: $(1\triangle) \to 1\triangle(1,0) \to 2\square \to I_1 \to 2\triangle \to I_2^* \to I_2^{**} \to I_2 \to I_3 \to 3\square \to I_4 \to 3\triangle \to I_5 \to I_6 \to 4\square \to I_7 \to 4\triangle$ (see Fig. 5.8 to 5.15 for snapshots of each of the different phases). The $1\triangle$ phase is denoted in parentheses as it is never achieved for finite slab thickness $h > 0$. The I_x phases denote the different intermediate phases.

In the following, we will give a closer description of the sequence of occurring phases and of the locations of the transitions for $\rho_\mathrm{H} = 1$ (see Fig. 5.7 for the full phase diagram).

As the soft sphere potential is purely repulsive, the system immediately separates

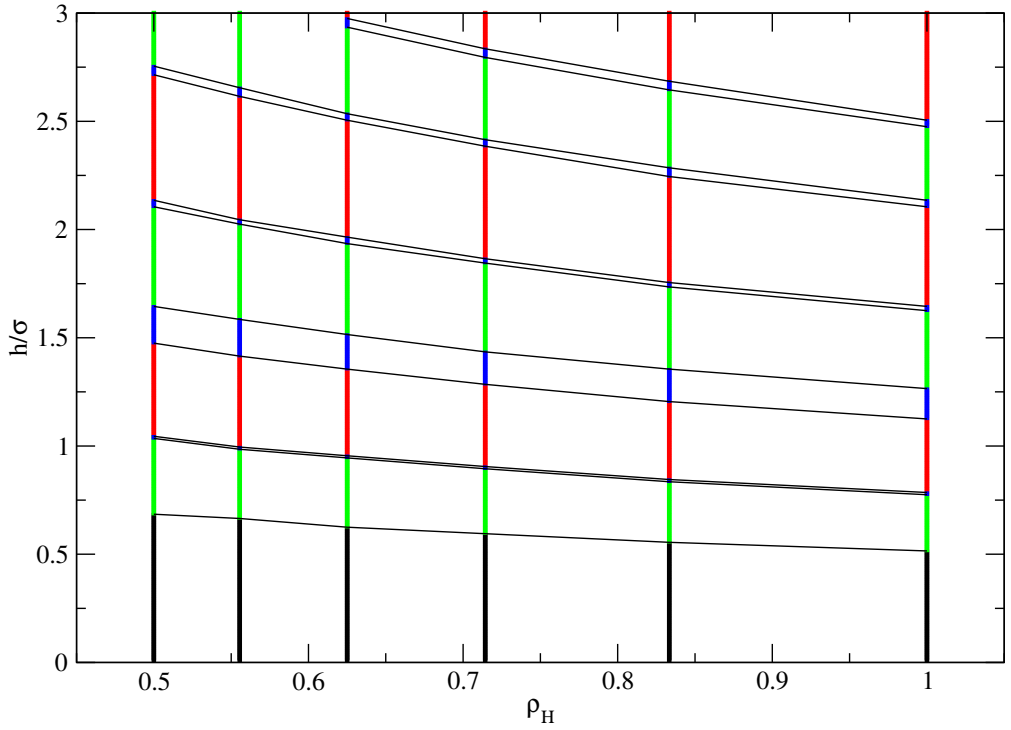

Figure 5.7.: Full phase diagram of the soft sphere system in slab geometry. Square phases in green, triangular phases in red, intermediate phases in blue, and linear buckled phase in black. The black lines indicate the transitions. The general sequence of $n\square \to n\triangle \to (n+1)\square$ is recovered, but many intermediate phases are discovered.

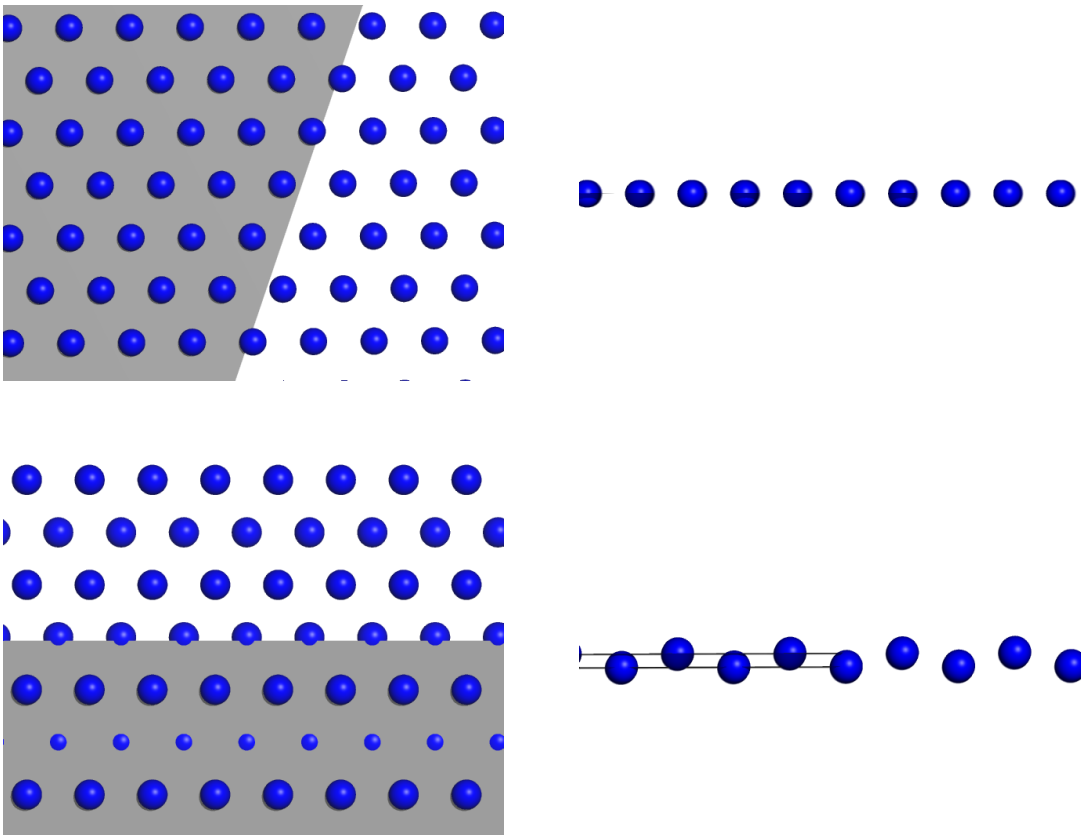

Figure 5.8.: Snapshots of the soft sphere system, showing the (for finite slab thickness unachievable) monolayer $1\triangle$ (top) and the buckled $1\triangle(1,0)$ (bottom) phases. Top views on the left, side views on the right. The blue spheres are not drawn to scale. The grey areas represent planes parallel to the walls at a distance of $\sigma/2$.

into two sub-layers for finite slab width $h > 0$. This separation is achieved by half of the particles positioning themselves in chains at the top wall and the other half at the bottom wall (see Fig. 5.8). The distances between neighboring chains are slightly contracted with respect to a perfect triangular lattice. The transition $1\triangle(1,0) \rightarrow 2\square$ is smooth. The sub-layers are arranged in a rectangular lattice and as they separate further, this transforms into a square lattice. For $\rho_{\mathrm{H}} = 1$, the $1\triangle$ phase is stable only at $h = 0$, while the buckled $1\triangle(1,0)$ phase is stable for $0 < h < 0.52\sigma$ (i.e. at that point eight-fold symmetry is complete). While only one particle per unit cell is necessary to represent the $1\triangle$ monolayer, at least two are required for the $1\triangle(1,0)$ phase.

The transition $2\square \rightarrow 2\triangle$ is achieved via an intermediate phase I_1. The $2\square$ phase is stable for $0.52\sigma \leq h < 0.78\sigma$. The intermediate I_1 phase is stable for $0.78\sigma \leq h < 0.79\sigma$ and the $2\triangle$ phase is stable for $0.79\sigma \leq h < 1.13\sigma$. The $2\square$ and $2\triangle$ phases form perfect bilayers (no deformation in z-direction) with square and triangular lattices within layers (see Fig. 5.9). They both require only two particles per unit cell. The intermediate phase is a distorted form of either $2\square$ or $2\triangle$ where neighboring lines shift so as to get closer to a triangular arrangement (see Fig. 5.9). Note that the region where the intermediate I_1 phase is stable is so small, that it will probably be difficult to observe it in finite temperature simulations and even more so in experimental systems. To form the intermediate I_1 phase, two particles per unit cell are required.

The transition from two to three layers (i.e. $2\triangle \rightarrow 3\square$) is achieved via two intermediate phases I_2 and I_3 and several preliminary intermediate phases I_2^* and I_2^{**}. The I_2 and I_3 phases are stable for $1.14\sigma \leq h < 1.24\sigma$ and $1.24\sigma \leq h < 1.27\sigma$, respectively. The I_2 intermediate phase is achieved by a fourth of the particles from both layers separating from the wall and forming sub-layers (see Fig. 5.10). The particles remaining in the layers at the walls form a lattice consisting of one hexagon and two triangles per unit cell. The two sub-layers are positioned such as to maximize the distance between their constituent particles. Note that the two sub-layers combined contain only two thirds of the particles of a layer remaining at the wall. In total, eight particles per unit cell are necessary to form the intermediate I_2 phase. The I_3 intermediate phase has an even more complicated structure with 14 particles per unit cell. In this case, two sevenths of the parti-

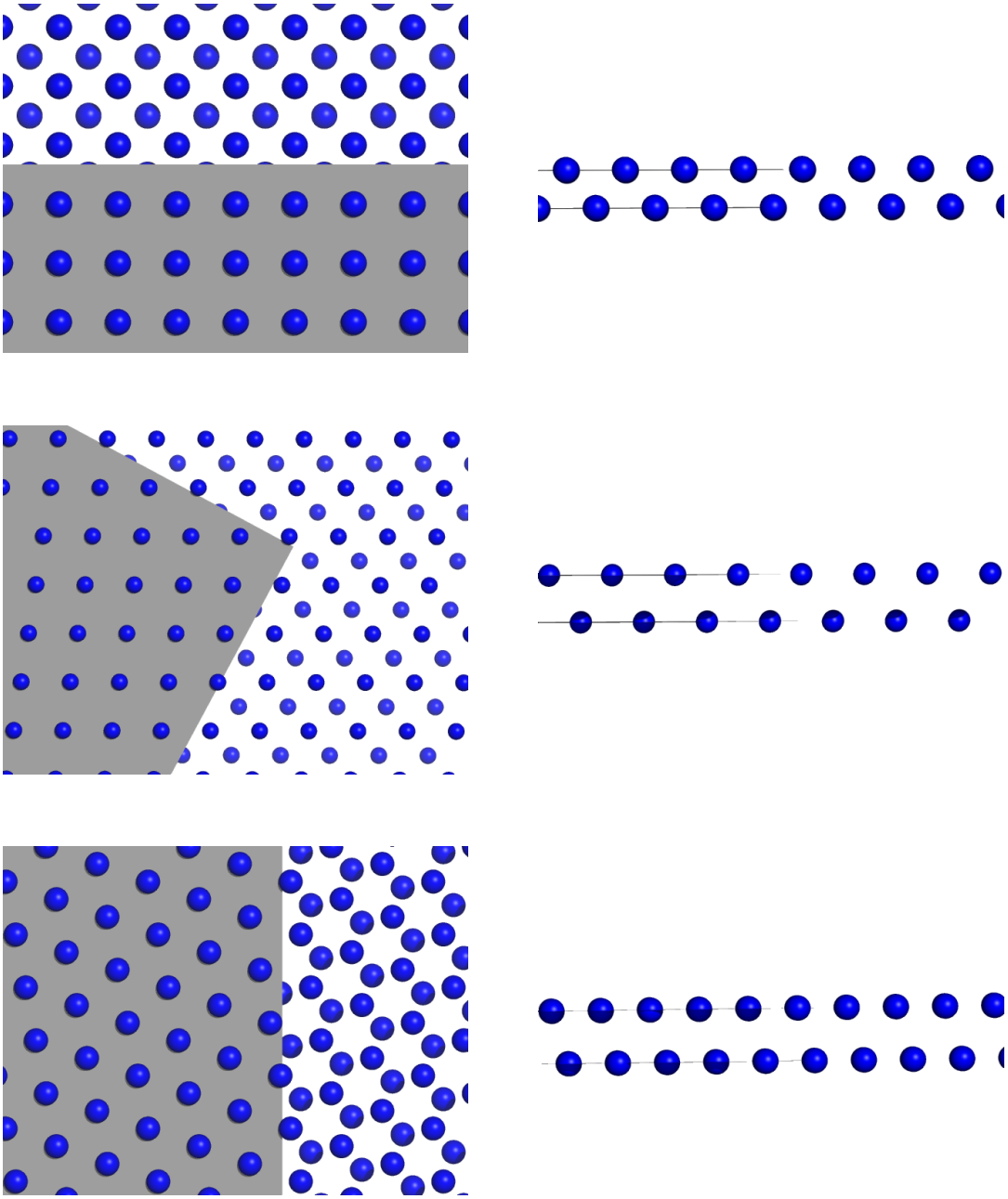

Figure 5.9.: Snapshots of the soft sphere system, showing the 2□ (top), the intermediate I_1 (center) and the 2△ (bottom) phases. Top views on the left, side views on the right. The blue spheres are not drawn to scale. The grey areas represent planes parallel to the walls at a distance of $\sigma/2$.

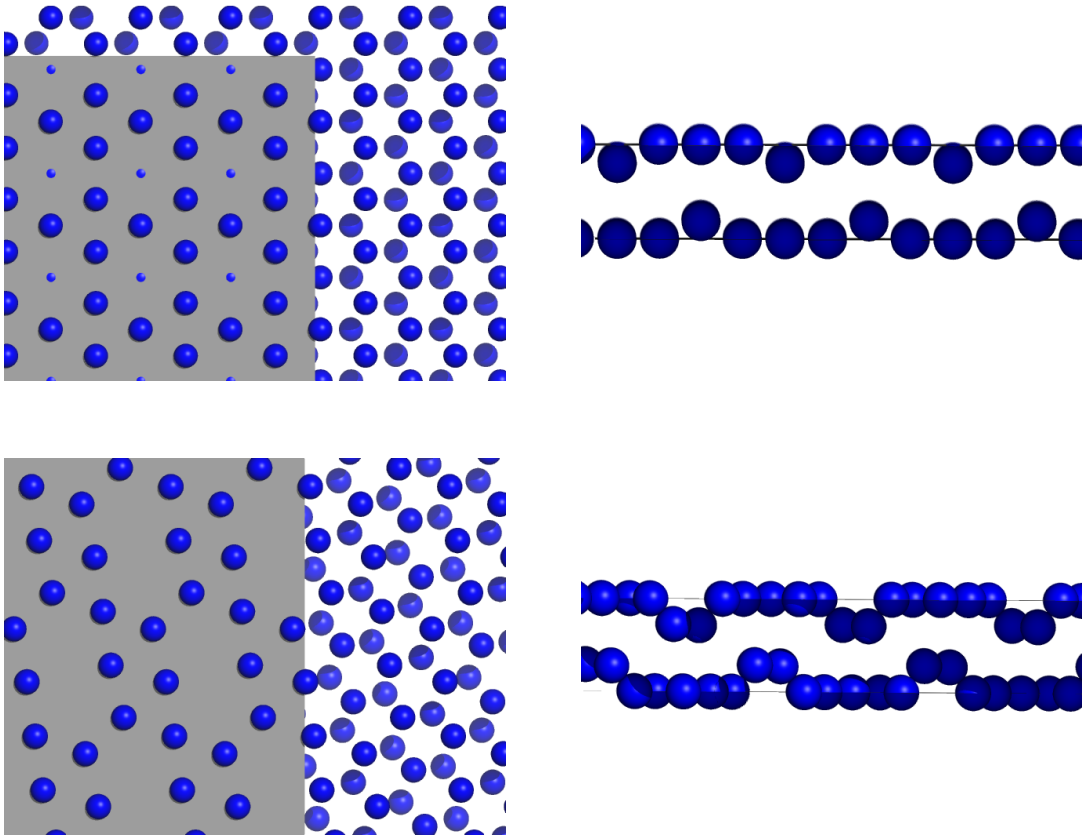

Figure 5.10.: Snapshots of the soft sphere system, showing the intermediate I_2 (top) and the intermediate I_3 (bottom) phases. Top views on the left, side views on the right. The blue spheres are not drawn to scale. The grey areas represent planes parallel to the walls at a distance of $\sigma/2$.

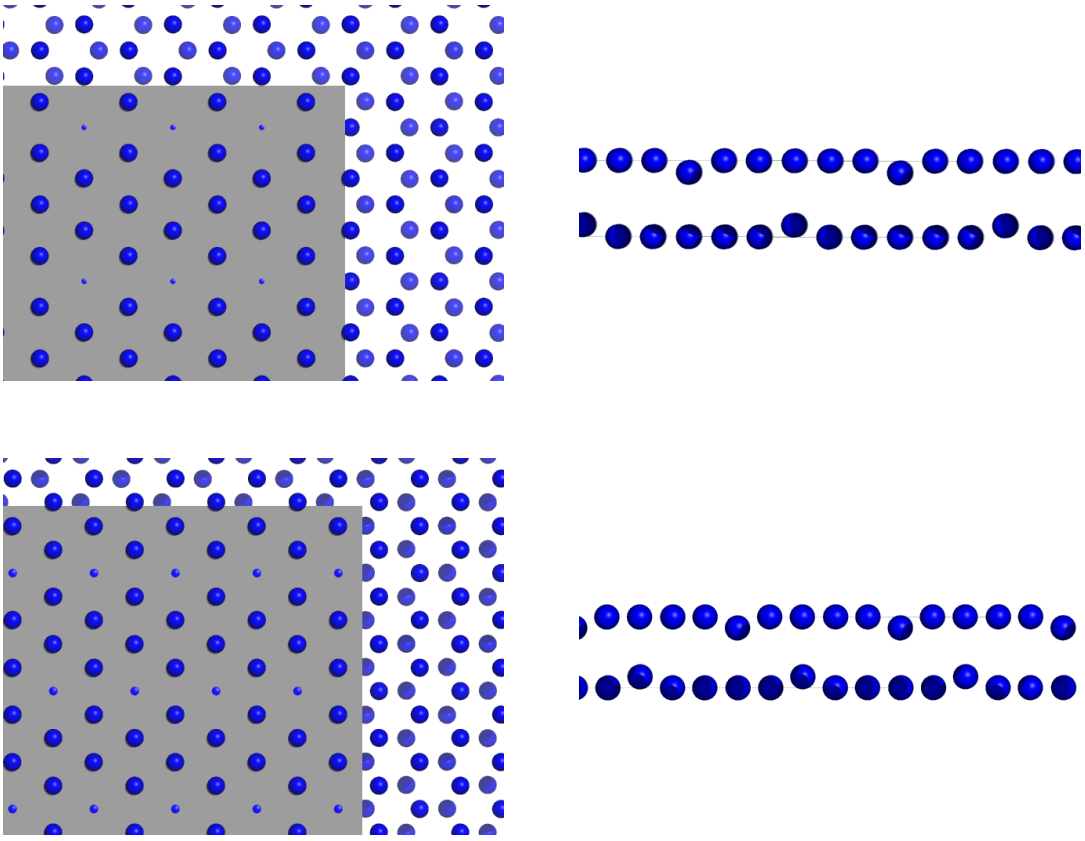

Figure 5.11.: Snapshots of the soft sphere system, showing the intermediate I_2^* (top) and the intermediate I_2^{**} (bottom) phases. Top views on the left, side views on the right. The blue spheres are not drawn to scale. The grey areas represent planes parallel to the walls at a distance of $\sigma/2$.

cles separate from the walls. The particles remaining at the walls form a lattice composed of an elongated hexagon and four triangles (see Fig. 5.10). The sub-layers themselves also have a complicated structure as the two particles in each of the sub-layers do not separate the same distance from the wall. The region where either of the intermediate phases is stable extends over a range which might be accessible for simulations at finite temperatures. However, we have to take into account that the energy differences between intermediate phases and layered phases can be very small; they also depend on the density. For $\rho_{\mathrm{H}} = 1$, there is an intermediate I_2^{**} phase which occurs as an intermediate step at the transition $2\triangle \rightarrow I_2$ ($1.13\sigma \leq h < 1.14\sigma$). This structure is similar to the I_2 intermediate phase, but with fewer particles detached from the wall (only one fifth). For other densities, we have also observed the I_2^* intermediate structure, where one sixth of the particles detach from the walls. Figure 5.11 shows these two phases. From the general order of phases and their separation ration (i.e. the ratio of particles in the intermediate layers to particles at one wall, see Fig. 5.12) we can say that the intermediate phases are ordered with increasing separation ratio (0.4 for I_2^*, 0.5 for I_2^{**}, 0.66 for I_2 and 0.8 for I_3). The fact that not all of the preliminary intermediate phases appear in our computations for all densities is most likely due to our step size in h (i.e. all of the phases can probably be observed if a sufficiently small step size is used). The regions where some of these phases are energetically most favorable are extremely small. Moreover, it is highly probable that even more intermediate phases arise in more detailed investigations or for more particles per unit cell. The best configuration is probably determined such that the separation ratio goes from 0 ($2\triangle$) to 1 ($3\square$) continuously.

The $3\square$ phase is stable for $1.27\sigma \leq h < 1.63\sigma$, the $3\triangle$ phase for $1.65\sigma \leq h < 2.11\sigma$. Again, these phases are made up of perfect layers, requiring only three particles per unit cell. In between these two phases, the intermediate I_4 phase is stable ($1.63\sigma \leq h < 1.65\sigma$). The structure of this phase is highly complicated (see Fig. 5.13). On a 2D level, the layers form a distorted elongated triangular tiling (i.e. the unit cell consists of a square and two triangles). The 3D arrangement exhibits substructures with stronger order. These substructures are equilateral triangular prisms parallel to the surface. Such substructures are present at both walls and are slightly shifted with respect to each other. The length of the prism coincides

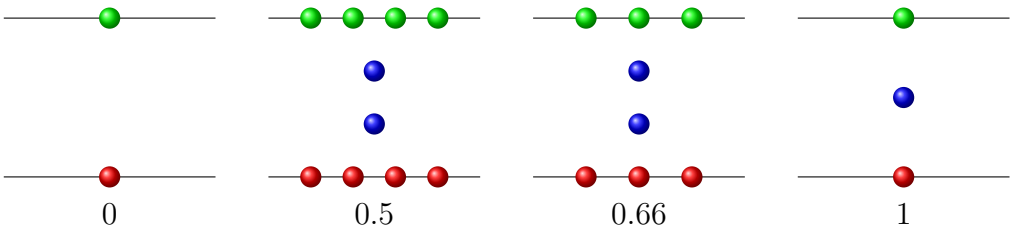

Figure 5.12.: Schematic representation of the separation ratio. Shown here is the transition from two to three layers. As more and more particles separate from the wall layers (red and green) to form the intermediate layer (blue), the separation ratio, i.e. the ratio of the number of particles in the intermediate layer to the number of particles in one of the wall layers, increases from 0 to 1.

with the distorted squares. Similar structures have been observed in hard sphere systems [91]. Six particles per unit cell are needed to form the I_4 structure.

The transition from three to four layers ($3\triangle \rightarrow 4\square$) is marked by two intermediate phases I_5 and I_6. These are stable in very narrow h-ranges, namely for $2.1\sigma \leq h < 2.13\sigma$ and $2.13\sigma \leq h < 2.14\sigma$, respectively. The I_5 intermediate phase (see Fig. 5.14) differs from the $3\triangle$ phase insofar as the center layer buckles. The interesting point here is that this buckling is not symmetric, i.e. the center layer separates into sublayers with a ratio two to one. This structure is, in contrast to all other observed structures, not invariant upon inversion of the z-axis (and a subsequent translation). This loss of a basic symmetry might be indicative that this structure is not thermodynamically stable and that closer investigations are necessary. In total, nine particles per unit cell are required to form this structure, the (forming) sublayers contain 0.33 and 0.66 times as many particles as a wall layer, respectively. The I_5 phase is followed by the I_6 intermediate phase. This structure consists of 24 particles per unit cell. The buckling is once again symmetric and the wall layers are also broken up, similar to the transition from two to three layers. The (forming) two central layers each contain 0.71 times as many particles as a wall layer. Similar as for the $2\triangle \rightarrow I_2 \rightarrow I_3 \rightarrow 3\square$ transition, we possibly obtain more intermediate phases for closer investigations, the slab width regions of stability are, however, very small. A fundamental difference is that once a central layer

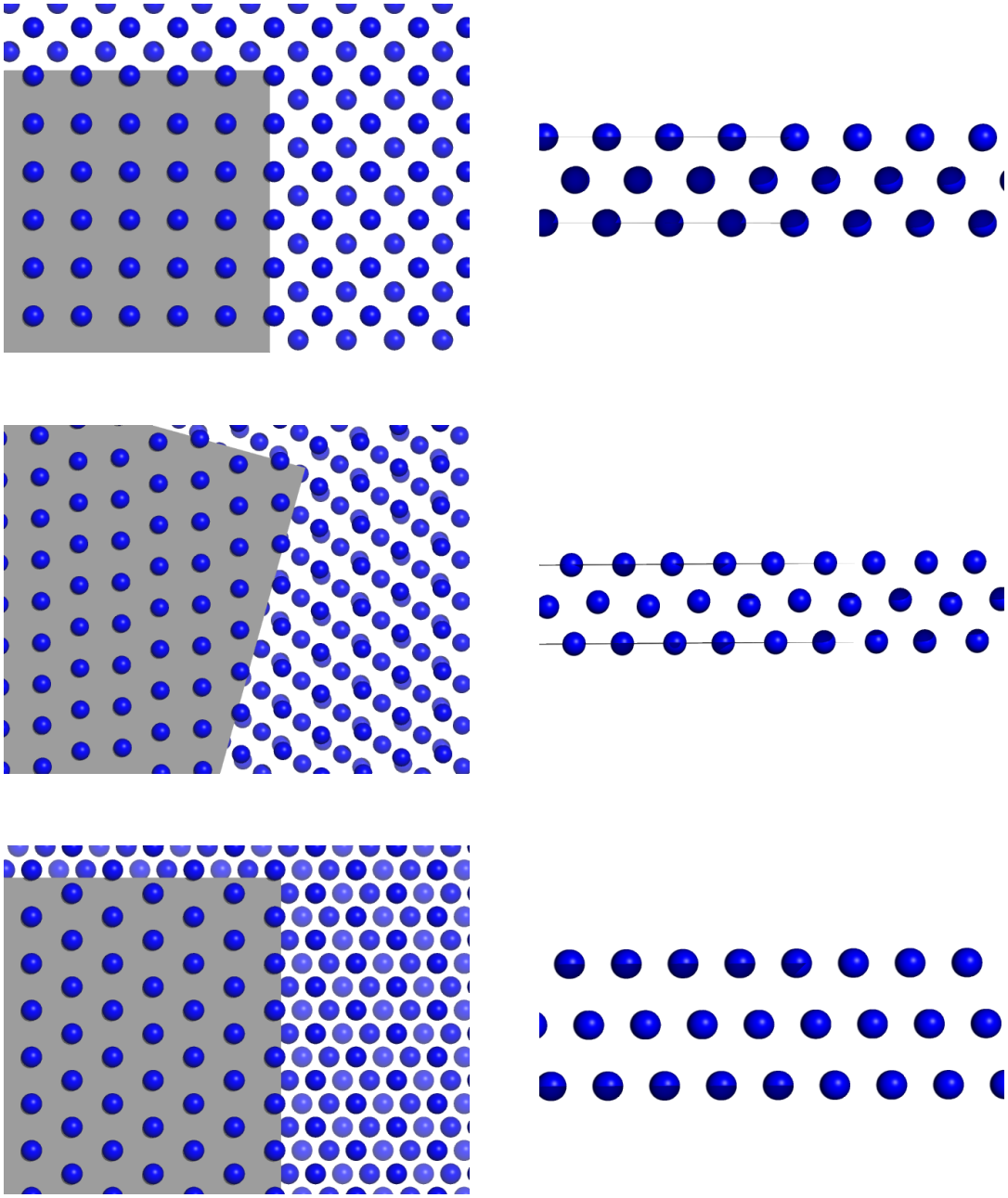

Figure 5.13.: Snapshots of the soft sphere system, showing the 3□ (top), the intermediate I_4 (center) and the 3△ (bottom) phases. Top views on the left, side views on the right. The blue spheres are not drawn to scale. The grey areas represent planes parallel to the walls at a distance of $\sigma/2$.

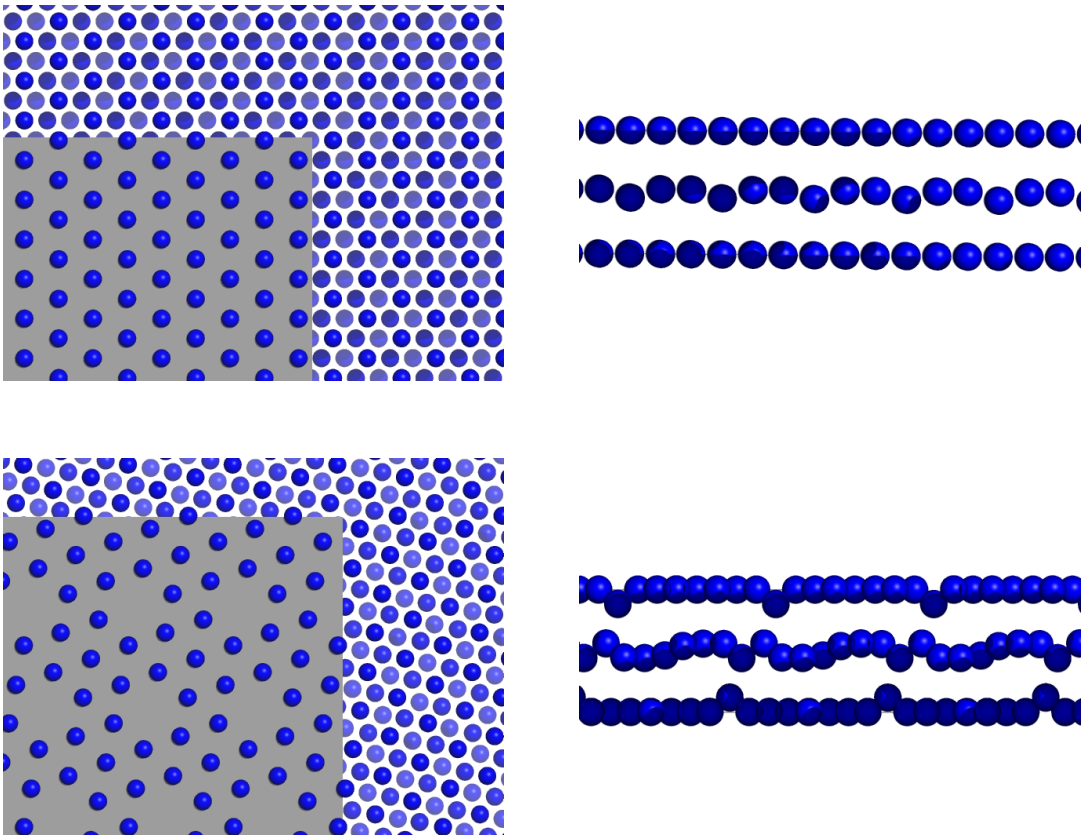

Figure 5.14.: Snapshots of the soft sphere system, showing the intermediate I_5 (top) and the intermediate I_6 (bottom) phases. Top views on the left, side views on the right. The blue spheres are not drawn to scale. The grey areas represent planes parallel to the walls at a distance of $\sigma/2$.

is involved, symmetry upon inversion of the z-axis is not necessarily conserved. It might be interesting to investigate this transition at finite temperatures or for systems with more particles per unit cell (in this work, we tried up to 28 particles). The $4\square$ phase is stable for $2.14\sigma \leq h < 2.48\sigma$, the $4\triangle$ phase for $2.51\sigma \leq h \leq 3\sigma$ (i.e. the upper boundary of the investigated region). Once more, these phases are made up of perfect layers, requiring only four particles per unit cell. In between these two phases, the intermediate I_7 phase is stable ($2.48\sigma \leq h < 2.51\sigma$). The structure of this phase is very similar to the I_4 phase, just for four instead of three layers (see Fig. 5.15), thus requiring twelve particles per unit cell to represent. On a 2D level, the layers form a distorted lattice consisting of two squares and two triangles per unit cell (basically an elongated triangular tiling with an additional square). The 3D arrangement consists of equilateral triangular prism substructures close to the top and bottom walls that are then shifted slightly with respect to each other. The base of the prism has twice the side length as the one in the I_4 intermediate phase. The length of these prisms coincides with the rows of two distorted squares.

5.2. Dipolar Soft Sphere Interaction

When adding a dipolar interaction, the number of parameters to optimize increases significantly, leading to a considerable increase in required computational time. Moreover, the energetically most favorable configurations are significantly more complex. This is especially true for the intermediate phases. We therefore restricted our investigations to slab thicknesses $0.01\sigma \leq h \leq \sigma$. In this region, the system forms at most a bilayer. We ran our genetic algorithm for dipole moments $\mu^* = 1$ and $\mu^* = 2$ and densities $0.5 \leq \rho_{\mathrm{H}} \leq 1$. Figure 5.16 shows the energy curve for $\rho_{\mathrm{H}} = 1$ both for $\mu^* = 1$ and $\mu^* = 2$ for different particle numbers per unit cell. The linear $1\triangle(1,0)$ buckling observed for the soft sphere system is still present for small slab thickness (compare section 5.1). Figure 5.17 shows the behavior of the order parameters with increasing slab width. Note the significantly weakened order due to the contraction of the lattice caused by the formation of dipole head-to-tail chains (see snapshots in Fig. 5.19 and 5.20).

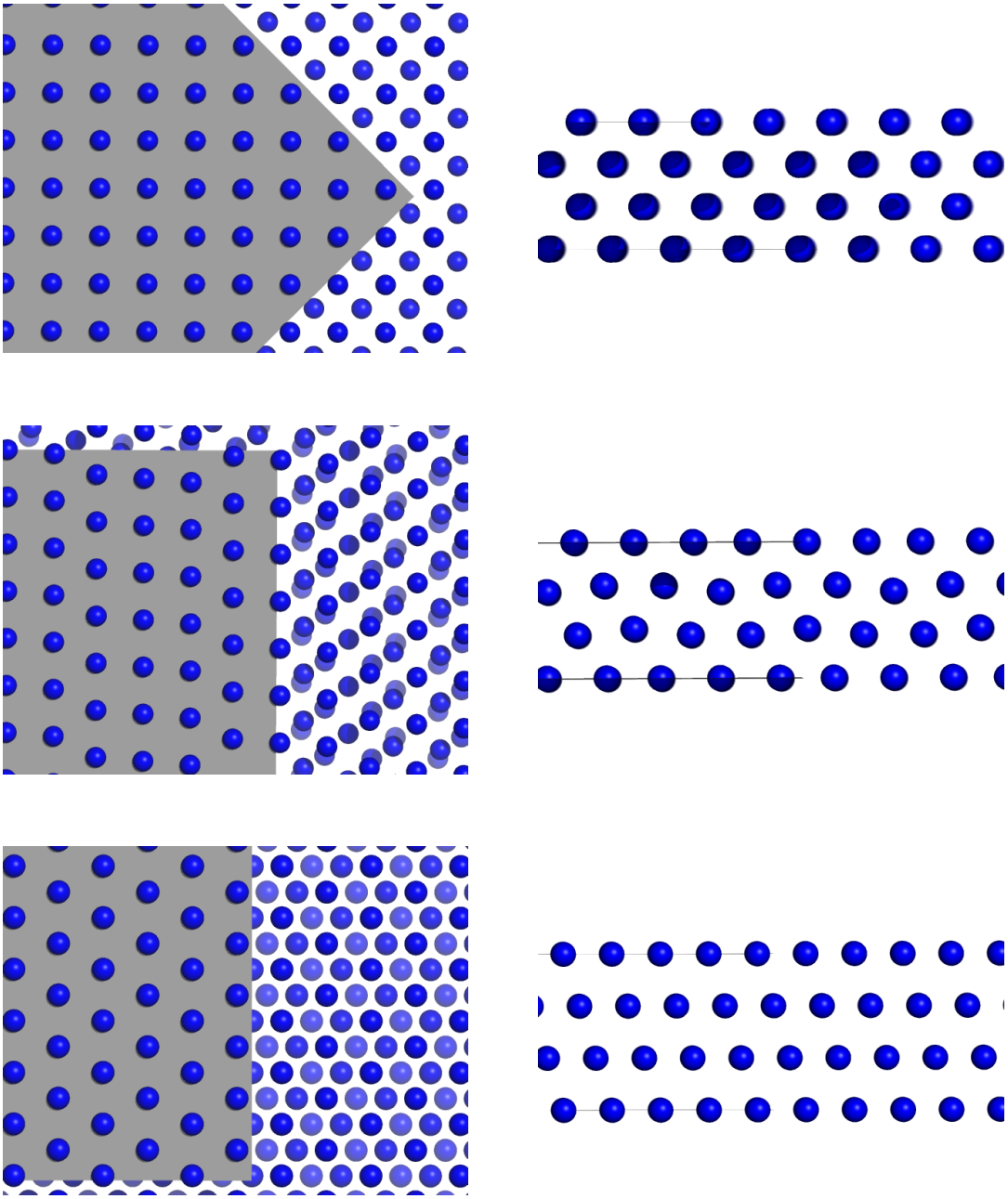

Figure 5.15.: Snapshots of the soft sphere system, showing the 4□ (top), the intermediate I_7 (center) and the 4△ (bottom) phases. Top views on the left, side views on the right. The blue spheres are not drawn to scale. The grey areas represent planes parallel to the walls at a distance of $\sigma/2$.

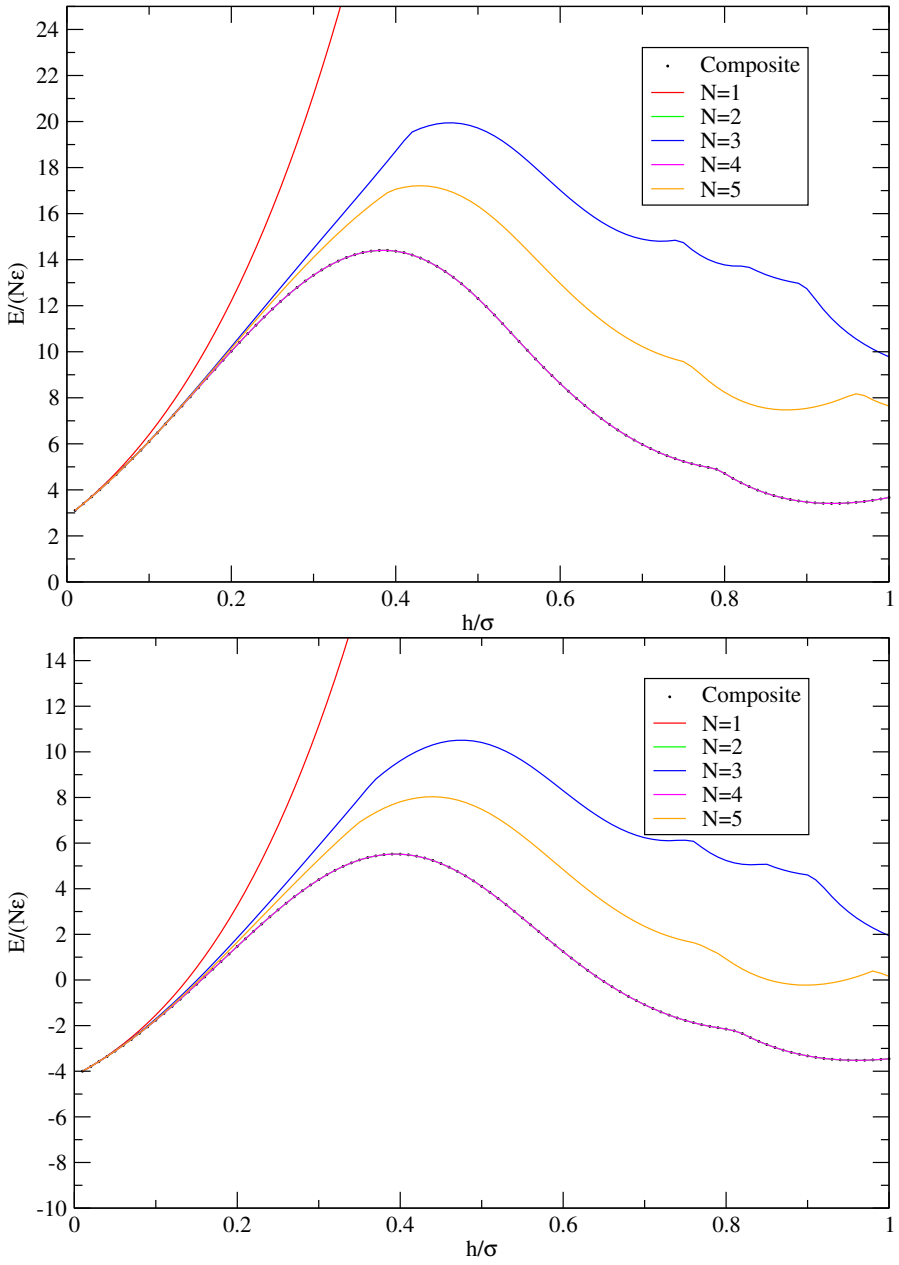

Figure 5.16.: Energy curves for different numbers of particles per unit cell N in a dipolar soft sphere system with $\rho_{\mathrm{H}} = 1$. Top: $\mu^* = 1$. Bottom: $\mu^* = 2$.

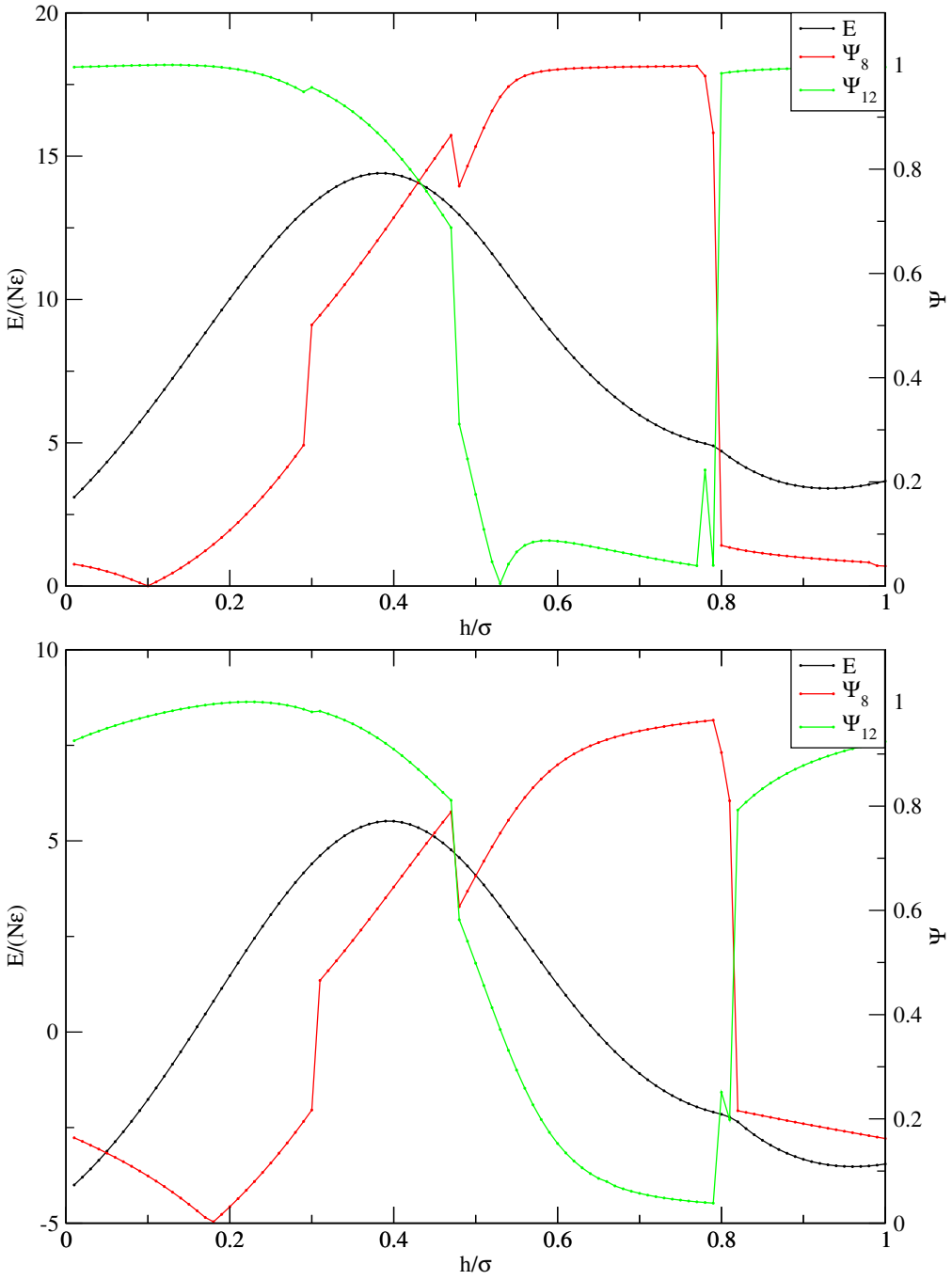

Figure 5.17.: Order parameters in a dipolar soft sphere system with $\rho_{\mathrm{H}} = 1$. Top: $\mu^* = 1$. Bottom: $\mu^* = 2$. Note the weakened order compared to soft sphere systems (see section 5.1).

In some experimental systems [12, 92] as well as in several simulation studies [90, 93], zig-zag buckling phases have been observed. When no external field is applied, the dipoles align within layers (i.e. parallel to the walls in the x-y-plane) as the lattice is only periodic in these directons. The prevalence of chain formation facilitates the dominance of linear $1\triangle(1,0)$ buckling. Figure 5.18 shows the phase diagram for dipolar soft spheres for $\mu^* = 1$.

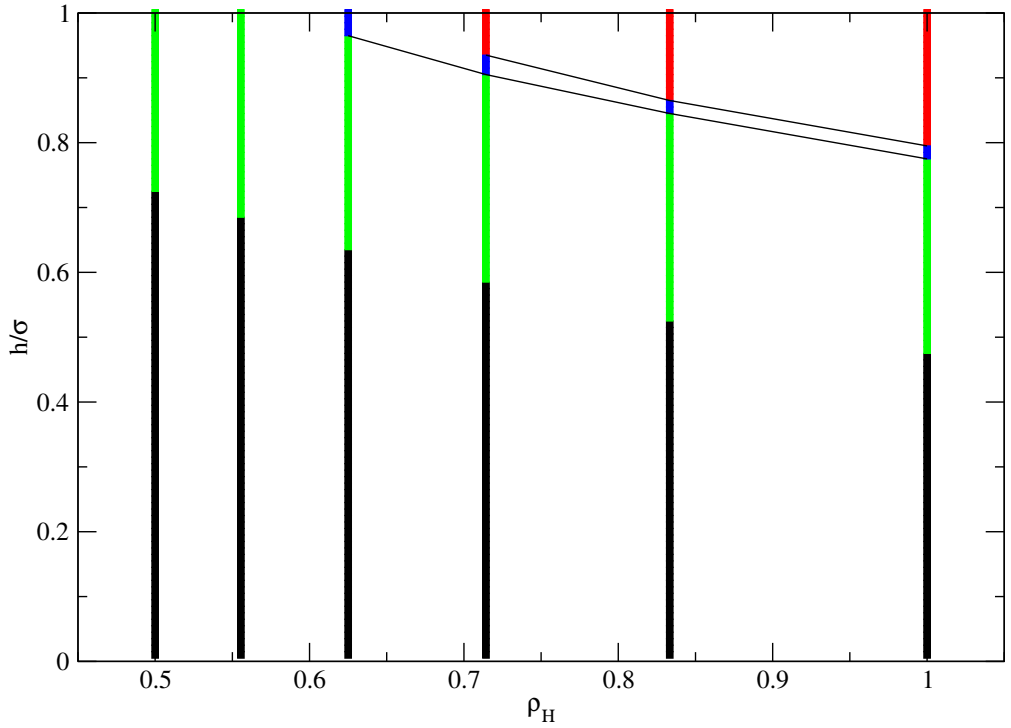

Figure 5.18.: Phase diagram of the dipolar soft sphere system in slab geometry. Square phase in green, triangular phase in red, intermediate phase in blue, and linear buckled phase in black. The black lines indicate the transitions. Note that a clear distinction between the $1\triangle(1,0)$ buckling and the $2\square$ (actually rectangular) phases is not possible.

At low densities and strong dipole moment (e.g. $\rho_{\mathrm{H}} = 0.5$ and $\mu^* = 2$) we found indications for phase separation at small slab width. In particular, the system no longer forms a crystal of uniform density, but instead forms regions of higher density with voids in between (see Fig. 5.19). This structure might be due to a characteristic optimum distance between parallel chains of dipoles [8, 18]. Oth-

erwise, the buckled $1\triangle(1,0)$ phase is formed for small slab thickness. This configuration smoothly transforms into a $2\square$ arrangement. Since the system never reaches perfect eight-fold symmetry, the distinction between those two phases is to some extent arbitrary. The $2\square$ phase is contracted in the direction of the aligned dipoles, forming thus a rectangular lattice.

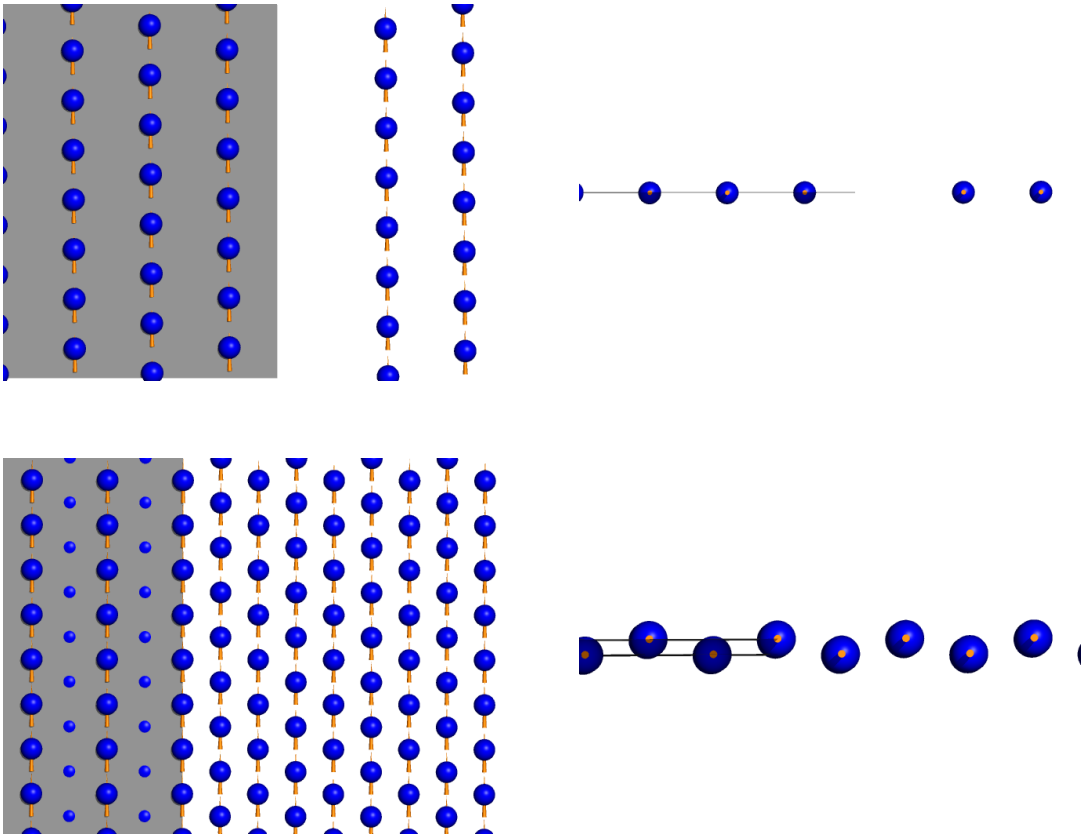

Figure 5.19.: Snapshots of the dipolar soft sphere system, showing the phase-separated (top) and the buckled $1\triangle(1,0)$ (bottom) phases. Top views on the left, side views on the right. The blue spheres are not drawn to scale. The grey areas represent planes parallel to the walls at a distance of $\sigma/2$. The orange cones represent the orientation of the dipoles.

The transition $1\triangle(1,0) = 2\square \rightarrow 2\triangle$ is marked by an intermediate phase I_1. This phase consists of a distorted $2\square$ lattice in which the dipoles are no longer oriented

so as to point at their nearest neighbors (see Fig. 5.20). After this intermediate phase, the 2△ phase becomes most favorable.

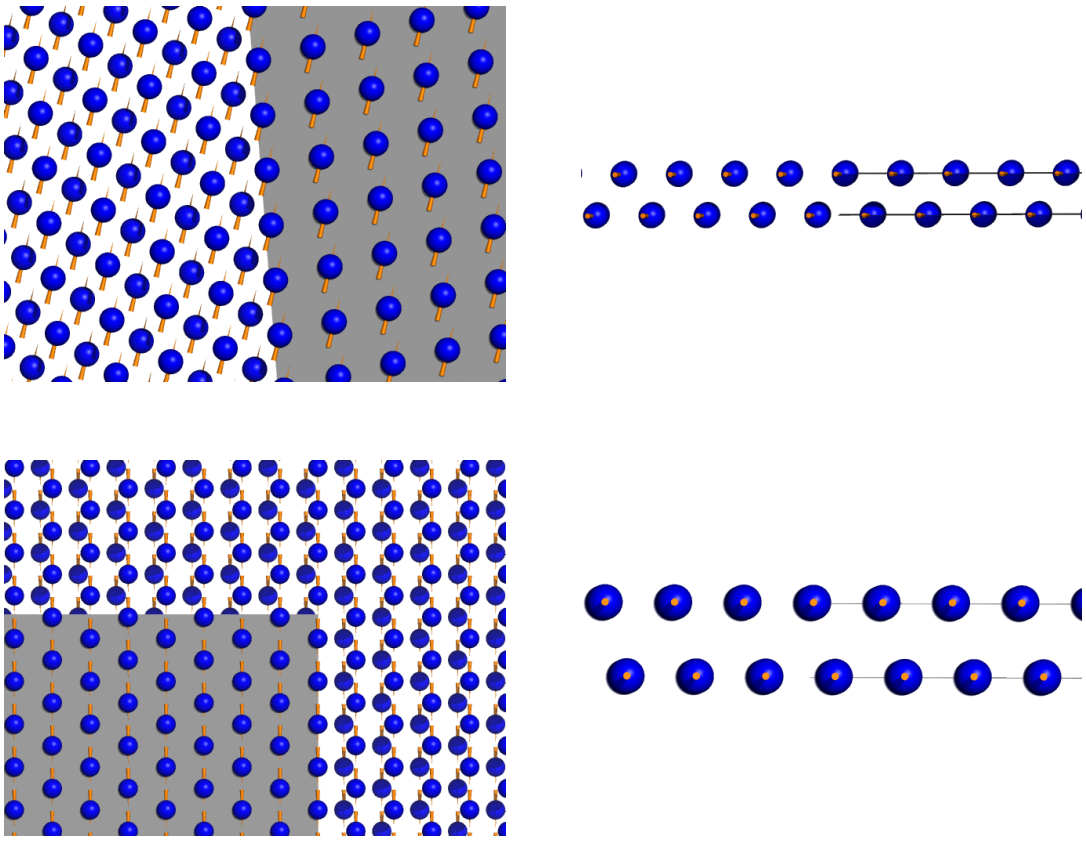

Figure 5.20.: Snapshots of the dipolar soft sphere system, showing the intermediate I_1 (top) and the 2△ (bottom) phases. Top views on the left, side views on the right. The blue spheres are not drawn to scale. The grey areas represent planes parallel to the walls at a distance of $\sigma/2$. The orange cones represent the orientation of the dipoles.

5.3. Effects of an External Field

Many experimental systems [13, 14, 94] are built up with dipoles oriented perpendicular to the walls. In most cases this stems from the fact that the dipolar particles are paramagnetic spheres that are magnetized with a field perpendicular

to the walls. As discussed in section 5.2, without such a field the dipoles orient in-plane. We have thus employed an external field E_{ext} perpendicular to the walls (as described in section 1.2). For the computations, we chose field strengths $E^*_{\text{ext}} = 15$ and $E^*_{\text{ext}} = 30$. For these values, the field term is approximately of the same magnitude as the dipole-dipole contribution or far above it, respectively. We have also implemented an option in the program that allows to keep the dipole moments completely fixed perpendicular to the walls. However, this leads to some inconsistencies in the computations when the dipole strength is varied. In this case articles are forced into a certain orientation, but do not minimize their energy in this orientation. Thus systems with stronger dipole moments lie energetically higher than systems with weak dipole moments, which does not correspond to the physical case and makes comparisons between them difficult. It should be noted that, in contrast to the monolayer system, dipoles oriented perpendicular to the wall do not simply interact with a r^{-3}-potential as there is a small attractive contribution from their difference in elevation z.

Figure 5.21 shows the energy and order parameter curves for systems with $\rho_{\text{H}} = 1$ and different values for μ^* and E^*_{ext}. The external field gives rise to a new family of intermediate, i.e. more complicated buckling, phases. Depending on density, the general sequence of phases is $1\triangle(1,0) \rightarrow 1\triangle(1,1) \rightarrow 1\triangle(3,1), 1\triangle(2,2) \rightarrow 2\square \rightarrow I_1 \rightarrow 2\triangle$. The exact transition from one to two layers is, once more, highly complicated. In particular, we have found indications that a cascade of different buckling phases might be present. Figures 5.23 to 5.25 show snapshots of the different phases for increasing slab width h. Figure 5.22 shows the phase diagrams for dipolar soft spheres with $\mu^* = 1$ for both $E^*_{\text{ext}} = 15$ and $E^*_{\text{ext}} = 30$.

For small slab widths, the $1\triangle(1,0)$ linear buckling phase (see Fig. 5.23) is observed for certain densities and fields. For higher densities, this phase is entirely suppressed. In the $1\triangle(1,0)$ phase, the dipoles are tilted in such a way that their in-plane components point at their nearest neighbor in the chain, thus all dipoles are parallel. The nearest neighbor distances along these chains are slightly contracted. The external field facilitates the formation of a new buckling phase. The buckling in the $1\triangle(1,1)$ phase is no longer linear, but occurs in a zig-zag pattern. Remarkable in this case is the orientation of the dipoles. These are no longer entirely parallel (see Fig. 5.23), but are tilted perpendicular to the creases. Close to

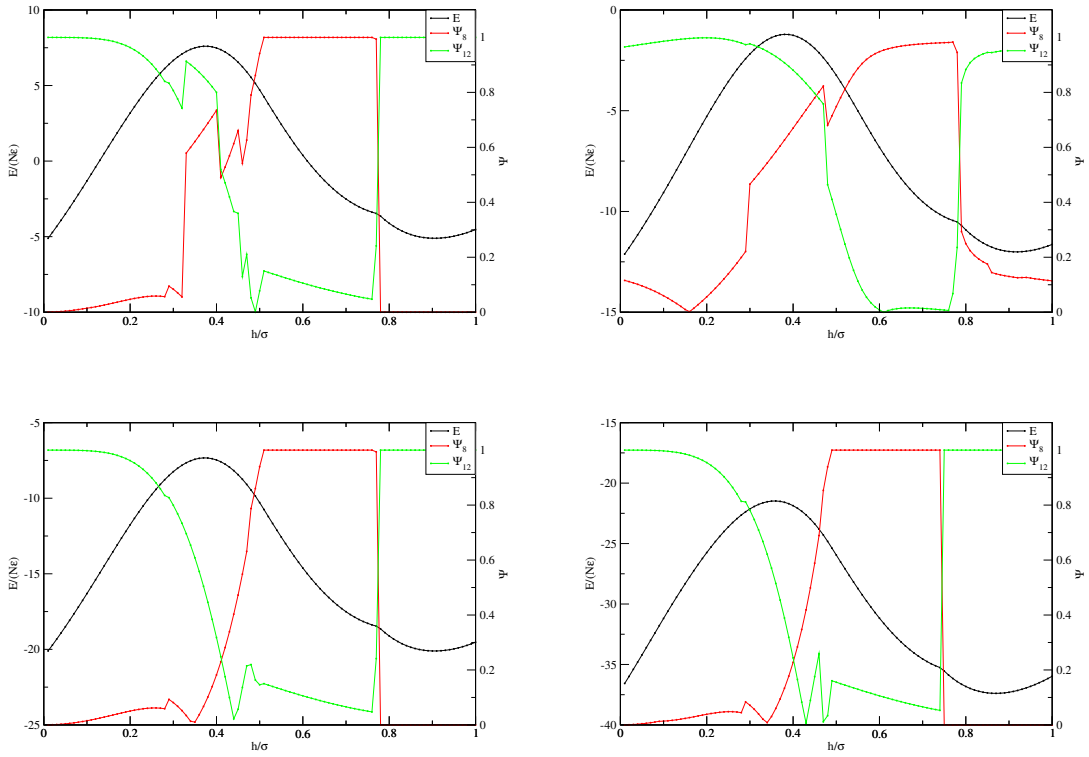

Figure 5.21.: Order parameters in a dipolar soft sphere system with external field. Top left: $\mu^* = 1$, $E^*_{\text{ext}} = 15$. Top right: $\mu^* = 2$, $E^*_{\text{ext}} = 15$. Bottom left: $\mu^* = 1$, $E^*_{\text{ext}} = 30$. Bottom right: $\mu^* = 2$, $E^*_{\text{ext}} = 30$.

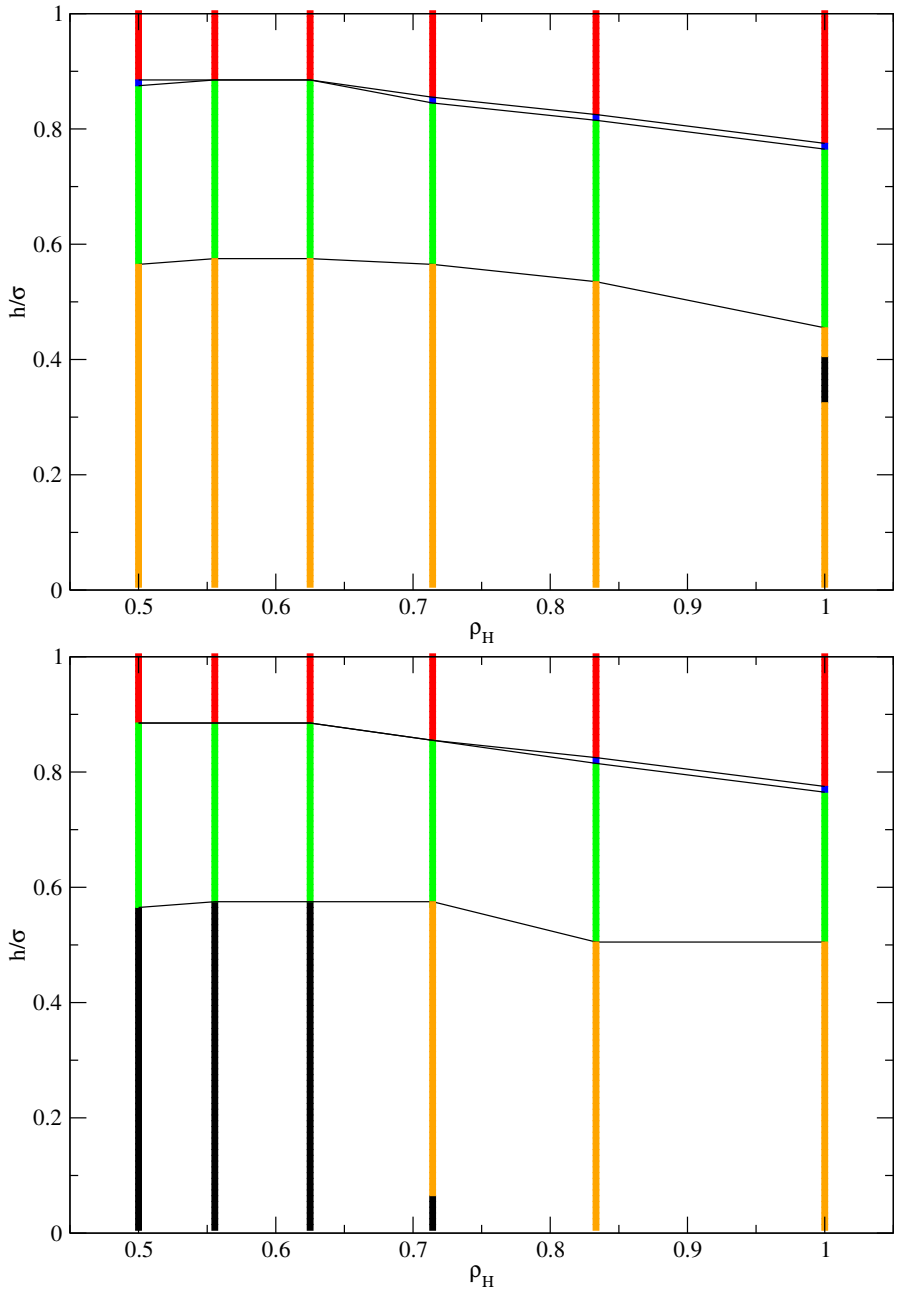

Figure 5.22.: Phase diagram of the dipolar soft sphere system in slab geometry under the influence of an external field. Square phase in green, triangular phase in red, intermediate phase in blue, linear buckled phase in black, and zig-zag buckled phase in orange. The black lines indicate the transitions. Top: $E^*_{\text{ext}} = 15$. Bottom: $E^*_{\text{ext}} = 30$.

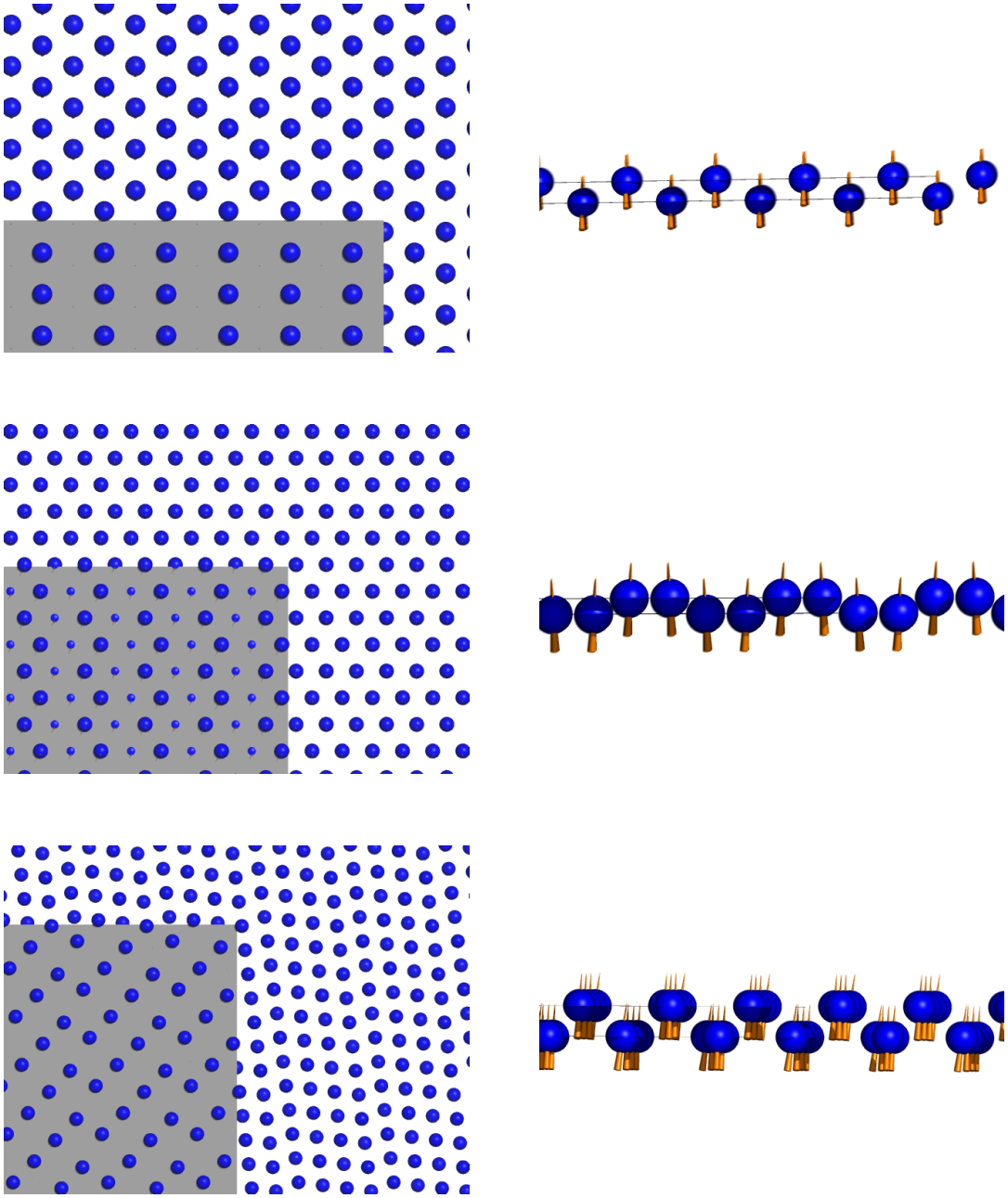

Figure 5.23.: Snapshots of the dipolar soft sphere system with external field, showing the $1\triangle(1,0)$ (top), the $1\triangle(1,1)$ (center) and the $1\triangle(3,1)$ (bottom) phases. Top views on the left, side views on the right. The blue spheres are not drawn to scale. The grey areas represent planes parallel to the walls at a distance of $\sigma/2$. The orange cones represent the orientation of the dipoles.

the one to two layer transition, more complicated buckling phases occur. During our optimizations, we found a $1\triangle(3,1)$ buckling phase. Such a phase is very similar to a $2\square$ configuration (see Fig. 5.23). Similar to the soft sphere case, where the transition from two to three layers might comprise a cascade of increasingly more complicated structures, higher order buckling phases might be present here. The region where they represent the dominant structures is very narrow. The dipoles in the $1\triangle(3,1)$ structure are tilted towards their neighbor in the chains. The last dipole before a kink, however, differs from this, as its environment is different (see Fig. 5.23).

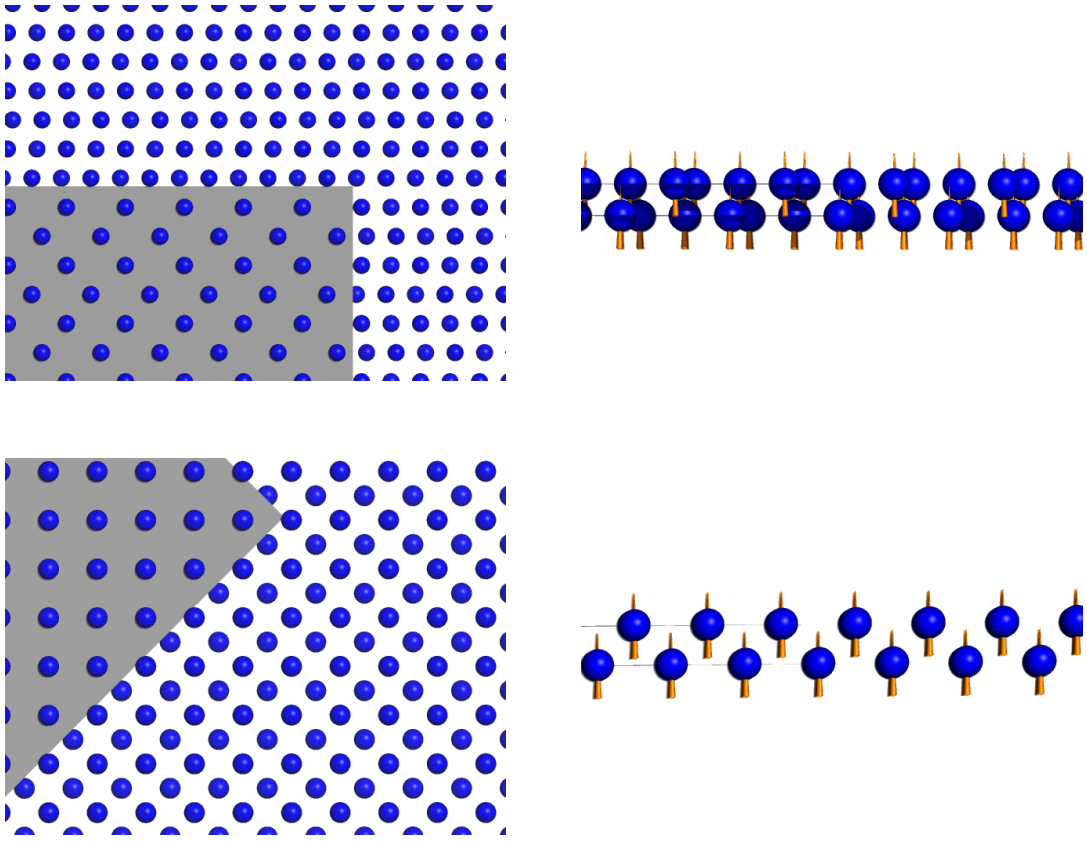

Figure 5.24.: Snapshots of the dipolar soft sphere system with external field, showing the $1\triangle(2,2)$ (top) and the $2\square$ (bottom) phases. Top views on the left, side views on the right. The blue spheres are not drawn to scale. The grey areas represent planes parallel to the walls at a distance of $\sigma/2$. The orange cones represent the orientation of the dipoles.

For some field strengths and densities, we have also observed a $1\triangle(2,2)$ buckling phase (see Fig. 5.24). Such a phase can be very close to a $2\square$ configuration, i.e. it is distorted strongly from the triangular lattice it is based on.

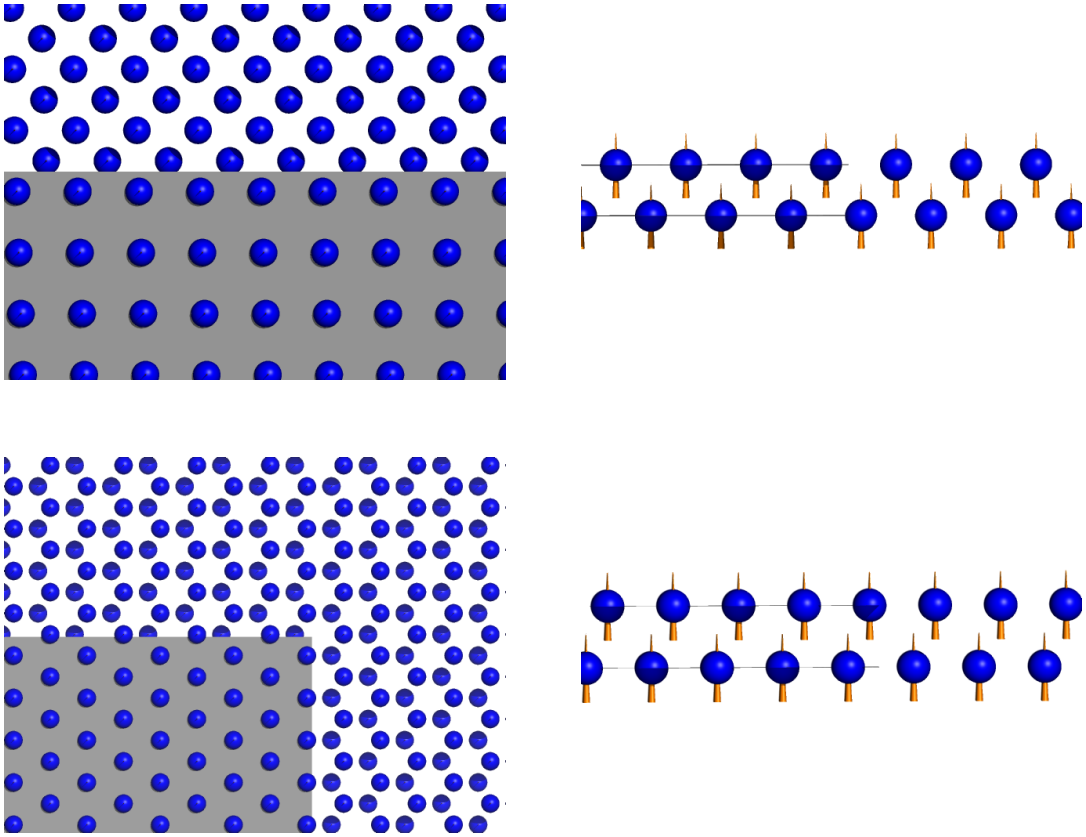

Figure 5.25.: Snapshots of the dipolar soft sphere system with external field, showing the intermediate I_1 (top) and the $2\triangle$ (bottom) phases. Top views on the left, side views on the right. The blue spheres are not drawn to scale. The grey areas represent planes parallel to the walls at a distance of $\sigma/2$. The orange cones represent the orientation of the dipoles.

The transition $2\square \rightarrow 2\triangle$ is effected by the intermediate I_1 phase (see Fig. 5.25), which is a distorted version of the square phase.

6. Summary and Outlook

In this work, we have studied the energetically most favorable configurations of confined (quasi-2D) systems of dipolar soft spheres at zero temperatures. This was achieved by minimizing the relevant thermodynamic potential using an optimization tool based on ideas of genetic algorithms.

For soft spheres, we have found that the general sequence of stable phases is the same as for a hard sphere systems. We have observed many different intermediate phases that exhibit a complicated inherent 3D structure. Closer investigations, particularly at the transition from two to three layers would be of high interest. Monte Carlo simulations at finite temperature in the interesting regions would be necessary to determine the thermodynamical stability of the structures we observed.

For dipolar soft spheres, we have observed that dipoles orient parallel to the walls. Thus, we did not observe fundamental differences depending on the dipole moment.

We also studied the effects of an external field perpendicular to the walls on a confined system of dipolar soft spheres. Depending on field strength, density and slab thickness, we have observed several different buckling phases that become increasingly complicated close to the transition from one to two layers. These are similar to buckling phases observed in some experimental systems. More detailed investigations of the dependence on density and field strength would be necessary to better understand the phase diagram.

In general, our optimization strategy is appropriate for higher densities, but investigations at low densities are more difficult as energy differences can be very small. Appropriate modifications to the genetic algorithm optimization tool might be able to alleviate this problem.

Further development on the order parameters we used to analyze our results would be necessary to correctly classify systems ranging from 2D to 3D. Such order parameters might make it easier to understand the transition from a monolayer to the bulk.

Other interesting systems that could be investigated with our program include binary mixtures of dipolar soft spheres [60] (functionality for this is already included in the program) or systems of dipolar ellipsoidal particles [95].

7. Acknowledgments

I would like to thank all the people who have helped and supported me while writing this thesis:

First of all my advisor, Gerhard Kahl, who has given me lots of advice and has made so many things possible.

Another many thanks go to Günther Doppelbauer for helping me with all of the technical aspects, from writing the code to visualization and more, and for solving so many of my problems.

I would also like to thank Martial Mazars for advising and helping me during my stay in France and for all the suggestions and advice.

Further thanks goes to Jean-Jacques Weis and the people at the Laboratoire de Physique Théorique at the Université Paris-Sud in Orsay, and to the people of the *HPC-Europa2* program, particularly at CINES in Montpellier, for an interesting and productive time in France. I would also like to acknowledge financial support by the Technische Universität Wien's *Programm für kurzfristige wissenschaftliche Aufenthalte im Ausland*.

To the people of the Soft Matter Theory Group at Technische Universität Wien, Emanuela Bianchi, Giannis Georgiou, Ismene Kolovos, Jan Kurzidim, Martina Lechner, Marta Montes-Saralegui, Arash Nikoubashman, Ulf Pedersen, Dieter Schwanzer, Panagiotis Theodorakis and Andreas Tröster, I am very grateful for the many enjoyable lunches and the positive environment.

Last but not least I would like to thank my family for supporting me during my studies (and trying to understand what exactly I was doing) and my friends in Vienna and Linz for all the fun and welcome distractions during the years.

Bibliography

[1] S. Odenbach, editor. *Ferrofluids, Magnetically Controlable Fluids and Their Applications*. Lecture Notes Physics. Springer, New York, 2002.

[2] A. P. Philipse and D. Maas. Magnetic colloids from magnetotactic bacteria: chain formation and colloidal stability. *Langmuir*, 18:9977–9984, 2002.

[3] B. Groh and S. Dietrich. Density-functional theory for the freezing of stockmayer fluids. *Physical Review E*, 54:1687, 1996.

[4] S. Klapp and F. Forstmann. Stability of ferroelectric fluid and solid phases in the stockmayer model. *Europhysics Letters*, 38:663, 1997.

[5] S. Klapp and F. Forstmann. Crystallization of dipolar hard spheres: Density functional results. *Journal of Chemical Physics*, 109:1062, 1998.

[6] S. Klapp and G. Patey. Integral equation theory for dipolar hard sphere fluids with fluctuating orientational order. *Journal of Chemical Physics*, 112:3832, 2000.

[7] G. T. Gao and X. C. Zeng. Freezing transition of a strongly dipolar simple fluid. *Physical Review E*, 61:R2188, 2000.

[8] B. Groh and S. Dietrich. Crystal structures and freezing of dipolar fluids. *Physical Review E*, 63:021203, 2001.

[9] J. Richardi, M. P. Pileni, and J.-J. Weis. Self-organization of confined dipolar particles in a parallel field. *Journal of Chemical Physics*, 130:124515, 2009.

[10] J. Richardi and J.-J. Weis. Low density mesostructures of confined dipolar particles in an external field. *Journal of Chemical Physics*, 135:124502, 2011.

[11] F. Ramiro-Manzano, E. Bonet, I. Rodriguez, and F. Meseguer. Layering transitions in confined colloidal crystals: The hcp-like phase. *Physical Review E*, 76:050401, 2007.

[12] F. Ramiro-Manzano, Elvira Bonet, Isabelle Rodriguez, and Francisco Meseguer. Layering transitions in colloidal crystal thin films between 1 and 4 monolayers. *Soft Matter*, 5:4279–4282, 2009.

[13] Florian Ebert, Patrick Dillmann, Georg Maret, and Peter Keim. The experimental realization of a two-dimensional colloidal model system. *Review of Scientific Instruments*, 80:083902, 2009.

[14] Lahcen Assoud, Florian Ebert, Peter Keim, René Messina, Georg Maret, and Hartmut Löwen. Ultrafast quenching of binary colloidal suspensions in an external magnetic field. *Physical Review Letters*, 102(23):238301, 2009.

[15] Olivier Cayre, Vesselin N. Paunov, and Orlin D. Velev. Fabrication of dipolar colloid particles by microcontact printing. *Chemical Communications*, pages 2296–2297, 2003.

[16] K. Butter, P. H. H. Bomans, P. M. Frederik, G. J. Vroege, and A. P. Philipse. Direct observation of dipolar chains in iron ferrofluids by cryogenic electron microscopy. *Nature Materials*, 2:88–91, 2003.

[17] Mark Klokkenburg, Ben H. Erné, Johannes D. Meeldijk, and Albrecht Wiedenmann. *In Situ* imaging of field-induced hexagonal columns in magnetite ferrofluids. *Physical Review Letters*, 97:185702, 2006.

[18] R. Tao and J. M. Sun. Three-dimensional structure of induced electrorheological solid. *Physical Review Letters*, 67(3):398–401, 1991.

[19] Bernd Hartke. Global cluster geometry optimization by a phenotype algorithm with niches: Location of elusive minima, and low-order scaling with cluster size. *Journal of Computational Chemistry*, 20:1752, 1999.

[20] J. A. Barker and R. O. Watts. Monte carlo studies of the dielectric properties of water-like models. *Molecular Physics*, 26(3):789–792, 1973.

[21] B. R. A. Nijboer and F. W. de Wette. On the calculation of lattice sums. *Physica XXIII*, 1957.

[22] B. R. A. Nijboer. On the electrostatic potential due to a slab shaped and a semi-infinite nacl-type lattice. *Physica A*, 125:275, 1984.

[23] John Lekner. Summation of dipolar fields in simulated liquid-vapour interfaces. *Physica A*, 157(2):826–838, 1989.

[24] John Lekner. Summation of coulomb fields in computer-simulated disordered systems. *Physica A*, 176(3):485–498, 1991.

[25] J. M. Caillol. Structural, thermodynamic, and electrical properties of polar fluids and ionic solutions on a hypersphere: Theoretical aspects. *Journal of Chemical Physics*, 96(2):1455, 1992.

[26] V. Rokhlin. Rapid solution of integral equations of classical potential theory. *Journal of Computational Physics*, 60(2):187–207, 1995.

[27] L. Greengard and V. Rokhlin. A fast algorithm for particle simulations. *Journal of Computational Physics*, 135:280–292, 1997.

[28] K. E. Schmidt and M. A. Lee. Implementing the fast multipole method in three dimensions. *Journal of Statistical Physics*, 63:1223–1235, 1991.

[29] P. P. Ewald. Die berechnung optischer und elektrostatischer gitterpotentiale. *Annalen der Physik*, 64:253, 1921.

[30] M. P. Tosi. *Cohesion of ionic solids in the Born model*. Academic Press, New York, 1964.

[31] S. W. de Leeuw, J. W. Perram, and E. R. Smith. Simulation of electrostatic systems in periodic boundary conditions. i. lattice sums and dielectric constants. *Proceedings of the Royal Society of London A*, 373:27–56, 1980.

[32] T. M. Nymand and P. Linse. Ewald summation and reaction field methods for potentials with atomic charges, dipoles, and polarizabilities. *Journal of Chemical Physics*, 112:6152, 2000.

[33] Martial Mazars. Ewald methods for inverse power-law interactions in tridimensional and quasi two-dimensional systems. *Journal of Physics A: Mathematical and Theoretical*, 43:425002, 2010.

[34] Martial Mazars. Long ranged interactions in computer simulations and for quasi-2d systems. *Physics Reports*, 500:43–116, 2011.

[35] D. Frenkel and N. Smit. *Understanding molecular simulation*. Academic Press, 1996.

[36] M. P. Allen and D. J. Tildesley. *Computer Simulation of Liquids*. Oxford University Press, 1987.

[37] In-Chul Yeh and Max L. Berkowitz. Ewald summation for systems with slab geometry. *Journal of Chemical Physics*, 111:3155, 1999.

[38] M. Mazars, J.-M. Caillol, J.-J. Weis, and D. Levesque. Comparison of simulation methods for charged systems of slab geometry. *Condensed Matter Physics*, 4(4):697–713, 2001.

[39] S. H. L. Klapp and M. Schoen. Spontaneous orientational order in confined dipolar fluid systems. *Journal of Chemical Physics*, 117:8050, 2002.

[40] Sabine H. L. Klapp. Monte-carlo simulations of strongly interacting dipolar fluids between two conducting walls. *Molecular Simulation*, 32(8):609–621, 2006.

[41] M. Schoen and S. H. L. Klapp. *Reviews in Computational Chemistry*, volume 24. Wiley-VCH, New Jersey, 2007.

[42] Jelena Jordanovic and Sabine H. L. Klapp. Structure of ferrofluid nanofilms in homogeneous magnetic fields. *Physical Review E*, 79:021405, 2009.

[43] Charles Darwin. *The Origin of Species by Means of Natural Selection*. John Murray, London, 1859.

[44] Nils Aall Barricelli. Esempi numerici di processi di evoluzione. *Methodos*, pages 45–68, 1954.

[45] Nils Aall Barricelli. Symbiogenetic evolution processes realized by artificial methods. *Methodos*, pages 143–182, 1957.

[46] Alex Fraser. Simulation of genetic systems by automatic digital computers. i. introduction. *Australian Journal of Biological Sciences*, 10:484–491, 1957.

[47] Alex Fraser and Donald Burnell. *Computer Models in Genetics*. McGraw-Hill, New York, 1970.

[48] Jack L. Crosby. *Computer Simulation in Genetics*. John Wiley & Sons, London, 1973.

[49] J. H. Holland. *Adaptation in Natural and Artificial Systems*. The University of Michigan Press, Ann Arbor, 1975.

[50] S. Sato, K. Otori, A. Takizawa, H. Sakai, Y. Ando, and H. Kawamura. Applying genetic algorithms to the optimum design of a concert hall. *Journal of Sound and Vibration*, 258(3):517–526, 2002.

[51] Shigeru Obayashi, Daisuke Sasaki, Yukihiro Takeguchi, and Naoki Hirose. Multiobjective evolutionary computation for supersonic wing-shape optimization. *IEEE Transactions on Evolutionary Computation*, 4(2):182–187, 2000.

[52] A. Assion, T. Baumert, M. Bergt, T. Brixner, B. Kiefer, V. Seyfried, M. Strehle, and G. Gerber. Control of chemical reactions by feedback-optimized phase-shaped femtosecond laser pulses. *Science*, 282:919–922, 1998.

[53] Edward Altshuler and Derek Linden. Design of a wire antenna using a genetic algorithm. *Journal of Electronic Defense*, 20(7):50–52, 1997.

[54] R. Giro, M. Cyrillo, and D. S. Galvao. Designing conducting polymers using genetic algorithms. *Chemical Physics Letters*, 366(1-2):170–175, 2002.

[55] D. Gottwald, G. Kahl, and C. N. Likos. Prediciting equilibrium structures in freezing processes. *Journal of Chemical Physics*, 122:204503, 2005.

[56] G. J. Pauschenwein and G. Kahl. Clusters, columns, and lamellae - minimum energy configurations in core softened potentials. *Soft Matter*, 4:1396, 2008.

[57] G. J. Pauschenwein and G. Kahl. Zero temperature phase diagram of the square-shoulder system. *Journal of Chemical Physics*, 129:174107, 2008.

[58] J. Fornleitner, F. Lo Verso, G. Kahl, and C. N. Likos. Genetic algorithms predict formation of exotic ordered configurations for two-component dipolar monolayers. *Soft Matter*, 4:480, 2008.

[59] J. Fornleitner and G. Kahl. Lane formation vs. cluster formation in two-dimensional square-shoulder systems - a genetic algorithm approach. *Europhysics Letters*, 82:18001, 2008.

[60] Julia Fornleitner, Federica Lo Verso, Gerhard Kahl, and Christos N. Likos. Ordering in two-dimensional dipolar mixtures. *Langmuir*, 25(14):7836–7846, 2009.

[61] G. Doppelbauer, E. Bianchi, and G. Kahl. Self-assembly scenarios of patchy colloidal particles in two dimensions. *Journal of Physics: Condensed Matter*, 22(10):104105, 2010.

[62] Moritz Antlanger, Günther Doppelbauer, and Gerhard Kahl. On the stability of archimedean tilings formed by patchy particles. *Journal of Physics: Condensed Matter*, 23:404206, 2011.

[63] Mario Kahn. Ordered equilibrium structures of soft particles. Master's thesis, Technische Universität Wien, 2008.

[64] Mario Kahn, Jean-Jacques Weis, and Gerhard Kahl. Ordered equilibrium structures of soft particles in thin layers. *Journal of Chemical Physics*, 133:224504, 2010.

[65] Dieter Gottwald. *Genetic Algorithms in Condensed Matter Theory.* PhD thesis, Technische Universität Wien, 2005.

[66] Julia Fornleitner. *Ordered Equilibrium Structures of Two-Dimensional Soft Matter Systems.* PhD thesis, Technische Universität Wien, 2008.

[67] Gernot J. Pauschenwein. *Phase Behaviour of Colloidal Systems.* PhD thesis, Technische Universität Wien, 2008.

[68] Günther Doppelbauer. Development of a phenotype algorithm for particle geometry optimization. Master's thesis, Technische Universität Wien, 2009.

[69] Günther Doppelbauer. *Ordered Structures of Patchy Particle Systems.* PhD thesis, Technische Universität Wien, 2012.

[70] Camille Jouvie. Ordered equilibrium structures for dipolar fluids. Master's thesis, Technische Universität Wien, 2010.

[71] Sphere point picking. http://mathworld.wolfram.com/SpherePointPicking.html.

[72] C. W. Glass, A. R. Oganov, and N. Hansen. Uspex - evolutionary crystal structure prediction. *Computational Physics Communications*, 175:713, 2006.

[73] N. L. Abraham. *A Genetic Algorithm for Crystal Structure Prediction*. PhD thesis, University of York, 2007.

[74] N. L. Abraham. Improved real-space genetic algorithm for crystal structure and polymorph prediction. *Physical Review B*, 77:134117, 2008.

[75] D. C. Lonie and E. Zurek. Xtalopt: An open-source evolutionary algorithm for crystal structure prediction. *Computational Physics Communications*, 182:372, 2011.

[76] D. C. Lonie and E. Zurek. Identifying duplicate crystal structures: Xtalcomp, an open-source solution. *Computational Physics Communications*, 183:690, 2012.

[77] D. J. Wales and J. P. K. Doye. Global optimization by basin-hopping and the lowest energy of lennard-jones clusters containing up to 110 atoms. *Journal of Physical Chemistry A*, 101:5111, 1997.

[78] C. Zhu, R. H. Byrd, P. Lu, and J. Nocedal. L-bfgs-b: a limited memory fortran code for solving bound constrained optimization problems. Technical report, NAM-11, EECS Department, Northwestern University, 1994.

[79] R. H. Byrd, P. Lu, J. Nocedal, and C. Zhu. A limited memory algorithm for bound constrained optimization. *SIAM Journal of Scientific Computing*, 16:1190–1208, 1995.

[80] Open mpi: Open source high performance computing. http://www.open-mpi.org/.

[81] Intel fortran compiler. http://software.intel.com/en-us/articles/intel-compilers/.

[82] Katherine J. Strandburg, John A. Zollweg, and G. V. Chester. Bond-angular

order in two-dimensional lennard-jones and hard-disk systems. *Physical Review B*, 30(5):2755, 1984.

[83] Katherine J. Strandburg. Two-dimensional melting. *Review of Modern Physics*, 60:161, 1988.

[84] Paul J. Steinhardt, David R. Nelson, and Marco Ronchetti. Bond-orientational order in liquids and glasses. *Physical Review B*, 28(2):784–805, 1983.

[85] Wolfgang Lechner and Christoph Dellago. Accurate determination of crystal structures based on averaged local bond order parameters. *Soft Matter*, 5:646, 2008.

[86] Harold T. Stokes and Dorian M. Hatch. Findsym: program for identifying the space-group symmetry of a crystal. *Journal of Applied Crystallography*, 38:237–238, 2005.

[87] Pymol molecular viewer. `http://www.pymol.org/`.

[88] Xmgrace. `http://plasma-gate.weizmann.ac.il/Grace/`.

[89] Pawel Pieranski, L. Strzelecki, and B. Pansu. Thin colloidal crystals. *Physical Review Letters*, 50(12):900–903, 1983.

[90] Matthias Schmidt and Hartmut Löwen. Phase diagram of hard spheres confined between two parallel plates. *Physical Review E*, 55(6):7228–7241, 1997.

[91] Andrea Fortini and Marjolein Dijkstra. Phase behaviour of hard spheres confined between parallel hard plates: manipulation of colloidal crystal structures by confinement. *Journal of Physics: Condensed Matter*, 18:L371–L378, 2006.

[92] I. Rodríguez, F. Ramiro-Manzano, F. Meseguer, and E. Bonet. Fabrication and characterization of colloidal crystal thin films. *European Journal of Physics*, 32:505–515, 2011.

[93] Yilong Han, Yair Shokef, Ahmed M. Alsayed, Peter Yunker, Tom C. Lubensky, and Arjun G. Yodh. Geometric frustration in buckled colloidal monolayers. *Nature*, 456:898–903, 2008.

[94] Norman Hoffmann, Florian Ebert, Christos N. Likos, Hartmut Löwen, and

Georg Maret. Partial clustering in binary two-dimensional colloidal suspensions. *Physical Review Letters*, 97(7):078301, 2006.

[95] Arash Nikoubashman and Christos N. Likos. Self-assembled structures of gaussian nematic particles. *Journal of Physics: Condensed Matter*, 22:104107, 2010.

[96] C. G. Broyden. The convergence of a class of double-rank minimization algorithms 1. general considerations. *IMA Journal of Applied Mathematics*, 6(1):76–90, 1970.

[97] R. Fletcher. A new approach to variable metric algorithms. *The Computer Journal*, 13(3):317–322, 1970.

[98] G. F. Voronoi. Nouvelles applications des paramètres continus à la théorie de formes quadratiques. *Journal für die reine und angewandte Mathematik*, 134:198–287, 1908.

A. Appendix

A.1. Lattice Reduction

In some cases, it can be useful to use a lattice vector representation that contains more parameters than the minimal set. For example when simplifying the lattice, permanently enforcing that the vector $\mathbf{a}$ points in x-direction restricts the choice of possible alternative lattice vectors we can consider. However, when simplifying the lattice by using general lattice vectors, the resulting lattice vectors will no longer fulfill the conditions we specify. We thus have to transform the lattice back into the reduced form via a rotation [19]. As we show in the following, this can be achieved by determining the length of all lattice vectors and the angles between them. Then, we simply reconstruct the lattice vectors in the desired orientations using [19]

$$\mathbf{a} = \begin{pmatrix} |a| \\ 0 \\ 0 \end{pmatrix} \tag{A.1}$$

$$\mathbf{b} = \begin{pmatrix} |b| \cos\left(\widehat{\mathbf{ab}}\right) \\ |b| \sin\left(\widehat{\mathbf{ab}}\right) \\ 0 \end{pmatrix} \tag{A.2}$$

$$\mathbf{c} = \begin{pmatrix} |c| \cos\left(\widehat{\mathbf{ac}}\right) \\ |c| \frac{\cos\left(\widehat{\mathbf{bc}}\right) - \cos\left(\widehat{\mathbf{ac}}\right) \cos\left(\widehat{\mathbf{ab}}\right)}{\sin\left(\widehat{\mathbf{ab}}\right)} \\ |c| \frac{\sqrt{1 - \cos^2\left(\widehat{\mathbf{ab}}\right) - \cos^2\left(\widehat{\mathbf{ac}}\right) - \cos^2\left(\widehat{\mathbf{bc}}\right) + 2\cos\left(\widehat{\mathbf{ab}}\right)\cos\left(\widehat{\mathbf{ac}}\right)\cos\left(\widehat{\mathbf{bc}}\right)}}{\sin\left(\widehat{\mathbf{ab}}\right)} \end{pmatrix} \tag{A.3}$$

which leaves the fractional coordinates of the particles unchanged. The dipole orientations will, however, differ with respect to the old (unreduced) lattice; thus

we have to rotate them as well (see appendix A.2).

A.2. Dipole Reorientation

The dipole orientations are given by two angles θ and ψ measured with respect to the z-axis. In some cases (e.g. after straining the lattice or simplifying it) we need to transform the lattice to its reduced form (see section 1.3). This operation is equivalent to rotating the lattice in three dimensions, changing thereby also the z-axis. In order to preserve the orientation of the dipoles (i.e. they should still point in the same *lattice* directions as before), we have to recalculate θ and ψ. In the following, a tilde will be used to denote the orientations and lattice vectors of the old system. The orientation of a dipole in the old system is

$$\begin{aligned} \begin{pmatrix} \tilde{\mu_{\mathrm{x}}} \\ \tilde{\mu_{\mathrm{y}}} \\ \tilde{\mu_{\mathrm{z}}} \end{pmatrix} &= \mu \begin{pmatrix} \sin\tilde{\psi}\cos\tilde{\theta} \\ \sin\tilde{\psi}\sin\tilde{\theta} \\ \cos\tilde{\psi} \end{pmatrix} \\ &= \tilde{x}\tilde{\mathbf{a}} + \tilde{y}\tilde{\mathbf{b}} + \tilde{z}\tilde{\mathbf{c}} = \begin{pmatrix} \tilde{a_{\mathrm{x}}} & \tilde{b_{\mathrm{x}}} & \tilde{c_{\mathrm{x}}} \\ \tilde{a_{\mathrm{y}}} & \tilde{b_{\mathrm{y}}} & \tilde{c_{\mathrm{y}}} \\ \tilde{a_{\mathrm{z}}} & \tilde{b_{\mathrm{z}}} & \tilde{c_{\mathrm{z}}} \end{pmatrix} \cdot \begin{pmatrix} \tilde{x} \\ \tilde{y} \\ \tilde{z} \end{pmatrix} \end{aligned} \tag{A.4}$$

and the orientation in the new system (which shall *not* be the same orientation in absolute coordinates) is

$$\begin{pmatrix} \mu_{\mathrm{x}} \\ \mu_{\mathrm{y}} \\ \mu_{\mathrm{z}} \end{pmatrix} = \begin{pmatrix} a_{\mathrm{x}} & b_{\mathrm{x}} & c_{\mathrm{x}} \\ 0 & b_{\mathrm{y}} & c_{\mathrm{y}} \\ 0 & 0 & c_{\mathrm{z}} \end{pmatrix} \cdot \begin{pmatrix} x \\ y \\ z \end{pmatrix}. \tag{A.5}$$

As we want the orientation of the dipoles with respect to the *lattice* vectors to remain the same, we choose

$$\begin{pmatrix} x \\ y \\ z \end{pmatrix} = \begin{pmatrix} \tilde{x} \\ \tilde{y} \\ \tilde{z} \end{pmatrix}, \tag{A.6}$$

which leads to

$$\begin{pmatrix} \mu_\mathrm{x} \\ \mu_\mathrm{y} \\ \mu_\mathrm{z} \end{pmatrix} = \begin{pmatrix} a_\mathrm{x} & b_\mathrm{x} & c_\mathrm{x} \\ 0 & b_\mathrm{y} & c_\mathrm{y} \\ 0 & 0 & c_\mathrm{z} \end{pmatrix} \cdot \begin{pmatrix} \tilde{a_\mathrm{x}} & \tilde{b_\mathrm{x}} & \tilde{c_\mathrm{x}} \\ \tilde{a_\mathrm{y}} & \tilde{b_\mathrm{y}} & \tilde{c_\mathrm{y}} \\ \tilde{a_\mathrm{z}} & \tilde{b_\mathrm{z}} & \tilde{c_\mathrm{z}} \end{pmatrix}^{-1} \cdot \begin{pmatrix} \tilde{\mu_\mathrm{x}} \\ \tilde{\mu_\mathrm{y}} \\ \tilde{\mu_\mathrm{z}} \end{pmatrix} \tag{A.7}$$

This transformation leaves the length of $\boldsymbol{\mu}$ unchanged as the volume (i.e. the determinant of the matrices in equ. A.4 and A.5) is the same for both bases. Finally, we can extract the new orientation angles θ and ψ using

$$\psi = \arccos\left(\frac{\mu_\mathrm{z}}{\mu}\right) \tag{A.8}$$

$$\theta = \arctan\left(\frac{\mu_\mathrm{y}}{\mu_\mathrm{x}}\right). \tag{A.9}$$

A.3. L-BFGS Algorithm

The *Limited Memory Broyden-Fletcher-Goldfarb-Shanno* (L-BFGS) algorithm belongs to the family of quasi-Newton optimization methods to minimize functions $f(\boldsymbol{x})$, where $\boldsymbol{x}$ can be a vector in a high-dimensional space. While the original BFGS algorithm [96, 97] explicitly calculates an approximated Hessian matrix $H(f)_\mathrm{ij}(\boldsymbol{x}) = D_\mathrm{i}D_\mathrm{j}f(\boldsymbol{x})$, only a few previous steps are stored in this case, which makes this method suitable for high-dimensional local optimizations.

Starting from a parameter point $\boldsymbol{x}_0$, the algorithm updates to

$$\boldsymbol{x}_{\mathrm{k}+1} = \lambda_\mathrm{k}\boldsymbol{d}_\mathrm{k} \tag{A.10}$$

where λ_k is determined as an appropriate step size in a line search along the descent direction $\boldsymbol{d}_\mathrm{k}$. The approximation to the Hessian has to satisfy

$$H_{\mathrm{k}+1}\boldsymbol{y}_\mathrm{k} = \alpha_\mathrm{k}\boldsymbol{s}_\mathrm{k} \tag{A.11}$$

$$\alpha_\mathrm{k} > 0. \tag{A.12}$$

In the regular BFGS algorithm, the Hessian is updated according to

$$H_{\mathrm{k}+1} = H_\mathrm{k} + \frac{1}{\boldsymbol{s}_\mathrm{k}^\mathrm{T}\boldsymbol{y}_\mathrm{k}}\left[\left(1 + \frac{\boldsymbol{y}_\mathrm{k}^\mathrm{T}H_\mathrm{k}\boldsymbol{y}_\mathrm{k}}{\boldsymbol{s}_\mathrm{k}^\mathrm{T}\boldsymbol{y}_\mathrm{k}}\right)\boldsymbol{s}_\mathrm{k}\boldsymbol{s}_\mathrm{k}^\mathrm{T} - \boldsymbol{s}_\mathrm{k}\boldsymbol{y}_\mathrm{k}^\mathrm{T}H_\mathrm{k} - H_\mathrm{k}\boldsymbol{y}_\mathrm{k}\boldsymbol{s}_\mathrm{k}^\mathrm{T}\right] \tag{A.13}$$

$$V_{\mathrm{k}} = 1 - \rho_{\mathrm{k}} \boldsymbol{y}_{\mathrm{k}} \boldsymbol{s}_{\mathrm{k}}^{\mathrm{T}} \tag{A.14}$$

$$\boldsymbol{s}_{\mathrm{k}} = \boldsymbol{x}_{\mathrm{k}+1} - \boldsymbol{x}_{\mathrm{k}} \tag{A.15}$$

$$\boldsymbol{y}_{\mathrm{k}} = \boldsymbol{g}_{\mathrm{k}+1} - \boldsymbol{g}_{\mathrm{k}} \tag{A.16}$$

$$\boldsymbol{g}_{\mathrm{k}} = \nabla f(\boldsymbol{x}_{\mathrm{k}}) \tag{A.17}$$

$$\boldsymbol{d}_{\mathrm{k}} = -H_{\mathrm{k}} \boldsymbol{g}_{\mathrm{k}}. \tag{A.18}$$

The L-BFGS algorithm follows the same procedure for the first m steps, but afterwards just applies m quasi-Newton updates to H_0 using the saved last m steps

$$H_{\mathrm{k}+1} = V_{\mathrm{k}}^{\mathrm{T}} H_{\mathrm{k}} V_{\mathrm{k}} + \rho_{\mathrm{k}} \boldsymbol{s}_{\mathrm{k}} \boldsymbol{s}_{\mathrm{k}}^{\mathrm{T}} \tag{A.19}$$

$$\rho_{\mathrm{k}} = \frac{1}{\boldsymbol{y}_{\mathrm{k}}^{\mathrm{T}} \boldsymbol{s}_{\mathrm{k}}} \tag{A.20}$$

$$V_{\mathrm{k}} = 1 - \rho_{\mathrm{k}} \boldsymbol{y}_{\mathrm{k}} \boldsymbol{s}_{\mathrm{k}}^{\mathrm{T}}. \tag{A.21}$$

A.4. Lattice Simplification

In order to simplify the unit cell, we try different combinations of the lattice vectors

$$\mathbf{a} \rightarrow \begin{cases} \mathbf{a} \pm \mathbf{b} \\ \mathbf{a} \pm \mathbf{c} \end{cases} . \tag{A.22}$$

This transformation leaves the unit cell volume unchanged, changing, however, the fractional coordinates. The quantity we seek to minimize is the unit cell surface area

$$A_{\mathrm{surf}} = 2\left(|\mathbf{a} \times \mathbf{b}| + |\mathbf{b} \times \mathbf{c}| + |\mathbf{c} \times \mathbf{a}|\right) \tag{A.23}$$

which for a given volume is minimal for a cubic cell. Therefore, the algorithm will try to form angles of 90° between the vectors $\boldsymbol{a}$, $\boldsymbol{b}$, and $\boldsymbol{c}$. In case that

$$\tilde{\mathbf{a}} = \mathbf{a} \pm \mathbf{b} \tag{A.24}$$

is accepted, the lattice vectors and fractional coordinates are updated

$$\tilde{\mathbf{a}} = \mathbf{a} \pm \mathbf{b} \tag{A.25}$$

$$\tilde{\mathbf{b}} = \mathbf{b} \tag{A.26}$$

$$\tilde{\mathbf{c}} = \mathbf{c} \tag{A.27}$$
$$\tilde{x_{\mathrm{i,f}}} = x_{\mathrm{i,f}} \tag{A.28}$$
$$\tilde{y_{\mathrm{i,f}}} = y_{\mathrm{i,f}} \mp x_{\mathrm{i,f}} \tag{A.29}$$
$$\tilde{z_{\mathrm{i,f}}} = z_{\mathrm{i,f}} \tag{A.30}$$

leaving the particle coordinates

$$\begin{aligned} \mathbf{r}_{\mathrm{i}} &= \tilde{x_{\mathrm{i,f}}}\tilde{\mathbf{a}} + \tilde{y_{\mathrm{i,f}}}\tilde{\mathbf{b}} + \tilde{z_{\mathrm{i,f}}}\tilde{\mathbf{c}} \\ &= x_{\mathrm{i,f}}(\mathbf{a} \pm \mathbf{b}) + (y_{\mathrm{i,f}} \mp x_{\mathrm{i,f}})\mathbf{b} + z_{\mathrm{i,f}}\mathbf{c} \\ &= x_{\mathrm{i,f}}\mathbf{a} + y_{\mathrm{i,f}}\mathbf{b} + z_{\mathrm{i,f}}\mathbf{c} \end{aligned} \tag{A.31}$$

unchanged. In case that any of the fractional coordinates now lie outside the allowed region, i.e. the interval $[0, 1)$, 1 has to be added or subtracted to those quantities until they fulfill this requirement. For quasi-2D geometries, we cannot try, for obvious reasons, the combinations $\mathbf{a} \pm \mathbf{c}$ and $\mathbf{b} \pm \mathbf{c}$, as this would lead to problems with the z-periodicity in our parametrization. The lattice simplification is done in the full parametrization to allow maximum flexibility. Then, the lattice has to be transformed back to its reduced form (see appendix A.1.)

A.5. Derivation of the Interpolation for Tabulated Functions

We use a quadratic interpolation for special functions $f(x)$ after having tabulated their values at positions x_{n}

$$x_{\mathrm{n}} = x_{\min} + \frac{n}{N}(x_{\max} - x_{\min}) \tag{A.32}$$
$$f_{\mathrm{n}} = f(x_{\mathrm{n}}) \tag{A.33}$$
$$n = 0, 1, 2, ..., N, N+1, N+2 \tag{A.34}$$

we can expand $f(x)$ in a Taylor series, truncating after the second term

$$x_{\mathrm{n}} \leq x = x_{\mathrm{n}} + \xi h \leq x_{\mathrm{n+1}} \tag{A.35}$$
$$f(x) = f(x_{\mathrm{n+1}}) + (x - x_{\mathrm{n+1}})f'(x_{\mathrm{n+1}}) + \frac{1}{2}(x - x_{\mathrm{n+1}})^2 f''(x_{\mathrm{n+1}}) + ... \tag{A.36}$$

$$
\begin{aligned}
&\approx f_{n+1} + \frac{1}{2}(\frac{x - x_n}{h} - 1)(f_{n+2} - f_n) + \frac{1}{2}(\frac{x - x_n}{h} - 1)^2(f_{n+2} - 2f_{n+1} + f_n) \\
&= f_{n+1} + \frac{1}{2}(\xi - 1)(f_{n+2} - f_n) + \frac{1}{2}[\xi(\xi - 1) - (\xi - 1)](f_{n+2} - 2f_{n+1} + f_n) \\
&= f_n + \xi(f_{n+1} - f_n) + \frac{1}{2}\xi(\xi - 1)(f_{n+2} - 2f_{n+1} + f_n).
\end{aligned}
$$

Using a quadratic interpolation ensures that the *numerical* derivative is a continuous function, which is advantageous for the local optimization algorithm (see section 4.1), even though the analytical derivative will not *exactly* match the numerical one.

A.6. Cutoff Cell Determination

In an effort to minimize the computations necessary for a certain accuracy, we try to find out which cells have to be considered when carrying out the summation to the cutoff R (which can be either R_{cut}, K_{cut}, or R_{c}), as we truncate all interactions above R. In case of a real space cutoff, we have to increase the value of R to $\tilde{R}$

$$
\begin{aligned}
\tilde{R} &= R + r_{\mathrm{ij,max}} \\
&= R + \mathrm{MAX}_{\mathrm{ij}}\left(|\mathbf{r}_{\mathrm{ij}}|\right)
\end{aligned}
\tag{A.37}
$$

to ensure that all particle distances smaller than R are included. The calculation of $n_{\mathrm{c,max}}$, $n_{\mathrm{b,min}}\left(n_{\mathrm{c}}\right)$ and $n_{\mathrm{b,max}}\left(n_{\mathrm{c}}\right)$, and $n_{\mathrm{a,min}}\left(n_{\mathrm{c}}, n_{\mathrm{b}}\right)$ and $n_{\mathrm{a,max}}\left(n_{\mathrm{c}}, n_{\mathrm{b}}\right)$ (compare equ. 4.2) will be shown below. Calculations in reciprocal space are similar, but the roles of the vectors and their components is different. The values $n_{\mathrm{i,min}}$, $n_{\mathrm{i,max}}$ should, for all $n_{\mathrm{i,min}} \leq n_{\mathrm{i}} \leq n_{\mathrm{i,max}}$ and $i = a, b, c$, satisfy the relation

$$
\begin{aligned}
R^2 &\leq |\mathbf{r}|^2 = x^2 + y^2 + z^2 \\
&= \left(n_{\mathrm{a}}a_{\mathrm{x}} + n_{\mathrm{b}}b_{\mathrm{x}} + n_{\mathrm{c}}c_{\mathrm{x}}\right)^2 + \left(n_{\mathrm{b}}b_{\mathrm{y}} + n_{\mathrm{c}}c_{\mathrm{y}}\right)^2 + \left(n_{\mathrm{c}}c_{\mathrm{z}}\right)^2 .
\end{aligned}
\tag{A.38}
$$

This inequality is always fulfilled for (i.e. even in the worst case where $x = y = 0$)

$$
\left(n_{\mathrm{c}}c_{\mathrm{z}}\right)^2 \geq R^2 \tag{A.39}
$$

$$
n_{\mathrm{c}} : \begin{cases} n_{\mathrm{c,min}} \leq -\frac{R}{c_{\mathrm{z}}} \\ n_{\mathrm{c,max}} \geq \frac{R}{c_{\mathrm{z}}} \end{cases} . \tag{A.40}
$$

The actual values need to be rounded to the next integer. For any given n_c, equ. A.39 can be rearranged to (again assuming the worst case $x = 0$)

$$\begin{aligned} (n_\mathrm{b} b_\mathrm{y} + n_\mathrm{c} c_\mathrm{y})^2 &\geq R^2 - (n_\mathrm{c} c_\mathrm{z})^2 && \text{(A.41)} \\ n_\mathrm{b} &: \begin{cases} n_{\mathrm{b,min}}\,(n_\mathrm{c}) \leq \frac{-\sqrt{R^2-(n_\mathrm{c}c_\mathrm{z})^2}-n_\mathrm{c}c_\mathrm{y}}{b_\mathrm{y}} \\ n_{\mathrm{b,max}}\,(n_\mathrm{c}) \geq \frac{\sqrt{R^2-(n_\mathrm{c}c_\mathrm{z})^2}-n_\mathrm{c}c_\mathrm{y}}{b_\mathrm{y}} \end{cases} . && \text{(A.42)} \end{aligned}$$

This is only valid for $c_\mathrm{y} > 0$, so in the general case we have to compare the two results (rounded to the next integer) and choose the larger one for $n_{\mathrm{max,b}}$ and the smaller one for $n_{\mathrm{min,b}}$. Finally, we handle n_a in the same way

$$\begin{aligned} (n_\mathrm{a} a_\mathrm{x} + n_\mathrm{b} b_\mathrm{x} + n_\mathrm{c} c_\mathrm{x})^2 &\geq R^2 - (n_\mathrm{b} b_\mathrm{y} + n_\mathrm{c} c_\mathrm{y})^2 - (n_\mathrm{c} c_\mathrm{z})^2 && \text{(A.43)} \\ n_\mathrm{a} &: \begin{cases} n_{\mathrm{a,min}}\,(n_\mathrm{c}, n_\mathrm{b}) \leq \frac{-\sqrt{R^2-(n_\mathrm{c}c_\mathrm{z})^2-(n_\mathrm{c}c_\mathrm{y}+n_\mathrm{b}b_\mathrm{y})^2}-(n_\mathrm{c}c_\mathrm{x}+n_\mathrm{b}b_\mathrm{x})}{a_\mathrm{x}} \\ n_{\mathrm{a,max}}\,(n_\mathrm{c}, n_\mathrm{b}) \geq \frac{\sqrt{R^2-(n_\mathrm{c}c_\mathrm{z})^2-(n_\mathrm{c}c_\mathrm{y}+n_\mathrm{b}b_\mathrm{y})^2}-(n_\mathrm{c}c_\mathrm{x}+n_\mathrm{b}b_\mathrm{x})}{a_\mathrm{x}} \end{cases} && \text{(A.44)} \end{aligned}$$

again rounded to the next integer and, depending on c_x and b_x, appropriately allocated.

A.7. 3D Order Parameters

In order to measure 3D orientational symmetry, Steinhardt [84] defined order parameters W_l

$$\begin{aligned} Q_\mathrm{lm}\,(\mathbf{r}) &= Y_\mathrm{lm}\,(\theta(\mathbf{r}), \phi(\mathbf{r})) && \text{(A.45)} \\ \bar{Q}_\mathrm{lm} &= \langle Q_\mathrm{lm}\,(\mathbf{r}) \rangle && \text{(A.46)} \\ W_\mathrm{l} &= \sum_{\substack{m_1, m_2, m_3 \\ m_1 + m_2 + m_3 = 0}} \begin{pmatrix} l & l & l \\ m_1 & m_2 & m_3 \end{pmatrix} \bar{Q}_{\mathrm{lm}_1} \bar{Q}_{\mathrm{lm}_2} \bar{Q}_{\mathrm{lm}_3} && \text{(A.47)} \end{aligned}$$

where $\bar{Q}_\mathrm{lm}$ is the average over the nearest neighbors, $\theta\,(\mathbf{r})$ and $\psi\,(\mathbf{r})$ are the polar angles of the bonds measured respective to some reference axis, and $Y_\mathrm{lm}\,(\theta, \psi)$ are the spherical harmonics.

A.8. Quasi-2D Order Parameters

In order to account for 3D deformations in layered systems, we defined order parameters similar to 2D order parameters. After determining in 3D the nearest neighbors j of particle i, we calculate the quantity

$$\Psi_{\mathrm{n}}(i) = \frac{1}{\tilde{N}_{\mathrm{NN}}(i)} \sum_{\mathrm{j}=1}^{\mathrm{N_{NN}(i)}} \exp(in\theta_{\mathrm{ij}}) \exp\left(-\frac{(z_{\mathrm{i}}-z_{\mathrm{j}})^2}{s^2}\right) \tag{A.48}$$

$$\tilde{N}_{\mathrm{NN}}(i) = \sum_{\mathrm{j}=1}^{\mathrm{N_{NN}(i)}} \exp\left(-\frac{(z_{\mathrm{i}}-z_{\mathrm{j}})^2}{s^2}\right) \tag{A.49}$$

where $N_{\mathrm{NN}}(i)$ is the number of nearest neighbors of particle i, $\tilde{N}_{\mathrm{NN}}(i)$ is the weighted number of neighbors, $s = \sigma$ is a softening factor for the z-contribution and θ_{ij} is the two-dimensional angle between a reference direction and the vector $\mathbf{r}_{\mathrm{ij}}$. The total order parameter of the configuration is then given by

$$\Psi_{\mathrm{n}} = \frac{1}{N} \sum_{\mathrm{i}=1}^{\mathrm{N}} |\Psi_{\mathrm{n}}(i)| . \tag{A.50}$$

While Ψ_4 and Ψ_6 can ideally characterize square and hexagonal order in monolayer systems, it is better to use Ψ_8 and Ψ_{12} for two reasons: first, Ψ_8 and Ψ_{12} are less susceptible to small deformations of the lattice; the second reason is related to the contributions from neighboring layers in slab geometries: as seen in section 5, neighboring layers are never directly on top of each other but rather "body centered". The neighborhood of a particle has thus not four- or six-fold, but eight- or twelve-fold rotational symmetry in 2D.

A.9. Voronoi Construction

In order to correctly determine the set of nearest neighbors for a particle, we chose the method of Voronoi construction [98]. This method divides space into polyhedra each then containing one particle. The faces of the Voronoi polyhedra are determined such that every point inside the polyhedra is closer to the particle *inside* the polyhedron than to any other particle. When polyhedra share a face,

the particles they contain are thus respective nearest neighbors. Figure A.1 shows a schematic representation of a Voronoi construction in 2D. In order to construct

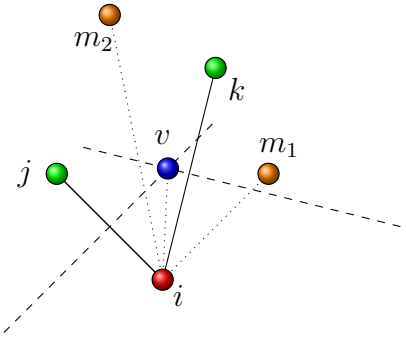

Figure A.1.: Schematic representation of Voronoi construction in 2D. The construction of the Voronoi polyhedron for particle i (red) is realized by considering pairs of neighbor candidates (j, k) (green). The planes halfway between those candidates and particle i determine possible faces (dashed lines). The intersection of these faces is a possible vertex v (blue). A vertex is invalidated if any other particle m (orange) generates a plane that invalidates the vertex. In the case shown above, particle m_1 invalidates the vertex while particle m_2 does not. Actual calculations are carried out in 3D.

the Voronoi polyhedron for particle i in 3D, we need to consider triplets of neighbor candidates (j, k, l). The planes located halfway between particles i and j (or k or l) are possible faces of the polyhedron. The intersection of the planes generated by (j, k, l) is a possible vertex of the polyhedron. The vertex fulfills a system of equations

$$(\mathbf{x}_\mathrm{i} - \mathbf{x}_\mathrm{j})^\mathrm{T}(\mathbf{v} - \frac{1}{2}(\mathbf{x}_\mathrm{i} + \mathbf{x}_\mathrm{j})) = 0 \tag{A.51}$$

$$(\mathbf{x}_\mathrm{i} - \mathbf{x}_\mathrm{k})^\mathrm{T}(\mathbf{v} - \frac{1}{2}(\mathbf{x}_\mathrm{i} + \mathbf{x}_\mathrm{k})) = 0 \tag{A.52}$$

$$(\mathbf{x}_\mathrm{i} - \mathbf{x}_\mathrm{l})^\mathrm{T}(\mathbf{v} - \frac{1}{2}(\mathbf{x}_\mathrm{i} + \mathbf{x}_\mathrm{l})) = 0 \tag{A.53}$$

or simplified

$$(\mathbf{x}_\mathrm{i} - \mathbf{x}_\mathrm{j})^\mathrm{T}\mathbf{v} = \frac{1}{2}(\mathbf{x}_\mathrm{i}^2 - \mathbf{x}_\mathrm{j}^2) \tag{A.54}$$

$$(\mathbf{x}_\mathrm{i} - \mathbf{x}_\mathrm{k})^\mathrm{T}\mathbf{v} = \frac{1}{2}(\mathbf{x}_\mathrm{i}^2 - \mathbf{x}_\mathrm{k}^2) \tag{A.55}$$

$$(\mathbf{x}_\mathrm{i} - \mathbf{x}_\mathrm{l})^\mathrm{T}\mathbf{v} = \frac{1}{2}(\mathbf{x}_\mathrm{i}^2 - \mathbf{x}_\mathrm{l}^2) \tag{A.56}$$

$$\begin{pmatrix} (\mathbf{x}_\mathrm{i} - \mathbf{x}_\mathrm{j})^\mathrm{T} \\ (\mathbf{x}_\mathrm{i} - \mathbf{x}_\mathrm{k})^\mathrm{T} \\ (\mathbf{x}_\mathrm{i} - \mathbf{x}_\mathrm{l})^\mathrm{T} \end{pmatrix} \cdot \mathbf{v} = \begin{pmatrix} \frac{1}{2}(\mathbf{x}_\mathrm{i}^2 - \mathbf{x}_\mathrm{j}^2) \\ \frac{1}{2}(\mathbf{x}_\mathrm{i}^2 - \mathbf{x}_\mathrm{k}^2) \\ \frac{1}{2}(\mathbf{x}_\mathrm{i}^2 - \mathbf{x}_\mathrm{l}^2) \end{pmatrix} \tag{A.57}$$

$$\mathbf{v} = \begin{pmatrix} (\mathbf{x}_\mathrm{i} - \mathbf{x}_\mathrm{j})^\mathrm{T} \\ (\mathbf{x}_\mathrm{i} - \mathbf{x}_\mathrm{k})^\mathrm{T} \\ (\mathbf{x}_\mathrm{i} - \mathbf{x}_\mathrm{l})^\mathrm{T} \end{pmatrix}^{-1} \cdot \begin{pmatrix} \frac{1}{2}(\mathbf{x}_\mathrm{i}^2 - \mathbf{x}_\mathrm{j}^2) \\ \frac{1}{2}(\mathbf{x}_\mathrm{i}^2 - \mathbf{x}_\mathrm{k}^2) \\ \frac{1}{2}(\mathbf{x}_\mathrm{i}^2 - \mathbf{x}_\mathrm{l}^2) \end{pmatrix}. \tag{A.58}$$

The inverse of a 3×3 matrix can easily be calculated using Cramer's rule. To check the validity of the vertex, we have to verify that no other particle m generates a plane that invalidates the vertex. This test can be done by calculating the projection

$$P = \frac{(\mathbf{x}_\mathrm{m} - \mathbf{x}_\mathrm{i})^\mathrm{T}(\mathbf{v} - \mathbf{x}_\mathrm{i})}{|(\mathbf{x}_\mathrm{m} - \mathbf{x}_\mathrm{i})|} \tag{A.59}$$

and comparing it to $|(\mathbf{x}_\mathrm{m} - \mathbf{x}_\mathrm{i})|/2$. A vertex is thus valid if

$$\frac{(\mathbf{x}_\mathrm{m} - \mathbf{x}_\mathrm{i})^\mathrm{T}(\mathbf{v} - \mathbf{x}_\mathrm{i})}{|(\mathbf{x}_\mathrm{m} - \mathbf{x}_\mathrm{i})|^2} \leq \frac{1}{2} + \delta \tag{A.60}$$

where δ is a small tolerance (see below). In order to generate a list of neighbor candidates, we consider all particles in the (central) unit cell and several surrounding unit cells (more than a single layer are necessary for distorted unit cells, so lattice simplification (see section 4.2) is advisable). For slab geometries, only neighboring unit cells within the slab are taken into consideration. To account for the walls, we also add mirror images of particle i at positions

$$\begin{pmatrix} x_\mathrm{i} \\ y_\mathrm{i} \\ -z_\mathrm{i} - \sigma \end{pmatrix}, \begin{pmatrix} x_\mathrm{i} \\ y_\mathrm{i} \\ -z_\mathrm{i} + 2h + \sigma \end{pmatrix} \tag{A.61}$$

to the list of possible neighbors. These mirror images project planes that are located exactly at the walls, but have themselves no physical meaning (so we have to neglect them for order parameter calculations). The lattices we deal with can be degenerate when it comes to nearest neighbors (i.e. diagonal neighbors in square or

rectangular lattices). While this should not be a problem from the technical point of view (e.g. a rectangular lattice will always be a bit distorted and each particle will thus have six neighbors and not four or eight), it can lead to small fluctuations having a large effect. We therefore decided to implement a small tolerance $\delta = 10^{-5}$ for degenerate vertices (i.e. we rather use more neighbors than fewer). An artifact of this is the sudden jumps in the twelve-fold order parameter Ψ_{12} in square phases (see section 5). The much larger eight-fold order parameter Ψ_8 remains the same at such points and the phases before and after are the same (i.e. the continuous deformation is just slightly stronger). However, we have to note that, while all phase transitions are visible as sudden changes in the order parameters, not all sudden changes in order parameters coincide with phase transitions. This could clearly be improved upon by a better definition of the order parameters.

B. Example Files

B.1. Example Input File

The following input file shows example input parameters (in this case we will perform isochoric optimizations on a system for $\mu^* = 1$ and $\rho_\mathrm{H} = 0.5$ (corresponding to $V_\mathrm{UC} = 2N\sigma^3$ before rescaling) in a slab geometry ($h = 0.3\sigma$) and $\alpha = 12$).

INDIVIDUALS number of individuals N_ind

GENERATIONS number of individuals N_gen created (used as classical generation number in serial version of the program)

MUTATIONRATE probability for mutation using strain matrix p_str

MUTATIONRATE2 probability for mutation using random dipole rotation p_rot

MUTATIONRATE3 probability for mutation using particle kind permutation p_perm

MUTATIONRATE4 probability for mutation using lattice squashing p_squ

ROTATE_SIGMA strength σ_rot of the dipole rotation mutation

FITNESSPARAMETER parameter P_fit used in the fitness function

ELITISM best N_elit individuals are kept (new individuals can't replace these)

MOMENT_FREE switch for all dipoles in z-direction (0) or free dipole orientation (1)

V_UC_FIXED switch for isobaric (NPT) mode (0) or isochoric (NVT) mode (1)

INITIAL_V_UC initial unit cell volume in multiples of $N\sigma^3$

WRITE_ANALYTICS create additional output

POTENTIAL_FORM switch for Lennard-Jones, i.e. $2\alpha - \alpha$, potential (1) or inverse power law potential (2)

POTENTIAL_ALPHA potential parameter α

POTENTIAL_WALL wall potential parameter α_{wall} for quasi-2D geometry (0 for no such potential)

SIGMA particle size σ

EPSILON potential parameter ϵ

PARTICLES_1 number N_1 of particles of kind 1

PARTICLES_2 number N_2 of particles of kind 2

MOMENTUM_1 dipole moment μ_1^* of particles of kind 1

MOMENTUM_2 dipole moment μ_2^* of particles of kind 2

PRESSURE pressure P in isobaric (NPT) mode

FIELD electric field $E^*_{\mathrm{ext,z}}$in z-direction (only useful in quasi-2D geometry)

SLAB slab thickness h in quasi-2D geometry

STRETCH vacuum layer thickness h_{vac} for quasi-2D approximation

OVERLAP minimum distance between particle centers for valid configurations

ACCURACY L-BFGS-B accuracy (multiplied by machine precision, i.e. by $\approx 10^{-16}$)

RELAXATION_STEPS abort relaxation after a certain number of steps to prevent excessive relaxation times for bad configurations

IPL_R_CUT Real space cutoff radius R_{c} or R_{cut} for inverse power law interaction.

IPL_K_CUT Reciprocal space cutoff radius K_{cut} for inverse power law interaction.

IPL_NU Ewald summation parameter for inverse power law interaction.

DIP_R_CUT Real space cutoff radius R_{cut} for dipolar interaction.

DIP_K_CUT Reciprocal space cutoff radius K_{cut} for dipolar interaction.

DIP_NU Ewald summation parameter for dipolar interaction.

GRID_IPL_REAL Number of points for tabulation of lattice sum real space summation for inverse power law interaction.

GRID_IPL_R Number of points for tabulation of Ewald sum real space summation for inverse power law interaction.

GRID_IPL_K Number of points for tabulation of Ewald sum reciprocal space summation for inverse power law interaction.

GRID_DIP_R Number of points for tabulation of Ewald sum real space summation for dipolar interaction.

GRID_DIP_K Number of points for tabulation of Ewald sum reciprocal space summation for dipolar interaction.

R0 Lower cutoff $r_{\min}$ for tabulation in real space in units of σ.

K0 Lower cutoff $k_{\min}$ for tabulation in reciprocal space in units of $1/\sigma$.

```
INDIVIDUALS 5
ELITISM 2
GENERATIONS 50
REBOOT 200
MUTATIONRATE 0.05
MUTATIONRATE2 0.02
MUTATIONRATE3 0.02
MUTATIONRATE4 0.05
ROTATE_SIGMA 0.5
FITNESSPARAMETER 3
MOMENT_FREE 1
V_UC_FIXED 1
INITIAL_V_UC 2.0
WRITE_ANALYTICS 0
POTENTIAL_FORM 2
POTENTIAL_ALPHA 12.0
POTENTIAL_WALL 0.0
SIGMA 1.0
EPSILON 1.0
PARTICLES_1 4
PARTICLES_2 0
MOMENTUM_1 1.0
MOMENTUM_2 0.0
PRESSURE 0.0
FIELD 0.0
SLAB 0.3
STRETCH 15.0
OVERLAP 0.01
ACCURACY 1.0d1
RELAXATION_STEPS 2000
IPL_R_CUT 10.0
IPL_K_CUT 0.0
IPL_NU 0.0
DIP_R_CUT 7.0
DIP_K_CUT 12.0
DIP_NU 1.5
GRID_IPL_REAL 4e4
GRID_IPL_R 0
GRID_IPL_K 0
GRID_DIP_R 4e4
GRID_DIP_K 4e4
R0 0.5
K0 0.2
```

B.2. Example Output File

The following output file shows the results of the run for the input file above.

```
particles (1,2), momentum (1,2), pressure, slab, stretch
  4   0  1.00  0.00     0.00  0.300   51.00
 lattice vectors
   2.5057502174580844        0.0000000000000000        0.0000000000000000
  2.39893835411015412E-006   2.4558897016035455        0.0000000000000000
  -1.0719552546178548      -0.95638882570696582        15.300000000000001
 kind, particle coordinates (fractional)
  1 0.000015297347 0.761966840534 0.000000000000
  1 0.000015483179 0.261966861441 0.000000000000
  1 0.508403977713 0.519603170967 0.019607843137
  1 0.508403662655 0.019603167213 0.019607843137
 kind, particle coordinates
  1   0.0000   0.0000   0.0000
  1  -0.0000  -1.2279   0.0000
  1   1.2529  -0.6140   0.3000
  1   1.2529  -1.8419   0.3000
 kind, dipole orientations (fractional)
  1  1.57079566524  1.57079787641
  1  1.57079563794  1.57079642418
  1  1.57079580835  1.57079618060
  1  1.57079576807  1.57079774934
 kind, dipole orientations
  1   0.0000   1.0000  -0.0000
  1   0.0000   1.0000  -0.0000
  1   0.0000   1.0000   0.0000
  1   0.0000   1.0000  -0.0000
 gfe, e (per base particle)
 -0.90111371663839279      -0.90111371663839279
 uc volume (per base particle), alignment, NN
  0.46153846153846151       0.99999999999970757        6.0000000000000000
 order parameters: psi4, psi6, psi8, psi12
  0.27232342483954547       0.95226432518659376
  9.27130365756480418E-002  0.81688080979930144
```

It always seems impossible,
until it is done.
Nelson Mandela